A new tool for miscibility control: Linear coupling

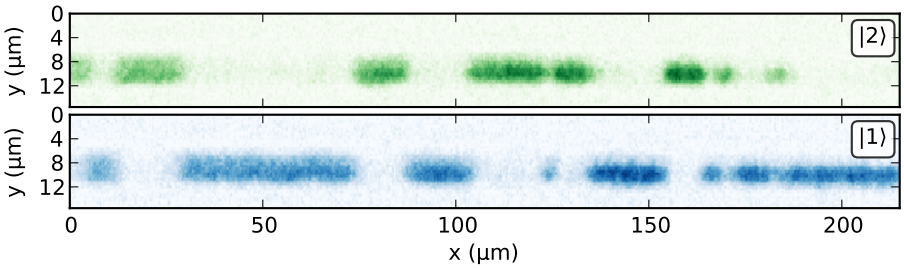

Eike Nicklas

2013

Dissertation
submitted to the
Combined Faculties of the Natural Sciences and Mathematics
of the Ruperto-Carola-University of Heidelberg. Germany
for the degree of
Doctor of Natural Sciences

Put forward by
Eike Nicklas
born in: Heidelberg, Germany
Oral examination: 23. July, 2013

A new tool for miscibility control: Linear coupling

Referees: Prof. Dr. Markus K. Oberthaler
Prof. Dr. Thomas Gasenzer

Abstract

In this work we experimentally study the rich interplay of a linear coupling and non-linear interactions between the two components of an elongated Bose-Einstein condensate of ^{87}Rb. In the limit of strong linear coupling we generate dressed states and explore the effective interactions between them. We find that the miscibility of dressed states is opposite to that of the atomic states. If the characteristic energies of interactions and linear coupling are equal they give rise to a miscible-immiscible quantum phase transition. We study the linear response of the system to sudden quenches in the vicinity of the critical point by analyzing spin correlations in the system. A power law scaling of the characteristic length scales is observed on both sides of the phase transition and the scaling exponents agree with the mean field prediction. Temporal scaling is found on the miscible side in agreement with a prediction based on Bogoliubov theory. In addition, experimental results for finite-time quenches through the critical point are presented. The good control over amplitude and phase of the linear coupling field offers new possibilities for the study of both equilibrium and dynamical properties of phase transitions.

Zusammenfassung

Diese Arbeit behandelt das vielfältige Zusammenspiel von linearer Kopplung und nichtlinearen Wechselwirkungen zwischen zwei Komponenten eines elongierten Bose-Einstein Kondensats von ^{87}Rb. Im Grenzfall starker linearer Kopplung erzeugen wir sogenannte 'dressed states' und untersuchen die Wechselwirkungen zwischen ihnen. Dabei zeigen wir, dass die Mischbarkeit von 'dressed states' entgegengesetzt der von atomaren Zuständen ist. Im Falle gleich großer charakteristischer Energien von Wechselwirkung und Kopplung findet ein Quantenphasenübergang von mischbar zu nicht mischbar statt. Wir untersuchen die Antwort des Systems auf plötzliche Parameteränderungen in der Nähe des kritischen Punktes anhand des Verhaltens von Spinkorrelationen. Dabei zeigt sich ein Potenzgesetz im Skalieren der charakteristischen Längenskalen auf beiden Seiten des Phasenübergangs, wobei die Exponenten mit der Vorhersage der Molekularfeldnäherung übereinstimmen. Auf der mischbaren Seite wird ein zeitliches Skalierungsverhalten in Übereinstimmung mit der Vorhersage der Bogoliubov-Theorie beobachtet. Zusätzlich präsentieren wir experimentelle Ergebnisse zu langsamen Rampen in der Nähe des kritischen Punktes. Die gute Kontrolle über die Amplitude und Phase des linearen Kopplungsfeldes schafft neue Möglichkeiten, die Eigenschaften von Phasenübergängen sowohl im dynamischen Fall als auch unter Gleichgewichtsbedigungen zu untersuchen.

Contents

1. Introduction

Phase transitions are ubiquitous in nature. One everyday example is the boiling of water, which marks the transition from a liquid to a gaseous state at a temperature of 100°C under standard pressure conditions of 1 bar. Further examples of phase transitions range from Bose-Einstein condensation to the high temperature plasma in the early stages of the universe after the Big Bang. These examples demonstrate that phase transitions occur on all energy scales from the nanokelvin regime up to beyond 10^{20} Kelvin.

The boiling of water is a paradigm example of a first order phase transition as the two phases, water and steam, can coexist at the transition temperature due to latent heat in the process. As heat is added to boiling water its temperature stays constant, but the fraction of particles in gaseous form is increased. In second order phase transitions the two phases cannot coexist at the transition point. A well known example is the Curie point separating ferromagnetic from paramagnetic behavior in magnetic materials. Above the Curie temperature and in the absence of external magnetic fields the magnetic moments of the atoms in the material point in random directions. When cooling below the transition point the magnetic moments align along a randomly chosen axis of magnetization. This is an illustrative example of a symmetry breaking in phase transitions, as the system spontaneously chooses one out of a set of equivalent configurations.

A phase transition is caused by the competition of two energy scales, one of them favoring an ordered state and the other a disordered configuration. These energy scales are equal at the transition point. In thermodynamic or classical phase transitions one of these competing quantities is given by temperature or pressure and the loss of order is driven by entropy due to thermal fluctuations. In contrast, quantum phase transitions occur at zero temperature and the symmetry breaking is caused by quantum fluctuations [1].

The study of critical phenomena at second order phase transitions has triggered many new concepts in theoretical physics such as the notion of universality or renormalization group methods. For example, the characteristic length and time scales of the system diverge at the critical point with a power law scaling. The corresponding critical exponents depend only on the universality class of the system given for example by its dimension or the range of interactions, but not on the microscopic details. Mean field theories can predict values for the critical exponents, but their validity breaks down close to the critical point.

Ultracold quantum gases offer new prospects for experimental studies of phase transitions and criticality as they are well isolated from the environment and offer a high level of control over the relevant system parameters such as interactions or the dimensionality of the trapping potential. They have been employed to study thermodynamic phase transitions such as Bose-Einstein condensation [2] or the Berezinskii-Kosterlitz-Thouless (BKT) transition in two dimensions [3] as well as quantum phase transitions. Prominent examples of the latter are the Mott insulator to superfluid transition [4, 5] or the Dicke phase transition [6]. Symmetry breaking has been observed in one-[7] and multi-component Bose-Einstein condensates [8, 9] as well as in the context of the aforementioned quantum phase transitions [10, 11]. Universality and scale invariance have been measured in the density fluctuations near the BKT transition [12] and quantum critical behavior was observed at the vacuum-to-superfluid transition in two-dimensional optical lattices [13].

Some of the experiments mentioned above employ sudden or finite-time quenches through or

towards the critical point. The relaxation dynamics following quenches is an interesting subject on its own and has been studied in the context of the light-cone-like spreading of correlations [14] and prethermalization [15]. In the context of phase transitions quenches have been proposed as a tool to probe both equilibrium and dynamical scaling properties near critical points [16].

In this thesis we report on the experimental realization of a quantum phase transition in a quasi one-dimensional two-component Bose-Einstein condensate as proposed in [17, 18]. The inter-atomic interactions are chosen such that the two components are immiscible, i.e. in the ground state their overlap is minimized. Thus, the ground state of the system consists of two separate domains each containing atoms of one component. In a homogeneous one-dimensional geometry this state breaks translational symmetry as the position of the boundary between the domains is chosen randomly [19]. The symmetry restoring component is realized by a linear coupling of the involved states employing an electromagnetic field, which favors spatial overlap of the two atomic clouds. A critical point occurs when the energy scales of the symmetry-breaking interactions and the symmetry-restoring linear coupling are equal.

In our experiments we characterize both ingredients for the phase transition, namely atomic interactions and the linear coupling. In the absence of a linear coupling the dynamics of the system is determined by inter-atomic interactions. A Feshbach resonance [20] allows us to tune the relevant interaction strength and we systematically analyze its effect on the spatial dynamics of the system. If the linear coupling is much stronger than the interactions, the latter can be neglected and the system is dominated by the coupling field. In analogy to optical dressed states [21] the system can be described by eigenstates of the linear coupling Hamiltonian. We experimentally generate dressed condensates using a novel non-adiabatic preparation scheme. In addition the effective interactions among dressed states are examined and contrasted to the interactions of the involved bare states.

After having independently studied the relevant ingredients for the miscible-immiscible transition we characterize the phase transition and measure the linear response of the system after sudden quenches to the vicinity of the transition point. A power law divergence of the characteristic length scales at the critical point is observed both on the miscible and on the immiscible side. In addition the extracted relaxation time in the miscible regime is compared to the energy gap of the excitation spectrum of the system. Our findings agree with theoretical mean field predictions based on Bogoliubov theory.

This thesis is organized as follows: After this introduction, we discuss the theoretical description of linearly coupled binary Bose-Einstein condensates and summarize the results necessary for the interpretation of the experimental observations. The third chapter introduces our experimental system and presents the employed methods for analyzing the obtained data. Chapter 4 deals with the interaction properties of dressed states, which are obtained from the amplitude of Rabi oscillations after several hundred oscillation cycles. These results are published in [22]. The implementation of the miscible-immiscible quantum phase transition is presented in chapter 5 and the non-equilibrium dynamics of the system following a sudden quench is discussed. The final chapter discusses dynamical scaling near phase transitions in the context of the Kibble-Zurek mechanism. A compact overview of the relevant experimental parameters and numerical methods for the simulation of Bose-Einstein condensates is provided in the appendices.

The following experiments are not discussed in this thesis, but were performed during the same time.

- *Nonlinear atom interferometry beats classical precision limit* [23]
- *Classical Bifurcation at the Transition from Rabi to Josephson Dynamics* [24]
- *Atomic homodyne detection of continuous variable entangled twin-atom states* [25]
- *Optimized absorption imaging of mesoscopic atomic clouds* [26]

2. Theory of linearly coupled interacting Bose-Einstein condensates

Bose-Einstein condensates are versatile tools for the study of interacting macroscopic quantum systems. The theoretical description of such degenerate quantum gases is significantly simplified by their good isolation from the environment and their low temperature. As the ground state of the system is macroscopically occupied it can be described as a classical field in the so-called mean field approximation [27]. In addition, due to the small kinetic energies of the atoms, interactions are possible only via s-wave scattering. Thus, atomic interactions are characterized by a single parameter, the s-wave scattering length a_s. A positive scattering length $a_s > 0$ denotes repulsive interactions, while $a_s < 0$ implies attraction between the atoms.

Compared to the situation with a single atomic species, the interaction properties of two-component condensates are much richer as each component interacts with atoms both of the same and of the other species. The relative values of the different scattering lengths determine fundamental properties of the system such as its miscibility or stability. These characteristics are fundamentally modified in the presence of a radiation field that linearly couples the two components. For example, an immiscible system can be tuned miscible by the radiation field [17].

In this chapter we introduce the theoretical description of linearly coupled interacting two-component Bose-Einstein condensates in the mean field approximation. We will discuss their ground state properties and excitation spectra along with the resulting dynamics. In our experimental system the atomic clouds are confined in an elongated trapping potential. Thus, we will constrain the discussion to one dimension. We will simplify the description by assuming a homogeneous system without longitudinal confinement as it allows to derive many results analytically. The deviations caused by a trapping potential will be discussed where necessary and quantified by numerical simulations.

2.1. Hamiltonian and equations of motion

We begin our discussion with the Hamiltonian of two interacting atomic clouds in the presence of a linear coupling field. In addition, this section introduces the relevant quantities and the mean field equations of motion.

Hamiltonian

Our experimental system consists of a Bose-Einstein condensate of ^{87}Rb. The two components are realized by different hyperfine states of the electronic ground state, which are coupled via microwave and radio frequency radiation. The Hamiltonian of the system consists of three terms [28, 18]

$$\hat{H} = \hat{H}_0 + \hat{H}_{\text{int}} + \hat{H}_{\text{cpl}} \tag{2.1}$$

$\hat{H}_0$ describes the single particle effects, $\hat{H}_{\text{int}}$ the interactions among atoms in the same as well as in different states, while $\hat{H}_{\text{cpl}}$ summarizes the effects of a possibly detuned linear coupling of the two

components. In second quantization these term are given by

$$\hat{H}_0 = \sum_{i=1,2} \int \mathrm{d}x\, \hat{\Psi}_i^\dagger \left(-\frac{\hbar^2}{2m}\nabla^2 + V \right) \hat{\Psi}_i$$
$$\hat{H}_{\mathrm{int}} = \frac{1}{2} \sum_{i,j=1,2} g_{ij} \int \mathrm{d}x\, \hat{\Psi}_i^\dagger \hat{\Psi}_j^\dagger \hat{\Psi}_j \hat{\Psi}_i$$
$$\hat{H}_{\mathrm{cpl}} = -\frac{1}{2} \int \mathrm{d}x\, \left[\hbar\tilde{\Omega} \hat{\Psi}_1^\dagger \hat{\Psi}_2 + \hbar\tilde{\Omega}^* \hat{\Psi}_2^\dagger \hat{\Psi}_1 \right] + \frac{1}{2}\hbar\delta \int \mathrm{d}x\, \left[\hat{\Psi}_2^\dagger \hat{\Psi}_2 - \hat{\Psi}_1^\dagger \hat{\Psi}_1 \right]$$

where $\hat{\Psi}_i = \hat{\Psi}_i(x,t)$ denote bosonic field annihilation operators obeying the bosonic commutation relations, $2\pi\hbar$ Planck's constant, m the atomic mass, $V = V(x)$ an external potential identically acting on the two components and $g_{ij} = \frac{4\pi\hbar^2 a_{ij}}{m}$ the interaction strength parametrized by the s-wave scattering length a_{ij}.[1] The linear coupling between the components is characterized by the Rabi frequency $\tilde{\Omega} = \Omega e^{i\varphi}$ and the detuning δ from the atomic resonance. $\hat{H}_0$ and $\hat{H}_{\mathrm{cpl}}$ are single particle Hamiltonians, whereas $\hat{H}_{\mathrm{int}}$ introduces nonlinear effects via two-body collisions.

Mean field description and classical Hamiltonian

At low temperatures and macroscopic atom numbers the field operators $\hat{\Psi}_i$ for the Bose-Einstein condensates can be replaced by classical complex-valued functions $\psi_i(x,t)$, which we call the order parameter or wave function of the condensate [27]. In this *mean field description*, the linear atom density is given by $n_i(x,t) = \psi_i^*(x,t)\psi_i(x,t)$ and the classical Hamiltonian takes the form

$$H = H_0 + H_{\mathrm{int}} + H_{\mathrm{cpl}} \tag{2.2}$$

with

$$H_0 = \sum_{i=1,2} \int \mathrm{d}x \left(-\frac{\hbar^2}{2m}\psi_i^* \nabla^2 \psi_i + V n_i \right)$$
$$H_{\mathrm{int}} = \frac{1}{2} \sum_{i,j=1,2} g_{ij} \int \mathrm{d}x\, n_i n_j$$
$$H_{\mathrm{cpl}} = -\frac{1}{2} \int \mathrm{d}x\, \left[\hbar\tilde{\Omega}\psi_1^*\psi_2 + \hbar\tilde{\Omega}^*\psi_2^*\psi_1 \right] + \frac{1}{2}\hbar\delta \int \mathrm{d}x\, [n_2 - n_1]$$

In the following we denote the number of atoms in the i-th component by $N_i = \int \mathrm{d}x\, n_i(x)$ and their normalized difference by the imbalance $z = \frac{N_2 - N_1}{N_1 + N_2}$.

Equations of motion

The equations of motion governing the dynamics of a two-component condensate can be obtained from the Hamiltonian given by Equation 2.1 using the Heisenberg equation $i\hbar\partial_t \hat{\Psi}_i = [\hat{\Psi}_i, \hat{H}]$, which yields the coupled pair of equations

[1] The interaction parameters g_{ij} are modified for (quasi-)one-dimensional systems. See subsection B.1.1 for details.

$$
\begin{aligned}
i\hbar\frac{\partial}{\partial t}\psi_1 &= \left[-\frac{\hbar^2}{2m}\nabla^2 + V + g_{11}|\psi_1|^2 + g_{12}|\psi_2|^2\right]\psi_1 - \frac{\hbar\tilde{\Omega}}{2}\psi_2 - \frac{\hbar\delta}{2}\psi_1 \\
i\hbar\frac{\partial}{\partial t}\psi_2 &= \left[-\frac{\hbar^2}{2m}\nabla^2 + V + g_{22}|\psi_2|^2 + g_{12}|\psi_1|^2\right]\psi_2 - \frac{\hbar\tilde{\Omega}^*}{2}\psi_1 + \frac{\hbar\delta}{2}\psi_2
\end{aligned}
\tag{2.3}
$$

These equations are the main tool for modeling the dynamics of the two-component condensate in the mean field regime. Their single-component version was derived independently by Gross [29] and Pitaevskii [30] and is referred to as the Gross-Pitaevskii equation.

2.2. Single spatial mode approximation

The dynamics of the system is governed by the interplay of several ingredients: A linear coupling of two states, non-linear interactions among the atoms, as well as the spatial degree of freedom. Before discussing the properties of this complex system we will first focus on each of these contributions separately in order to understand their physical characteristics.

As a first simplification we neglect the spatial degree of freedom and we reduce the one-dimensional system to zero dimensions such that only the internal degree of freedom remains, i.e. dynamics in the relative population of the two states. In this case, the spatial part of wave function $\phi_1(x) = \phi_2(x) = \phi(x)$ is the same for both components and we assume $\phi(x)$ to be normalized to 1. Experimentally the single spatial mode approximation is applicable when the atomic cloud is confined in a tight trap, such that the extent of the cloud is smaller than the typical length scale of density variations due to interactions. In the single mode approximation the system reduces to well-known models: In the absence of interactions it is described by the Rabi Hamiltonian whose eigenstates are the dressed states. The inclusion of interactions leads to the Josephson Hamiltonian. In this section, we will discuss these two systems.

Bloch sphere representation

In the absence of spatial degrees of freedom the system is fully described by N atoms, each having two internal states $|1\rangle$ and $|2\rangle$. Such a two-level system can be mapped onto a spin $J = 1/2$ system by assigning the atomic state $|1\rangle$ ($|2\rangle$) to the eigenstate of the spin operator $\hat{J}_z$ with the eigenvalue $j_z = -1/2$ ($+1/2$). A general pure quantum state of the two-level system is characterized by the normalized probability amplitude of being in either state and the relative quantum mechanical phase φ. Thus it can be represented in spherical coordinates as $|\theta, \varphi\rangle = \sin(\theta/2)|1\rangle + e^{-i\varphi}\cos(\theta/2)|2\rangle$.

This expression describes the point on the surface of a sphere with the polar angle θ and the azimuthal angle φ. In this *Bloch sphere representation* the axes were chosen such that the south pole corresponds to state $|1\rangle$ and the north pole to state $|2\rangle$. The population difference $(|2\rangle\langle 2| - |1\rangle\langle 1|)/2$ is mapped onto $\hat{J}_z$ and the coherences are represented by $\hat{J}_x = (|2\rangle\langle 1| + |1\rangle\langle 2|)/2$ and $\hat{J}_y = (|2\rangle\langle 1| - |1\rangle\langle 2|)/2i$ [31, 32].

2.2.1. Dressed states

In the limit of strong linear coupling, $\hbar\Omega \gg ng_{ij}$, interactions can be neglected and the dynamics of the system is governed by $\hat{H}_{\mathrm{cpl}}$. Identifying the two modes $|1\rangle = \psi_1$ and $|2\rangle = \psi_2$ the Hamiltonian

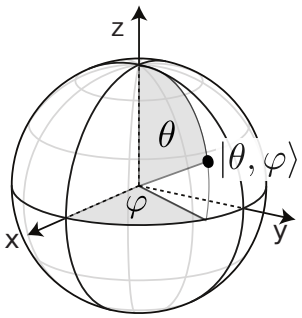

Figure 2.1.: Schematic representation of a quantum state $|\theta, \varphi\rangle$ of a two-level system on the Bloch sphere. The shaded regions illustrate the definition of θ and φ.

can be written in matrix notation as

$$\hat{H}_{\mathrm{cpl}} = -\frac{1}{2}\hbar \begin{pmatrix} \delta & \tilde{\Omega} \\ \tilde{\Omega}^* & -\delta \end{pmatrix} = -\frac{1}{2}\hbar \begin{pmatrix} \delta & \Omega e^{i\varphi} \\ \Omega e^{-i\varphi} & -\delta \end{pmatrix} \tag{2.4}$$

In analogy to quantum optics [21] the eigenstates of this Hamiltonian are the *dressed states*

$$\begin{aligned} |+\rangle &= e^{i\varphi/2}\sin(\theta/2)|1\rangle + e^{-i\varphi/2}\cos(\theta/2)|2\rangle \\ |-\rangle &= e^{i\varphi/2}\cos(\theta/2)|1\rangle - e^{-i\varphi/2}\sin(\theta/2)|2\rangle \end{aligned} \tag{2.5}$$

with the mixing angle $\tan\theta = -\Omega/\delta$. The corresponding eigenenergies are $E_\pm = \frac{\hbar}{2}(\mp\Omega_{\mathrm{eff}} - \delta)$, where $\Omega_{\mathrm{eff}} = \sqrt{\Omega^2 + \delta^2}$ denotes the oscillation (Rabi) frequency in the presence of a detuning [31]. In the limit of a large detuning $|\delta| \gg \Omega$, $\theta = 0$ and the dressed states coincide with the atomic states $|1\rangle$ and $|2\rangle$ [33]. On resonance, $\delta = 0$, the dressed states are equal superpositions of the atomic states $|+\rangle = \frac{1}{\sqrt{2}}(|1\rangle + |2\rangle)$ and $|-\rangle = \frac{1}{\sqrt{2}}(|1\rangle - |2\rangle)$ with eigenenergies $-\frac{1}{2}\hbar\Omega$ and $+\frac{1}{2}\hbar\Omega$, respectively. Note that the $|+\rangle$ state is lower in energy and corresponds to the ground state while $|-\rangle$ is an excited state.[2]

In terms of the spin representation introduced above the linear coupling Hamiltonian is written as $\hat{H}_{\mathrm{cpl}} = \hbar\Omega(\cos\varphi\hat{J}_x + \sin\varphi\hat{J}_y) + \hbar\delta\hat{J}_z$ [34]. Thus, in the Bloch sphere picture, the action of the Hamiltonian Equation 2.4 corresponds to a rotation around the axis (θ, φ). For resonant coupling $\theta = \pi/2$ and the rotation axis passes through the equator, whereas it is tilted towards one of the poles by a non-zero detuning. The $|+\rangle$ dressed state is parallel and the $|-\rangle$ state antiparallel to this rotation axis and thus they are stationary [31].

A generic pure quantum state $|\theta', \varphi'\rangle$ which is not aligned with the rotation axis oscillates with the frequency Ω_{eff} and a non-zero amplitude around (θ, φ). The amplitude of these *Rabi oscillations* depends on the relative phase $\Delta\varphi = \varphi' - \varphi$ of the atomic state and the linear coupling as well as $\Delta\theta = \theta' - \theta$. The angle θ' is determined by the imbalance of the initial state and θ by the detuning δ. In particular if the system is prepared in an atomic state, e.g. $|1\rangle$, and the linear coupling is resonant, then all atoms oscillate coherently between the two levels.

In the following, we will restrict the discussion to the case of resonant coupling, $\delta = 0$, where the dressed states $|+\rangle$ and $|-\rangle$ lie on the equator of the Bloch sphere and correspond to an equal probability of being in state $|1\rangle$ or $|2\rangle$. A possible experimental scheme for preparing a dressed state is to generate an equal superposition of the atom states and to adjust the relative phase $\Delta\varphi = 0$

[2] This definition is opposite to the commonly used convention due to the leading minus sign in Equation 2.4. This sign is included in order to conform with Equation 2.1.

in order to obtain $|+\rangle$ and $\Delta\varphi = \pi$ for $|-\rangle$. This scheme aligns the rotation axis to be (anti-) parallel with the atomic state. The experimental implementation of this method will be discussed in subsection 3.1.2 and section 5.1.

2.2.2. Internal Josephson junction

In the presence of interactions the oscillation dynamics on the Bloch sphere is modified by additional non-linear terms. The effect of interactions can be written in the spin representation as $\hat{H}_{\text{int}} = \hbar\chi\hat{J}_z^2$ with the effective nonlinearity $\hbar\chi = \frac{1}{2}(g_{11}+g_{22}-2g_{12})\int \mathrm{d}^3x\,|\phi(x)|^4$ [34]. This term corresponds to a rotation around the z-axis with an angular velocity that depends on the distance from the equator, i.e. the mean value of z. This effect is referred to as 'one-axis twisting' [35] and has been used to generate squeezed states which allow to improve interferometry beyond the statistical limit of independent measurements known as the standard quantum limit [23, 36].

The interesting quantum properties of a two-mode system with both on-site interaction and a linear coupling (equivalent to a tunneling link) between the sites were first discovered by Brian D. Josephson in 1962, when he considered two superconductors that are coupled via a weak insulating layer [37]. For example, he predicted an oscillating current when applying a constant external voltage, a phenomenon known as the ac Josephson effect. These characteristics have been observed in various experimental systems, in particular using interacting atomic states in a Bose-Einstein condensate coupled via Rabi coupling [24]. This realization is referred to as an *internal Josephson junction* [38]. For an in-depth derivation and discussion of the dynamics we refer to [39, 40]. In this section, we will only summarize the results that are relevant in the context of the quantum phase transition discussed in this thesis.

Plasma and π oscillations

We consider a resonantly coupled system leading to $\theta = \pi/2$ and without loss of generality assume the phase of the linear coupling to be $\varphi = 0$. In the absence of interactions a quantum state that is prepared close to the rotation axis, e.g. $|\theta = \pi/2, \varphi = \varepsilon\rangle$ with $\varepsilon \ll 1$, rotates on a circular path around $(\theta = \pi/2, \varphi = 0)$ with the frequency Ω. The presence of interactions $\hat{H}_{\text{int}}$ modifies both the shape of the trajectory in the classical phase space spanned by the relative population imbalance and phase of the two states and the oscillation frequency depending on the sign of χ and the relative strength of interactions and linear coupling $\Lambda = \frac{N|\chi|}{\Omega}$ [24].

In the Rabi regime of weak interactions ($\Lambda < 1$) and assuming $\chi > 0$, the velocity fields on the Bloch sphere due to linear coupling and interactions co-propagate resulting in an increased oscillation frequency $\omega_{\text{pl}} = \Omega\sqrt{1+\Lambda}$. These oscillations are often referred to as *plasma oscillations*. A relative phase of $\varphi = \pi$ leads to counter-propagating velocity fields resulting in slower *π oscillations* with a frequency $\omega_\pi = \Omega\sqrt{1-\Lambda}$. Graphical illustrations of the velocity fields are found in [39]. These oscillation frequencies are given by the gap between the ground state and the first excited state when mapping this internal Josephson junction onto an effective potential in Fock space [39, 40].

Bifurcation and symmetry breaking phase transition

The symmetry points of the plasma and π oscillations are stable fixed points in the phase space of the system. However, for $\Lambda > 1$ the value of ω_π becomes imaginary which indicates a critical point. The formerly stable fixed point on the equator of the Bloch sphere is replaced by an unstable fixed point and two new stable fixed points emerge at $\pm z_0 = \pm\sqrt{1-(1/\Lambda^2)}$. This phenomenon is called a pitchfork bifurcation and corresponds to a symmetry breaking phase transition [28]. For $\chi < 0$

the bifurcating fixed point correspond to the ground state of the system. At the bifurcation point the system switches over from a single ground state configuration to two equivalent degenerate lowest energy eigenstates. In terms of symmetry groups the Hamiltonian of the system has a $U(1) \times \mathbb{Z}_2$ symmetry. The $U(1)$ means that the Hamiltonian is not affected by a global phase in the wave function while the $\mathbb{Z}_2$ indicates an invariance under the transformation $z \to -z$ as the Hamiltonian is quadratic in z [41]. This symmetry is broken when the system randomly chooses the ground state at the positive or the negative value of z_0 and the symmetry reduces to $U(1) \times \mathbb{I}$.

In elongated condensates the single mode approximation is not valid and this symmetry breaking is the origin of a miscible-immiscible phase transition. For $\chi < 0$ and $\Lambda < 1$ the two components will overlap, i.e. they are miscible, because the ground state of the system corresponds to a state prepared on the isolated stable fixed point. When Λ is increased to $\Lambda > 1$ the symmetry is broken and one of the equivalent ground states at $\pm z_0$ is chosen spontaneously. As the single spatial mode approximation is not valid in elongated condensates different spatial regions will independently choose the $+z_0$ or $-z_0$ configuration and alternating domains each predominantly containing atoms of one or the other species will form. We now turn to the discussion of the ground state properties and excitation spectra properties of elongated binary Bose-Einstein condensates.

2.3. Ground state properties of elongated binary condensates

After having discussed the interplay of atomic interactions and a linear coupling field in the single spatial mode approximation we will now focus on two interacting species in a spatially extended system, in particular a one-dimensional waveguide. First, we will discuss the ground state properties of two-component Bose-Einstein condensates in the absence of the linear coupling, $\Omega = 0$. We will restrict ourselves to the case of equal atom numbers in the two components $N_1 = N_2$.

2.3.1. Homogeneous system without dressing

In a one-dimensional waveguide the ground state can either be a spatially uniform superposition of the two components or a phase separated one, where the two components occupy different regions and their overlap is minimized. The following energetic consideration allows to derive a criterion determining which configuration is energetically favorable.

For simplicity we ignore the kinetic energy contribution to the classical Hamiltonian Equation 2.2 and use a box potential of length L. The energy of the uniform superposition state with N_1 and N_2 atoms in the two components is given by [27, 42]

$$E_{\text{unif}} = \frac{g_{11}}{2}\frac{N_1^2}{L} + \frac{g_{22}}{2}\frac{N_2^2}{L} + g_{12}\frac{N_1 N_2}{L} \tag{2.6}$$

The corresponding expression for the phase-separated state reads

$$E_{\text{sep}} = \frac{g_{11}}{2}\frac{N_1^2}{L_1} + \frac{g_{22}}{2}\frac{N_2^2}{L_2} \tag{2.7}$$

The conditions of a fixed system size $L = L_1 + L_2$ and equal pressures $\partial E_{\text{sep}}/\partial L_1 = \partial E_{\text{sep}}/\partial L_2$ lead to

$$E_{\text{sep}} = \frac{g_{11}}{2}\frac{N_1^2}{L} + \frac{g_{22}}{2}\frac{N_2^2}{L} + \sqrt{g_{11}g_{22}}\frac{N_1 N_2}{L} \tag{2.8}$$

Thus the phase separated state is energetically favorable if

$$E_{\text{sep}} < E_{\text{unif}} \quad \Leftrightarrow \quad \sqrt{g_{11}g_{22}} < g_{12} \quad \Leftrightarrow \quad \Delta = \frac{g_{11}g_{22}}{g_{12}^2} < 1 \tag{2.9}$$

This is the condition for (im-)miscibility [27]: The ground state of two components consists of two separate phases, if their inter-species repulsion is stronger than the geometric mean of the intra-species repulsion strengths. Note that $\Delta < 1$ corresponds to $\chi < 0$ for the nonlinearity χ introduced in subsection 2.2.2. For the remainder of this section we will focus on the immiscible regime $\Delta < 1$, where the ground state consists of two separate domains.

The kinetic energy was neglected in the discussion above. Its inclusion leads to a non-zero width of the domain wall separating the two components. The characteristic width of the domain wall, the spin healing length ξ_s, can be determined in analogy to the single component healing length [27] by equating the quantum pressure due to kinetic energy with the interaction pressure at the domain wall

$$\frac{\hbar^2}{2m\sqrt{n_1}}\nabla^2\sqrt{n_1} + \frac{\hbar^2}{2m\sqrt{n_2}}\nabla^2\sqrt{n_2} = g_{11}n_1 + g_{22}n_2 - 2g_{12}\sqrt{n_1 n_2} \tag{2.10}$$

Assuming equal densities $n_1 = n_2 = n/2$ and identifying ξ_s with the characteristic length scale of density variations at the domain wall we yield[3]

$$\frac{\hbar^2}{m\xi_s^2} = \frac{n}{2}(g_{11} + g_{22} - 2g_{12}) \quad \Leftrightarrow \quad \xi_s = \frac{\hbar}{\sqrt{mng_s}} \tag{2.11}$$

with $g_s = \frac{1}{2}(g_{11} + g_{22} - 2g_{12})$.[4] Note that ξ_s takes on imaginary values in the immiscible regime, $g_s < 0$, where domain walls are stable. In the following we will always refer to $|\xi_s|$ when giving numerical values of the spin healing length.

The term ng_s corresponds to the energy contained in one domain wall due to the overlap of the two components. It sets an important energy scale of binary immiscible atomic clouds. As we will see in the remainder of this chapter many experimental observables in the context of the miscibility phase transition are directly related to this energy.

In summary, the ground state of an immiscible binary condensate consists of two domains each containing one component, separated by a domain wall. Although the Hamiltonian is translationally invariant, the ground state is not: The existence of two atomic components in separated regions breaks translational symmetry and the choice of which component populates which side of the domain wall is made spontaneously as both configurations are energetically equivalent [43]. The number of domain walls is minimized to one by the additional energy cost of each boundary. The width of the boundary is given by the spin healing length and depends on the value of the relevant interaction energy ng_s. The mean field ground states for both miscible and immiscible configurations are illustrated in Figure 2.2.

[3] In the limit $g_{11} \approx g_{22}$, this definition of the spin healing length is equivalent to the 'penetration depth' defined in [42]. The interaction parameters accessible in our experiments are all in the 'weakly segregated phase' discussed the same publication.

[4] g_s is (except for a factor $\hbar$) equivalent to the previous definition of χ which was used in order to obey the nomenclature conventions for internal Josephson junctions. In the context of miscibility in an elongated atomic cloud we will from now on use g_s.

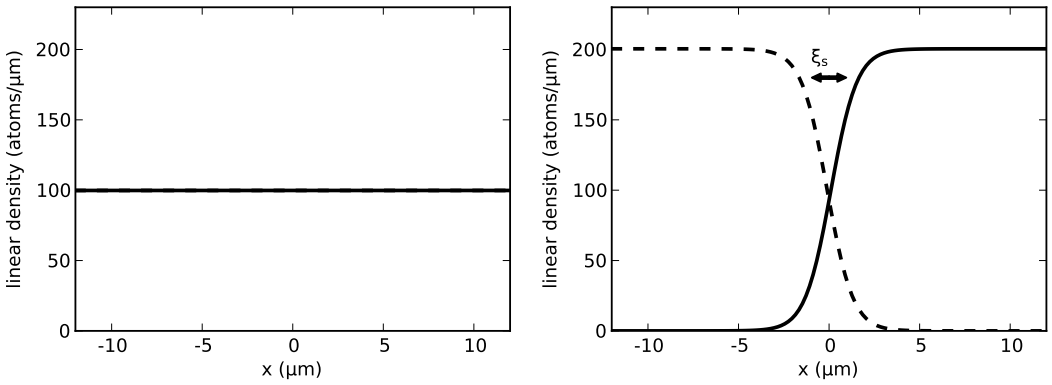

Figure 2.2.: Ground state density profiles of a miscible (left, $\Delta = 1.20$) and immiscible (right, $\Delta = 0.80$) homogeneous binary condensate. The width of the domain wall is given by the spin healing length ξ_s as illustrated in the right panel. The value of the spin healing lengths is $\xi_s = 1.91$ μm for the parameters used in this figure .

2.3.2. Homogeneous system with dressing

We will now include the effects of a linear coupling field on the ground state of the one-dimensional system. The linear coupling and its eigenstates, the dressed states, have been discussed in the single spatial mode approximation in subsection 2.2.1. The concept of dressed states has been generalized to dressed condensates in [44]. As we analyze the ground states properties, we choose the relative phase between linear coupling and the atoms such that the lower energy dressed state $|+\rangle$ is prepared. In the miscible regime $\Delta > 1$ the wave functions of the two components overlap and the previously discussed single mode case remains valid.

For immiscible parameters, $\Delta < 1$, the single mode approximation cannot be applied as the ground state consists of two separate domains in the absence of a linear coupling. It was shown theoretically that a linear coupling can tune the system to miscibility [17]. Above a critical coupling strength $\Omega_c = -ng_s$ the mean field ground state density profiles of the two components overlap and cannot be distinguished from a miscible system. The numerically computed ground state density profiles for various values of Ω are illustrated in the left panel of Figure 2.3. As Ω increases the domain wall widens and the background density far from the domain wall increases. When crossing the critical point the density profiles of the two components become flat and the system becomes miscible.

In order to understand these numerical observations we recall the bifurcation occurring in the single spatial mode approximation (see subsection 2.2.2). As the stable fixed points correspond to energy minima they predict the imbalance of the ground state [45]. When assuming an equal population of the two components $N_1 = N_2$ translational symmetry is broken and one component will predominate on the left side of the domain wall, while the right side is occupied by the other component.[5] The imbalance far from the domain wall is given by the prediction of the bifurcation

$$z_0 = \pm\sqrt{1 - (1/\Lambda)^2} = \pm\sqrt{1 - (\Omega/\Omega_c)^2} \tag{2.12}$$

This prediction is in excellent agreement with the numerical findings as shown in the right panel of

[5]Due to the linear coupling only the total atom number is conserved but not the individual populations N_1 and N_2 (see [45] for an in-depth discussion). However, as we are interested in the width of the domain wall in the presence of a linear coupling we fix the atom numbers to be equal. In addition we assume equal intra-species scattering lengths $a_{11} = a_{22}$.

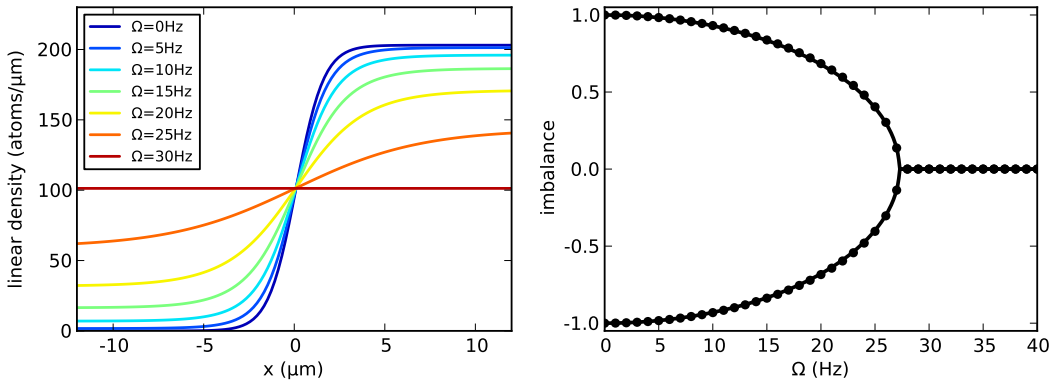

Figure 2.3.: (left) Numerically computed ground state density profiles near the domain wall for various linear coupling strengths. For clarity only the density of one component is drawn. The profile of the other component is obtained by reflection along $x = 0$. The width of the domain wall increases as Ω approaches Ω_c, which is 27.3 Hz for the chosen parameters. When exceeding the critical coupling strength the system becomes miscible. (right) The imbalance of the computed ground state profiles far from the domain wall (black circles) is compared to the analytical single mode prediction (solid line). The excellent agreement confirms that the ground state imbalance is given by the fixed points of the bifurcation.

Figure 2.3.

The presence of the linear coupling field reduces the energy of the uniform superposition state by $\hbar\Omega$ [46] and thus reduces the energy contained in a domain wall by this value. In analogy to the previous subsection 2.3.1 the resulting width of the domain wall can be calculated as

$$\frac{\hbar^2}{m\xi_s^2} = ng_s + \hbar\Omega \quad \Leftrightarrow \quad \xi_s = \frac{\hbar}{\sqrt{m(ng_s + \hbar\Omega)}} = \frac{\hbar}{\sqrt{m(\hbar\Omega - \hbar\Omega_c)}} \tag{2.13}$$

The effective spin healing length increases with Ω and diverges as $\Omega \to \Omega_c$. At this point the system transitions to miscibility and the two components overlap spatially.

2.3.3. Effects of a trapping potential

In the presence of a longitudinal trapping potential translational symmetry is broken as the sum density of the two components is not homogeneous anymore. This symmetry breaking changes the ground state and it takes on the symmetry of the trap due to the density dependence of the interaction energy $g_{ii}n_i$. Assuming $a_{11} > a_{22}$, component 1 will prefer lower densities than component 2 and occupies the edges of the trap while component 2 populates the trap center [47, 48]. In the immiscible regime this asymmetry in the intra-species scattering lengths can compensate the energy cost of a second domain wall. This situation is depicted in the right panel of Figure 2.4.

This three-domain ground state has the same symmetry as the trap in contrast to the symmetry broken two-domain state, in which one component occupies the left half of the trap and the other component the right half. For most configurations of the relative interaction strengths and atom numbers the three-domain ground is lower in energy than the two-domain state. A detailed discussion and categorization of the possible ground state configurations is found in [49].

The presence of the trap does not affect the width of the domain walls as long as ξ_s is a lot smaller

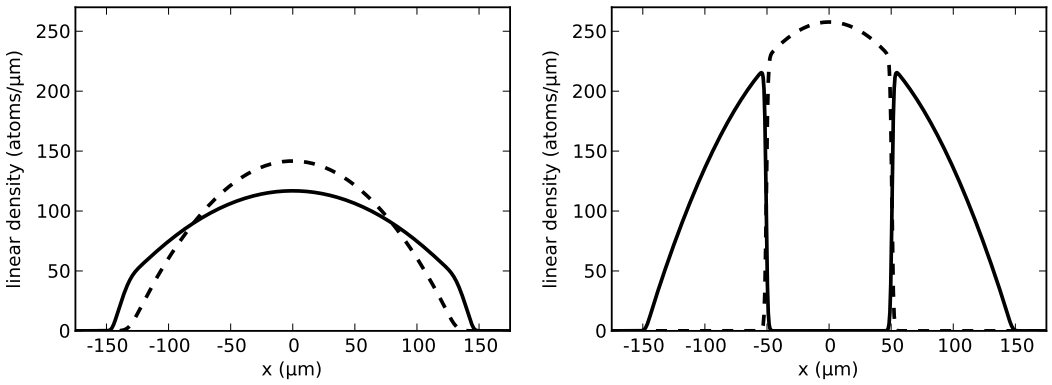

Figure 2.4.: Ground state density profiles of a miscible (left, $\Delta = 1.20$) and immiscible (right, $\Delta = 0.80$) binary condensate in the presence of a harmonic trapping potential. Due to $a_{11} > a_{22}$ the first component (solid lines) is pushed to the outer regions of the trap with a lower density while the other component (dashed lines) prevails in the trap center. This effect reduces the overlap of the two components for miscible parameters (left), a phenomenon that does not occur in a homogeneous system. In the immiscible case the asymmetry in intra-species scattering lengths leads to a ground state consisting of three-domains.

than the extent of the atomic clouds in the trap [42]. However, due to the inhomogeneous density profile ξ_s depends on the position of the domain wall relative to the trap center.

For miscible scattering parameters and in the absence of a trapping potential the overlap of the two components is perfect also for an asymmetry in the relative values of a_{11} and a_{22}. However, in the presence of a trap such an asymmetry causes different density profiles of the atomic clouds and their overlap is reduced as shown in the left panel of Figure 2.4. In contrast to phase separation, which requires immiscible interaction parameters, this effect is referred to as *potential separation* [43] as it occurs only in the presence of an external potential.

2.4. Bogoliubov theory

After the discussion of the ground state properties of binary interacting condensates we will now focus on their excitation spectra. The excitation spectrum can be calculated using a linear response analysis of the Gross-Pitaevskii equation and diagonalizing the resulting set of equations by employing the Bogoliubov transformation. This approach is the classical counterpart to Bogoliubov theory, which describes elementary excitations as bosonic quasiparticles whose vacuum is given by the unperturbed condensates [27]. We stress that this analysis is based on the mean field approximation and valid only in the linear response of the system, i.e. small deviations from the unperturbed condensates.

The notion of immiscibility of the two components in the ground state is related to a modulational instability of a uniform superposition of the two components. Unstable modes in the excitation spectrum have imaginary eigenenergies and thus grow exponentially in time. Initial work on single component condensates associated the appearance of unstable modes with attractive atomic interactions, which manifest themselves for example in the formation of a train of solitons [50]. The Bogoliubov approach has been generalized to two-component condensates, where effective attrac-

tive interactions can appear although all atomic interactions are repulsive [51, 52, 43].[6] This section summarizes the Bogoliubov spectra of binary condensates, which can be derived analytically for homogeneous one-dimensional systems. We begin with a simple linearization of the equations of motion yielding the characteristic length scales of the excitation modes. Then, we discuss the full spectrum of elementary excitations in the absence of a linear coupling field and include its effects later on. As previously, we will restrict the discussion to the case of repulsive interactions, $g_{ij} > 0$.

2.4.1. Linearization of the equations of motion

Following the ansatz presented in the appendices of [55, 56] many properties such as stability or characteristic length and energy scales can be deduced by linearizing the equations of motion around a stationary state. We begin the analysis by inserting $\psi_i = \psi_i^0 + \sqrt{n}\delta\psi_i$ into Equation 2.3, where ψ_i^0 denotes the real valued background wave function of component i and $\delta\psi_i$ is a small perturbation around it. Using the stationary character of the background state[7] $i\hbar\frac{\partial\psi_i^0}{\partial t} = \mu_i\psi_i^0$ and ignoring all terms of second or higher order in $\delta\psi_i$ we obtain the equations of motion for the perturbations

$$\frac{\hbar^2}{2m}\nabla^2\delta\psi_i = \sum_k S_{ik}\delta\psi_k \tag{2.14}$$

with

$$S = \begin{pmatrix} ng_{11} + \hbar\Omega/2 & ng_{12} - \hbar\Omega/2 \\ ng_{12} - \hbar\Omega/2 & ng_{22} + \hbar\Omega/2 \end{pmatrix} \tag{2.15}$$

The matrix S can be diagonalized by CSC^{-1} with the eigenvalues

$$\Gamma_\pm = \frac{1}{2}\left(\hbar\Omega + ng_{11} + ng_{22} \pm \sqrt{(ng_{11} - ng_{22})^2 + (2ng_{12} - \hbar\Omega)^2}\right) \tag{2.16}$$

The first term in the square root is a lot smaller[8] than the second one and can be neglected leading to

$$\Gamma_\pm = \frac{1}{2}n(g_{11} + g_{22} \pm 2g_{12}) + \frac{1}{2}(\hbar\Omega \mp \hbar\Omega) \tag{2.17}$$

The signs of the eigenvalues $\Gamma_\pm$ act as a stability signature of the system [52]. If all eigenvalues are positive the system is stable, while a negative eigenvalue indicates an instability. The physical reason for this correspondence is that small fluctuations $\delta\psi_i$ can decrease the energy of the system and thus grow exponentially if S has a negative eigenvalue [52]. Furthermore the nature of the excitations can be deduced from a similar energetic consideration: If all atomic interactions are repulsive but fulfill the immiscibility condition Equation 2.9, the unstable modes locally increase the atom number difference with constant sum density (out-of-phase mode), while an instability due to attractive interactions, $g_{12} < 0$, tends to increase the local sum density (in-phase mode) [52].

We consider the characteristic length scale ξ of the perturbations in the eigenbasis of S given by $\delta\bar{\psi}_i = \sum_k C_{ik}^{-1}\delta\psi_k$. This ansatz leads to

$$\xi^2\nabla^2\delta\bar{\psi}_i = \delta\bar{\psi}_i \tag{2.18}$$

[6] The (im-)miscibility condition Equation 2.9 was first derived in this context [53, 54].

[7] We assume an equal superposition of the two components as the background state, which is stationary but unstable for a homogeneous system with immiscible scattering parameters. In the presence of a trapping potential and $a_{11} \neq a_{22}$ a stationary background state is difficult to realize.

[8] About a factor 1000 for ^{87}Rb and taking into account the values of g_{12} and Ω we can realize in our experiments.

with

$$\xi^2 = \frac{\hbar^2}{2m\Gamma_\pm} \tag{2.19}$$

In the following we focus on the smallest eigenvalue Γ_- resulting in

$$\xi = \xi(\Omega) = \frac{\hbar}{\sqrt{2m(ng_s + \hbar\Omega)}} \tag{2.20}$$

In the absence of linear coupling ξ recovers the spin healing length defined in Equation 2.11, $\xi(\Omega = 0) = \xi_s/\sqrt{2}$. Furthermore ξ diverges at the critical coupling strength $\hbar\Omega_c = -ng_s$. For $\Omega < \Omega_c$, ξ is imaginary and the unstable solutions of Equation 2.18 are sinusoidal with a wave vector $k = 1/\xi$, i.e. a wavelength of $\lambda = 2\pi\xi$. In the case $\Omega > \Omega_c$, ξ is real and the stable solutions of Equation 2.18 are exponential functions with length scales of ξ. Thus ξ plays the role of a correlation length.

After this simplified linearization approach we will discuss the full dispersion of the excitations resulting from a mean field Bogoliubov analysis in the following section.

2.4.2. Bogoliubov spectrum of a homogeneous system

In the absence of an external trapping potential the excitation spectrum of a single condensate of atoms in state i is given by [27]

$$\hbar^2\omega^2(k) = \tilde{c}_i^2\hbar^2k^2 + \left(\frac{\hbar^2k^2}{2m}\right)^2 \tag{2.21}$$

where $\tilde{c}_i = \sqrt{n_i g_{ii}/m}$ is the sound velocity, k the wave vector of the excited mode and $\hbar\omega$ the corresponding excitation energy. The dispersion starts linearly for small k and becomes quadratic as k increases, respectively corresponding to the phonon and the free particle regimes of the quasiparticle excitations [27].

The dispersion of two interacting condensates can be written in the same form [43, 57, 58]

$$\hbar^2\omega_\pm^2(k) = c_\pm^2\hbar^2k^2 + \left(\frac{\hbar^2k^2}{2m}\right)^2 \tag{2.22}$$

where the sound velocities $c_\pm$ are calculated from the single condensate sound velocities $\tilde{c}_i$ by

$$c_\pm^2 = \frac{1}{2}\left[(\tilde{c}_1^2 + \tilde{c}_2^2) \pm \sqrt{(\tilde{c}_1^2 - \tilde{c}_2^2)^2 + 4(g_{12}^2/g_{11}g_{22})\tilde{c}_1^2\tilde{c}_2^2}\right] \tag{2.23}$$

The spectrum consists of two branches $\omega_\pm$ depicted in Figure 2.5. ω_+ is higher in energy because $c_+^2 > c_-^2$. In the absence of inter-species interactions, $g_{12} = 0$, the two atomic clouds are independent of each other and the two branches reduce to the dispersions of each condensate given by Equation 2.21. In the case $g_{12} \neq 0$ excitations on top of the two atomic species are not independent of each other and become coupled. The upper branch ω_+ describes in-phase excitations on the two components, i.e. excitations on the sum density such as breathing where both components move in unison. It is also called the 'stiff mode'. The lower branch ω_- represents the dispersion of out-of-phase modes, i.e. excitations on the difference density of the two components. They are referred to as spin excitations or 'soft modes' [59, 41]. In consequence the spectrum of two interacting condensates does not describe excitations on top of the single components but rather on their sum or difference density.

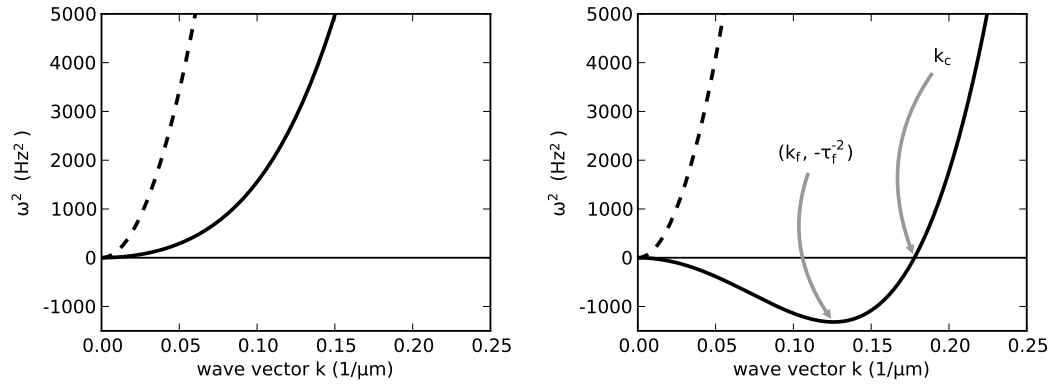

Figure 2.5.: Bogoliubov spectra in the miscible ($\Delta > 1$, left panel) and immiscible ($\Delta < 1$, right panel) regimes. Dashed lines represent sum density excitations ω_+^2 and solid lines correspond to spin excitations described by ω_-^2. In the immiscible case the eigenenergies of long wavelength spin excitations with $k < k_c$ become imaginary indicating a modulational instability. The fastest growing mode k_f and its growth rate τ_f are depicted.

If the condition for immiscibility Equation 2.9 is fulfilled, c_-^2 becomes negative resulting in imaginary excitation energies. Thus the amplitudes of long wavelength modes $0 < k < k_c = 2m|c_-|/\hbar$ grow exponentially [43, 58]. This phenomenon is referred to as modulational instability, because weak perturbations on the background state cause the subsequent exponential growth of excitation modes in a given range of wavelengths [58]. The fastest growing mode is determined from the minimum of ω_-^2 resulting in $k_f = k_c/\sqrt{2} = \sqrt{2}m|c_-|/\hbar$ and a growth rate of $1/\tau_f = |\omega_-(k_f)| = m|c_-|^2/\hbar$. These quantities are illustrated in Figure 2.5.

For small differences in the scattering lengths $a_{11} - a_{22} \ll a_{11}, a_{22}, a_{12}$, as it is the case for ^{87}Rb, Equation 2.23 can be written as

$$c_\pm^2 = \frac{1}{4}\frac{n}{m}(g_{11} + g_{22} \pm 2g_{12}) \tag{2.24}$$

This simplification changes the values of $c_\pm$ by less than 10^{-3} for our experimental parameters. The equation

$$mc_-^2 = \frac{1}{2}ng_s = \frac{\hbar^2}{2m}\frac{1}{\xi_s^2} \tag{2.25}$$

relates the properties of the excitation spectrum to the characteristic length scale of the ground state, the spin healing length, via

$$k_c = 2m|c_-|/\hbar = \sqrt{2}/\xi_s \quad \text{and} \quad k_f = k_c/\sqrt{2} = 1/\xi_s \tag{2.26}$$

2.4.3. Bogoliubov spectrum of a dressed system

The Bogoliubov theory for binary condensates has been expanded to include a linear coupling between the components [51, 45, 41, 46]. It was found that a linear coupling field can stabilize the spin excitation branch, which is unstable in the case of immiscible scattering parameters. In addition the dispersion becomes gapped in the long-wavelength limit $k \to 0$ resulting in massive excitation modes. This section summarizes the results of Tommasini et al. [41] and reformulates them in terms of experimental quantities.

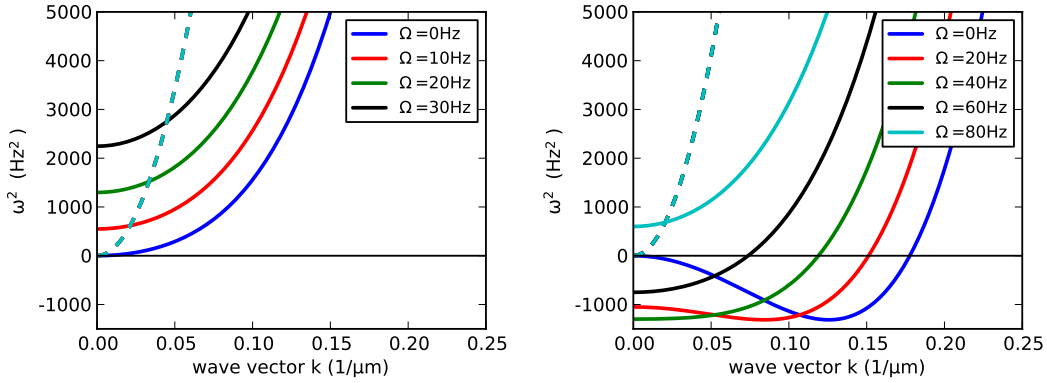

Figure 2.6.: Bogoliubov spectra in the miscible ($\Delta > 1$, left panel) and immiscible ($\Delta < 1$, right panel) regime for various amplitudes of the linear coupling Ω. Sum density excitations (ω_+^2, dashed lines) are independent of Ω. For miscible parameters the linear coupling introduces an energy gap in the long wavelength limit $k \to 0$. In the immiscible regime an increasing coupling strength shifts the instability of the spin excitations (ω_-^2, solid lines) towards smaller wave vectors until the system is stable. A further increase of Ω additionally creates an energy gap. The crossing of the branches is physical only if $a_{11} = a_{22}$; otherwise the two branches become coupled resulting in an avoided crossing.

The two branches of the excitation spectrum in the presence of a linear coupling are given by [41]

$$\begin{aligned} \hbar^2\omega_+^2(k) &= c_2^2\hbar^2k^2 + e_k^2 \\ \hbar^2\omega_-^2(k) &= c_1^2\hbar^2k^2 + e_k^2 + g^2 \end{aligned} \tag{2.27}$$

with

$$e_k = \frac{\hbar^2k^2}{2m} \tag{2.28}$$

$$g^2 = G_{11}n\hbar\Omega + (\hbar\Omega)^2 \tag{2.29}$$

the sound velocities

$$c_1^2 = \frac{G_{11}n}{2m} + \frac{\hbar\Omega}{m} \qquad c_2^2 = \frac{G_{22}n}{2m} \qquad c_{12}^2 = \frac{G_{12}n}{2m} \tag{2.30}$$

and the dressed interaction constants

$$G_{11} = \frac{1}{2}(g_{11} + g_{22} - 2g_{12}) \qquad G_{22} = \frac{1}{2}(g_{11} + g_{22} + 2g_{12}) \qquad G_{12} = \frac{1}{2}(g_{22} - g_{11}) \tag{2.31}$$

In the absence of a linear coupling field, $\Omega = 0$, Equation 2.27 collapses to Equation 2.22.[9] However, for $\Omega \neq 0$ the dispersion for the spin excitation branch ω_- qualitatively deviates from the previous expressions as it acquires an energy gap g at $k = 0$. The excitation spectra for both miscible and immiscible scattering parameters and various coupling strengths are shown in Figure 2.6.

In excitation spectra without instabilities the branches for the sum density and the spin excitations

[9]Note that due to the use of the dressed interaction constants G_{ij}, the sound velocities c_1 and c_2 correspond to c_- and c_+ used in the previous discussion of the undressed case (rather than $\tilde{c}_1$ and $\tilde{c}_2$). However, the relevant expressions $(c_1^2 + c_2^2)$ and $((c_1^2 - c_2^2)^2 + 4c_{12}^4)$ have the same values for c_i and $\tilde{c}_i$.

cross because $g^2 > 0$ and $c_1^2 < c_2^2$. However, different intra-species coupling strengths $a_{11} \neq a_{22}$ couple the density and spin excitations. This leads to a hybridization of the modes and the branches are separated by an avoided crossing [46]. An example of hybridized modes is illustrated in the right panel of Figure 2.7. It is calculated using [41]

$$\hbar^2\omega_\pm^2(k) = \frac{1}{2}\Big(2e_k^2 + (c_1^2 + c_2^2)\hbar^2k^2 + g^2 \pm\sqrt{[(c_1^2 - c_2^2)^2 + 4c_{12}^4]\hbar^4k^4 + 2[2j_\alpha^2 + (c_1^2 - c_2^2)g^2]\hbar^2k^2 + g^4}\Big) \quad (2.32)$$

with

$$j_\alpha^2 = \frac{G_{12}^2 n^2 \hbar\Omega}{2m} \quad (2.33)$$

In the following we will discuss the properties of the excitation spectra shown in Figure 2.6. For simplicity we will use the unhybridized dispersion relations given by Equation 2.27 for calculations. This can be done as the modifications due to the hybridization are relevant only close to the avoided crossing and do not affect the results. The sum density excitations ω_+ are not affected by the linear coupling and our discussion will focus on the spin excitations. In the miscible regime $\Delta > 1$ the presence of a linear coupling causes an energy gap g at $k = 0$ in the excitation spectrum. In addition the dispersion starts quadratically for small k and thus corresponds to a 'massive' mode, i.e. a finite amount of energy is required to excite the system.

Another important consequence of the gap is a finite reaction time of the system to sudden quenches which populate excited modes. The time evolution of each excited mode is given by its energy $\hbar\omega_-$. Thus, a finite value of the gap introduces a characteristic time scale for the evolution of the excitations. The implications of this finite reaction time will be discussed in chapter 5 and chapter 6.

For immiscible scattering parameters $\Delta < 1$ the linear coupling shifts the region of unstable modes towards longer wavelengths. If it exceeds a critical value $\Omega > \Omega_c$ all eigenenergies are real and the system becomes stable. Similarly to the miscible case the spin excitation branch acquires an energy gap. For values $\Omega_c/2 < \Omega < \Omega_c$, the most unstable mode is given by $k = 0$. The critical coupling strength Ω_c marks the transition from an unstable system to a stable one as already seen in the discussion of the ground state properties in subsection 2.3.2. This miscible-immiscible phase transition will be one of the main topics of this thesis. The value of Ω_c can be calculated from the vanishing of the energy gap given in Equation 2.29. The condition $g(\Omega_c) = 0$ yields

$$\hbar\Omega_c = -nG_{11} = -\frac{1}{2}n(g_{11} + g_{22} - 2g_{12}) = -ng_s \quad (2.34)$$

in agreement with the previous result in the context of the ground state properties.

In terms of the critical coupling strength the gap can be written as

$$g^2 = G_{11}n\hbar\Omega + (\hbar\Omega)^2 = \hbar\Omega(\hbar\Omega - \hbar\Omega_c) \quad (2.35)$$

In the single spatial mode limit $k = 0$ the system reduces to the internal Josephson junction discussed in subsection 2.2.2. In this context the gaps in the miscible and immiscible cases corresponds to the frequencies of plasma and π oscillations, respectively.[10] The real and imaginary parts of the

[10] The anharmonicity of plasma and π oscillations for large amplitudes is not captured in the Bogoliubov theory as it is valid only in the linear response, i.e. small deviations from the stationary state.

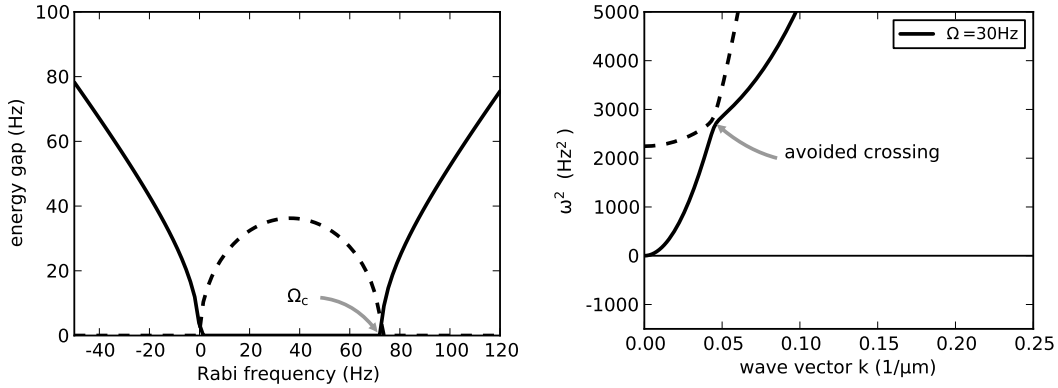

Figure 2.7.: (left) Real (solid line) and imaginary (dashed line) parts of the energy gap vs the linear coupling strength. The critical coupling Ω_c marks the transition from an immiscible to a miscible system. (right) Example of the dispersion of hybridized modes for the case $a_{11} \neq a_{22}$. The crossing of the two branches is avoided.

gap for immiscible scattering parameters are plotted in the left panel of Figure 2.7.

Physical mechanism for stabilization by dressing

The physical mechanism for the stabilization of an immiscible system by a linear coupling field can be visualized intuitively in analogy to a spin chain interacting with a magnetic field. The homogeneous two-component system can be thought of as an array of pseudo-spins in analogy to the Bloch sphere picture of a two level system in a single spatial mode (see section 2.2). We associate an atom of component 1 with spin-down and an atom of component 2 with spin-up. Consequently an equal superposition of the two components corresponds to a horizontal spin vector. The emergence of spin domains during the demixing dynamics of an initial superposition state can be visualized as a local rotation of the spins out of the horizontal plane towards one of the poles.

As discussed in subsection 2.2.1 a resonant linear coupling of the two components corresponds to a rotation of the spin around an axis through the equator. The preparation of a dressed state the rotation axis is aligned parallel with the atomic pseudo-spin. This configuration is analogous to an array of spins aligned in an external magnetic field. If the effective magnetic field associated with the linear coupling is strong enough, i.e. $\Omega > \Omega_c$, the spins stay aligned with the axis of the linear coupling. A rotation away from the rotation axis and thus demixing of the two components is suppressed.

Connection of ground state properties to Bogoliubov spectra

Characteristic length scales of the excitation spectra are the wave vectors of the most unstable mode k_f and of the unstable mode with the smallest wavelength k_c. In the previous section we have related these modes to the spin healing length in the absence of a linear coupling field. We will now perform a similar analysis including the linear coupling.

The sound velocity c_1 can be written in terms of the critical coupling as

$$c_1^2 = \frac{G_{11}n}{2m} + \frac{\hbar\Omega}{m} = \frac{1}{m}(\hbar\Omega - \hbar\Omega_c/2) \tag{2.36}$$

Using Equation 2.35 and Equation 2.36 the spin branch of the excitation spectrum can be expressed

in terms of Ω and Ω_c resulting in

$$\hbar^2\omega_-^2 = \left(\frac{\hbar^2k^2}{2m}\right)^2 + \frac{\hbar^2k^2}{2m}(2\hbar\Omega - \hbar\Omega_c) + \hbar\Omega(\hbar\Omega - \hbar\Omega_c) \tag{2.37}$$

The values for k_f and k_c can be calculated using the conditions $\frac{d\omega_-}{dk} = 0$ and $\omega_- = 0$, respectively, leading to

$$k_f = \sqrt{2m/\hbar}\sqrt{\Omega_c/2 - \Omega} \quad \text{and} \quad k_c = \sqrt{2m/\hbar}\sqrt{\Omega_c - \Omega} \tag{2.38}$$

Comparing these expressions to the spin healing length derived from the ground state in the presence of a linear coupling Equation 2.13, the relation $k_c = \sqrt{2}/\xi_s$ still holds. This characteristic length scale changes proportional to $(\Omega_c - \Omega)^{-1/2}$ and this scaling behavior will be discussed in the context of phase transitions in chapter 5.

Imbalance effects

In order to estimate the sensitivity of the excitation spectrum to experimental imperfections we analyze the effect of different populations in the two atomic clouds, i.e. a non-zero imbalance $z = \frac{N_2 - N_1}{N_1 + N_2}$. This effect is relevant for experiments because a small detuning of the linear coupling or an imperfect preparation pulse directly translate to a population imbalance (see also subsection 2.2.1). In addition this analysis provides a crude estimation for the excitation spectra beyond linear response. When unstable spin excitations grow they create density modulations on the atomic density profiles. The Bogoliubov theory discussed in this section is valid only in the linear response regime, i.e. if the modulation depth is small compared to the atomic background density. As the excitations create local imbalances the effect on the dispersion relations can be roughly estimated by considering an imbalanced system.

The excitation spectra of imbalanced systems in the immiscible regime are shown in Figure 2.8 for various values of z and both without and with a linear coupling. As an imbalance reduces the effective overlap of the two components it leads to a smaller effective interaction parameter ng_s. Thus the unstable region is shifted towards larger wavelengths and the growth rates become slower. In the presence of a linear coupling this effect is amplified because a smaller effective ng_s additionally reduces the critical coupling strength and thus increases the relevant parameter $\Omega - \Omega_c$ for a given value of Ω. The imbalance in our experiments is typically $-0.2 < z < 0.2$ and changes the excitation spectra by less than 10%.

2.4.4. Effects of a trap and numerical Bogoliubov-de Gennes analysis

The presented analytical Bogoliubov theory requires a homogeneous one-dimensional system. In experiments the atomic clouds are confined in an elongated trap and thus inhomogeneous and of finite size. If the spatial extent of the atomic cloud is large compared to the characteristic length scale of the excitations given by k_f, the system can be treated as locally homogeneous and the homogeneous theory is expected to be a reasonable approximation. We will now analyze the deviations of the excitation spectra for harmonically trapped condensates from the homogeneous case by employing a numerical Bogoliubov - de Gennes stability analysis (see subsection B.2.2). As the numerical analysis requires a stationary background state we assume equal values for the intra-species scattering lengths $a_{11} = a_{22}$. For an absolute comparison of the length scales and growth rates we choose a density for the analytical calculations corresponding to about 90% of the maximum density of the inhomogeneous cloud.

Figure 2.9 compares the analytical theory to the numerical results for two different experimental

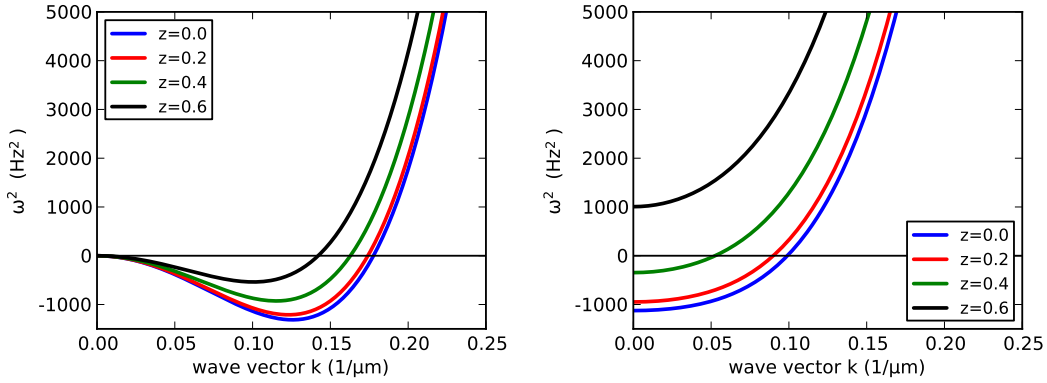

Figure 2.8.: Excitation spectra for different values of the imbalance z and for immiscible scattering parameters $\Delta < 1$. In the absence of a linear coupling (left) the effect of an imbalance is less pronounced than in the presence of a coupling field with $\Omega = 50\,\mathrm{Hz} = 0.7\,\Omega_c$ (right). Typical experimental imbalances are $-0.2 < z < 0.2$ which cause only minor changes in the excitation spectrum. The corrections for different imbalances are the symmetric for $\pm z$.

configurations in optical dipole traps we refer to as 'waveguide' and 'charger' (see section 3.1 for details on the experimental setup). While elementary excitation form a continuous spectrum in the homogeneous case the spectrum becomes discrete for a finite size system. The density of excitation modes in k-space is directly given by the size of the experimental system. This effect is apparent in the results for the charger (right panel of Figure 2.9), in which the atomic cloud has a longitudinal size of about 40 µm.

The finite number of available modes affects the demixing dynamics, which is dominated by the modes with the largest growth rates. In large atomic clouds many modes have similar growth rates and the emerging spin pattern is random depending on small variations of the initial seed of the modes. In contrast, only two or three excitation modes dominate the dynamics in the charger and the shot-to-shot fluctuations in the spin pattern will be small. In other words, the boundary conditions given by the finite size of the system pin the positions of the spin domains if the size of the domains is not much smaller than the extent of the atomic cloud.

Besides the discreteness of the spectrum the numerical results for the charger also deviate significantly in the wave vectors and the growth rates of the unstable modes. They are shifted towards smaller wavelengths and the growth rates are increased. This effect significantly modifies the demixing dynamics in the charger compared to the analytical predications.

In summary the properties of atomic clouds confined in the charger deviate significantly from the homogeneous theory while the results for the waveguide agree well with the analytical predictions. This justifies the use of the Bogoliubov theory for a homogeneous system to model the experimental observations in the waveguide presented in this thesis.

2.5. Extension to negative coupling strengths

In the previous discussion about the excitation spectra we have assumed a relative phase between the linear coupling and the atoms of $\varphi = 0$. In the limit of strong linear coupling this configuration corresponds to the $|+\rangle$ state, i.e. the ground state of the system (see subsection 2.2.1). The stationarity of $|+\rangle$ for $\Omega \gg \Omega_c$ implies a stable system and the absence of unstable modes in the excitation

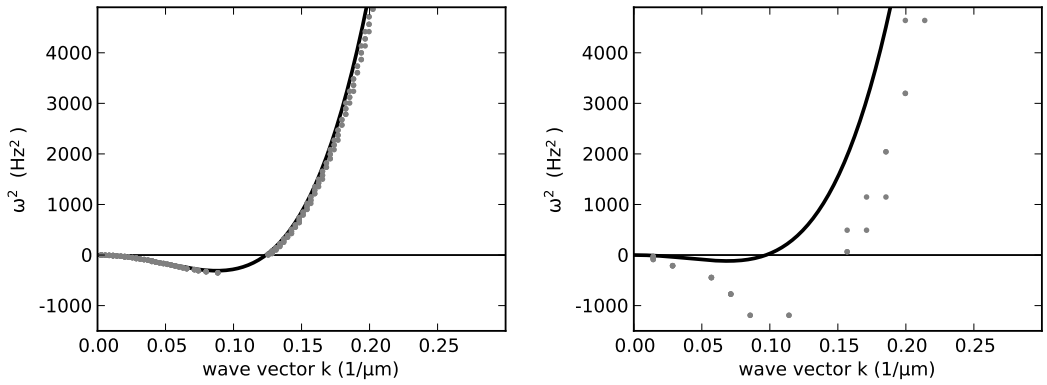

Figure 2.9.: Comparison of the analytical Bogoliubov theory for a homogeneous system to the results of a numerical Bogoliubov-de Gennes analysis for typical experimental configurations in the waveguide (left) and the charger (right). While the excitation spectrum for an atomic cloud in the waveguide agrees well with the predications for the homogeneous system it deviates significantly in the charger. In particular the discrete nature of the spectrum for the finite size system becomes apparent by the separation of the modes in k-space. The mode density is given by the size of the atomic cloud and does not depend on numerical parameters such as the spatial extent of the grid or the number of grid points used for the computation.

spectrum. As Ω is reduced and the strong coupling limit breaks down, $|+\rangle$ is not stationary anymore and excitation modes become unstable for $\Omega < \Omega_c$. However, one can similarly determine the excitation spectrum for a relative phase of $\varphi = \pi$ corresponding to the $|-\rangle$ state. As this is an excited state additional instabilities appear in the spectrum of the homogeneous system, which will be discussed in this section.

As in subsection 2.2.1 we have associated different choices of φ with the preparation of different states. However, as φ is the *relative* phase, i.e. the difference between the atomic phase and the phase of the linear coupling, it can also be incorporated in the Hamiltonian instead of the prepared state. In this picture the same initial state is prepared but subsequently evolves under different Hamiltonians. This equivalence can be understood by comparing the respective actions of the resonant linear coupling Hamiltonian H_{cpl} Equation 2.2 on the different atomic states:[11]

$$\begin{aligned} H_{\text{cpl}}(\varphi = 0)|-\rangle &= -\frac{1}{2}\hbar(+\Omega)(\psi_1^*\psi_2 + \psi_2^*\psi_1)|-\rangle \\ &= -\frac{1}{2}\hbar(-\Omega)(\psi_1^*\psi_2 + \psi_2^*\psi_1)|+\rangle \\ &= H_{\text{cpl}}(\varphi = \pi)|+\rangle \end{aligned} \tag{2.39}$$

The first expression incorporates $\varphi = \pi$ in the phase of the atomic components resulting in the $|-\rangle$ state. The last term includes the value of φ in the Hamiltonian and suggests an alternative interpretation of the configuration: We can assume that the system is always prepared in the $|+\rangle$ state and subsequently evolves under the action of different Hamiltonians. The two phases $\varphi = 0$ and $\varphi = \pi$ of the linear coupling can be interpreted as positive or negative values of Ω. When using

[11]The other terms of the Hamiltonian H_0 and H_{int} do not contain terms $\psi_i^*\psi_j$ with $i \neq j$. Thus, their actions on the $|+\rangle$ and the $|-\rangle$ states are identical.

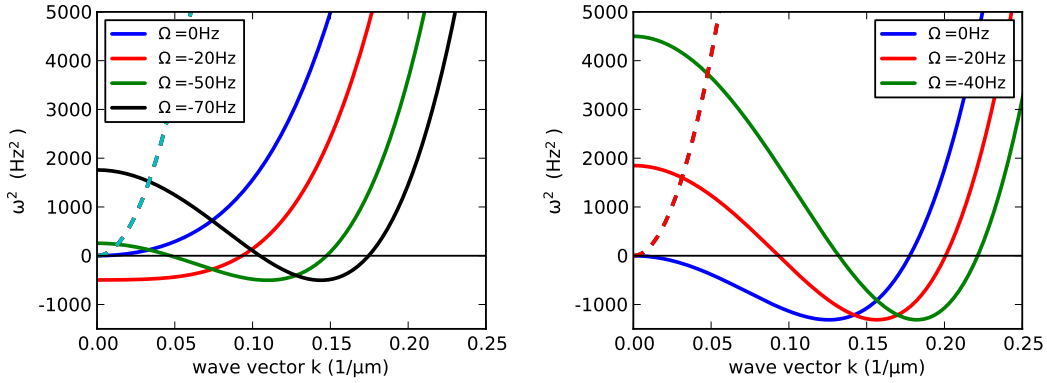

Figure 2.10.: Excitation spectra in the miscible (left) and immiscible (right) regime in the presence of a linear coupling field with $\Omega < 0$. (left) For miscible parameters long wavelength modes become unstable and the instability is shifted towards shorter wavelength modes in the same way as for $0 < \Omega < \Omega_c$ in the immiscible regime (see Figure 2.6). (right) In the immiscible regime the unstable modes are shifted towards short wavelengths while long-wavelength excitations become stable again and the $k = 0$ mode acquires a gap.

the concept of negative Ω it is redundant to distinguish between the preparation of two states. Preparing a $|+\rangle$ state and evolving it with $+\Omega_0$ ($-\Omega_0$) in the Hamiltonian is equivalent to preparing a $|-\rangle$ state and subsequently choosing $-\Omega_0$ ($+\Omega_0$).

This picture of an effective negative coupling strength has the advantage that quantities depending on Ω can be plotted in a single graph having one unambiguous axis for Ω. We will use this notation in the remainder of this thesis. However, it is important to remember that the corresponding eigenstate is not the lowest energy state.

The excitation spectra for negative values of linear coupling strength can be obtained directly by using values $\Omega < 0$ in the formulae in subsection 2.4.3. Examples of dispersion relations for various negative values of Ω are shown in Figure 2.10 both for miscible and immiscible scattering parameters. In the immiscible case the instability is shifted towards shorter wavelength modes while long wavelength modes are stabilized. An energy gap appears at $k = 0$, which corresponds to plasma oscillations of the Josephson Hamiltonian (see subsection 2.2.2). A system that is miscible in the absence of a linear coupling attains unstable modes for negative values of Ω. Similarly to the immiscible case long wavelength modes become unstable first and the instability is shifted towards smaller wavelengths as Ω is decreased.

The change in the spectrum of unstable modes with the coupling strength is summarized in Figure 2.11. The square-root scaling of the characteristic size of the unstable modes is smoothly continued as Ω becomes negative. Thus measurements of the mean field scaling behavior can be extended to negative coupling strengths in order to increase the dynamic range. The miscible case shows the same characteristic scaling of the instability region, but it is shifted towards smaller values of Ω. The system becomes unstable for $\Omega < 0$ (in analogy to $\Omega < \Omega_c$ in the immiscible case) and the $k = 0$ mode becomes stable again for $\Omega < \Omega_c < 0$ (in analogy to $\Omega < 0$). The width of the instability region is constant for different values of k and given by $|\Omega_c|$.

The ground state properties of the binary condensate are not changed for negative values of Ω, which in this case it is given by the $|-\rangle$ dressed state. This configuration is energetically identical to the case of positive Ω and a $|+\rangle$ state as we have seen in Equation 2.39. Consequently the extension to negative values of Ω is does not have physical consequences in terms of the ground state of the

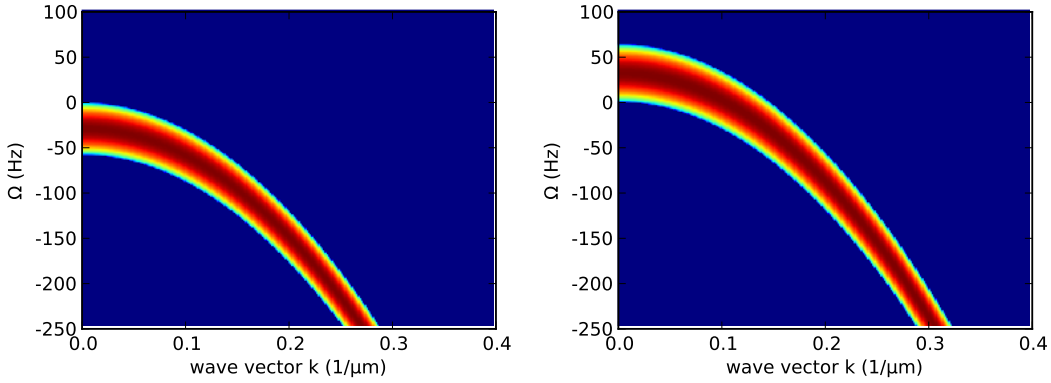

Figure 2.11.: Unstable modes versus linear coupling strength for miscible (left) and immiscible (right) scattering parameters. (left) The miscible system becomes unstable for $\Omega < 0$ and a decreasing Ω shifts the region of unstable modes (shaded region) towards larger wave vectors with a square root behavior. The width of the instability region at fixed k is constant and given by $|\Omega_c|$. (right) For immiscible parameters, the characteristics of the instability region are the same as for the miscible case but shifted by Ω_c such that the system becomes stable for $\Omega > \Omega_c$.

system as all of its properties remain the same under the transformation $\Omega \to -\Omega$ and $|+\rangle \to |-\rangle$. In other words the ground state of the system always has a relative phase of $\varphi = 0$ between atomic states and the linear coupling. If the phase of the linear coupling is changed by π this is 'compensated' by a phase flip in one of the components.

2.5.1. Phase and stability diagrams and summary

The properties of homogeneous two-component Bose-Einstein condensates in the presence of a linear coupling field can be summarized in phase diagrams for the ground state and the modulational stability of an equal superposition of the components. These diagrams are shown in Figure 2.12.

The system can be either miscible or immiscible, which manifests itself in the overlap of the atomic clouds in the ground state. The overlap is maximal for the miscible system and minimized in the immiscible case. The notion of negative coupling strengths does not affect the ground states, which are equivalent for positive and negative values of Ω as indicated by the symmetry with respect to $\Omega = 0$ in the phase diagram (left panel of Figure 2.12).

The stability of the system is determined from the linear response of an equal superposition of the two components to spin fluctuations. An excitation mode with an imaginary eigenenergy grows exponentially and is considered unstable. Negative coupling strengths can be realized by changing the relative phase of the linear coupling and the atoms by π. As stability depends on the preparation of the experimental state negative coupling strengths lead to new physical effects. In particular a miscible system can become unstable as shown in the right panel of Figure 2.12. The scaling of the relevant length scales of unstable modes (e.g. the smallest unstable wavelength) is continued smoothly across $\Omega = 0$.

In this chapter we have introduced the theoretical description of linearly coupled and interacting two-component Bose gases in a one-dimensional geometry. We have seen that a linear coupling field can tune a system with immiscible scattering parameters to miscibility, i.e. the ground state wave functions of the two components overlap and their excitation spectrum does not have any unstable

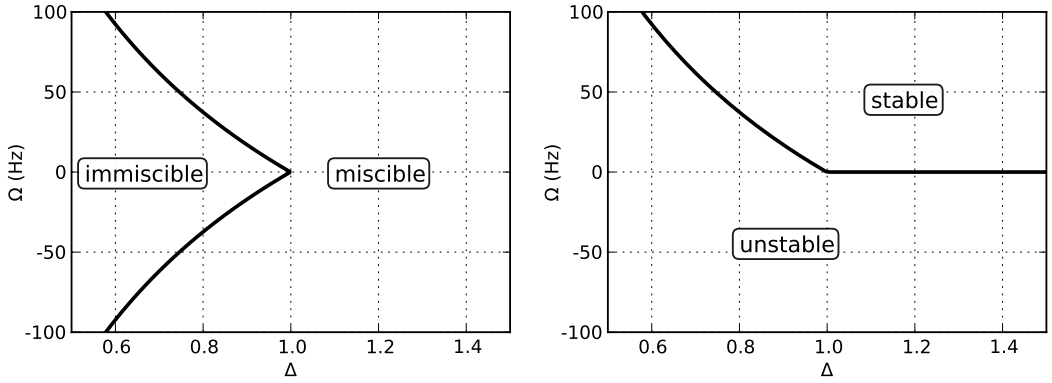

Figure 2.12.: Phase diagram summarizing the ground state (left) and stability properties of the system (right) as a function of Δ and Ω. (left) The ground state of the system becomes miscible as $|\Omega|$ exceeds the critical value Ω_c (solid line). It is symmetric with respect to $\Omega = 0$ as the ground state configurations for positive and negative coupling strengths are equivalent (see text). (right) For positive Ω a system with a miscible ground state is also stable against spin fluctuations. However, the system can be prepared in an excited state corresponding to negative coupling strengths, which is always unstable.

modes. The relevant energy scale is the energy contained in a domain wall ng_s. This parameter determines all relevant length and time scales of the system, e.g. the critical coupling strength, the spin healing length and the wavelengths and growth rates of the unstable modes. In the following chapter we will introduce the experimental realization of such a system.

3. Experimental system and analysis methods

After having discussed the theoretical description of the ground state and excitation properties of linearly coupled binary Bose-Einstein condensates, we will now focus on the experimental implementation of such a system. We will introduce the experimental apparatus and methods for the generation and detection of ultracold atomic clouds. The methods for the analysis of the experimental data will be presented by discussing the free, i.e. uncoupled, evolution of an equal superposition of two interacting condensates. The dynamics of the density distributions of the two components depends on their relative interaction strengths. By employing a Feshbach resonance, we will discuss both the regimes of potential and phase separation [43]. Modulational instabilities dominate the dynamics in the latter case and lead to regions where only one component is present surrounded by domains of the other component. As these patterns correspond to modulations in the difference of the density profiles we will refer to them as spin domains. A similar experiment employing comparable analysis methods was reported recently by the Spielman group [60].

3.1. Experimental system

In order to experimentally explore the interplay of interactions, linear coupling and spatial degrees of freedom, we employ Bose-Einstein condensates of ^{87}Rb. They are well isolated from the environment and can be created with good reproducibility making them an ideal model system for such studies.

The experimental apparatus and the details of the generation of the condensates and their detection have been described in previous theses [61, 62, 63, 32]. Here, we will briefly summarize the aspects of the experimental system and sequence that are relevant for the experiments presented in this thesis. Experimental challenges for the creation of one-dimensional condensates in optical dipole traps will be outlined. The numerical values of the relevant experimental parameters are summarized in Appendix A.

The ^{87}Rb atoms are initially confined in a magneto-optical trap and then transferred to a magnetic quadrupole trap. Subsequent evaporative cooling using a time orbiting potential (TOP) creates an atomic cloud of nearly 10^6 atoms close to degeneracy in the $|F = 1, m_F = -1\rangle$ state of the $5S_{1/2}$ ground state manifold. After a transfer to an optical dipole trap, degeneracy is reached with further evaporative cooling by lowering the intensity of one of the trap beams. The trap lasers with a wavelength of 1064 nm are far red detuned from the atomic resonances at $\lambda_{D2} = 780\,\text{nm}$ and $\lambda_{D1} = 795\,\text{nm}$. The details of the employed optical dipole trap depend on the performed experiments and will be discussed below. After condensation, a magnetic bias field for tuning of the inter-species scattering length is ramped to its target value and the actual experiment is conducted by a sequence of microwave and radio frequency pulses. Finally, the atomic clouds are imaged destructively by high-intensity absorption imaging [64, 26]. The duration of one experimental cycle is about 40 s.

3.1.1. Optical dipole traps

The experiments described in this thesis were performed in two different optical dipole traps. The experimental sequence for the preparation of the atomic cloud depends on the details of the em-

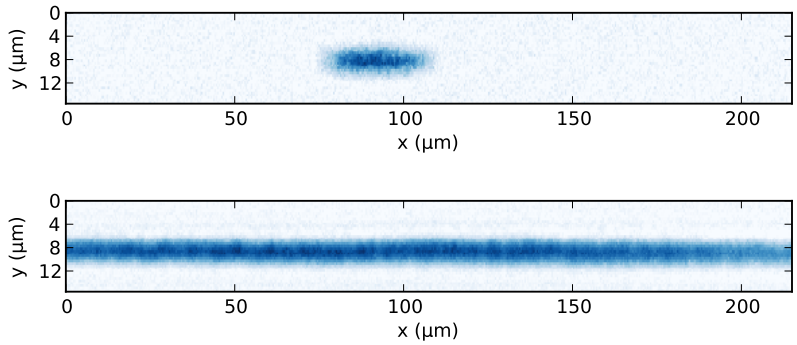

Figure 3.1.: Absorption images of 3000 atoms in the charger (top) and 45000 atoms in the waveguide (bottom). A high atomic column density is encoded in color, while white regions indicate the absence of atomic absorption. The different aspect ratio of the two traps and the increased longitudinal extent of the atoms in the waveguide are clearly visible.

ployed trap such as its aspect ratio and trapping frequencies. We will now describe the specifics of these two traps called 'charger' and 'waveguide'.

Charger

The 'charger' consists of a single laser beam focused down to a waist of about 5 µm [65]. Due to this strong focus, the Rayleigh length is small enough to offer sufficient confinement along the longitudinal direction, such that the cold atomic cloud can be transferred directly from the magnetic trap into the charger. A second 'crossed dipole beam' for additional longitudinal confinement during the preparation of the condensate is not required. The use of a single beam makes the position of the prepared Bose-Einstein condensate very reproducible and spatial excitations such as breathing or sloshing are below the detection limit. The tight confinement leads to fast thermalization rates and the duration of the final evaporation ramp is about 100 ms.

The aspect ratio of the transverse and longitudinal trapping frequencies is $\omega_\perp/\omega_x = 21$ [65]. For the experiments performed in the charger, the longitudinal trap frequency is $\omega_x = 2\pi \times (22 \ldots 24)$ Hz with a transverse confinement of $\omega_\perp = 2\pi \times (460 \ldots 500)$ Hz. The exact values depend on the specific settings for each experiment and will be given in the corresponding section. The condensates in the charger consist of a few thousand atoms with a negligible thermal fraction. A typical image of a condensate in the charger is shown in Figure 3.1.

While the preparation of Bose-Einstein condensates in the charger is very reliable and robust, the small aspect ratio leads to a longitudinal size < 30 µm of the atomic cloud. Thus, the inhomogeneous atomic cloud cannot be described as locally uniform and the deviations from the homogeneous theory are significant as discussed in subsection 2.4.4.

Furthermore, the typical size of spin patterns created by spatial demixing dynamics is in the range of 5 to 20 µm, which is not much smaller than the extent of the atomic cloud. Boundary effects will dominate the position and size of the spin domains and the low statistics due to the occurrence of only few domains in a single shot limits the accuracy of the determination of their size. These limitations can be relaxed by employing a different trap, the 'waveguide'.

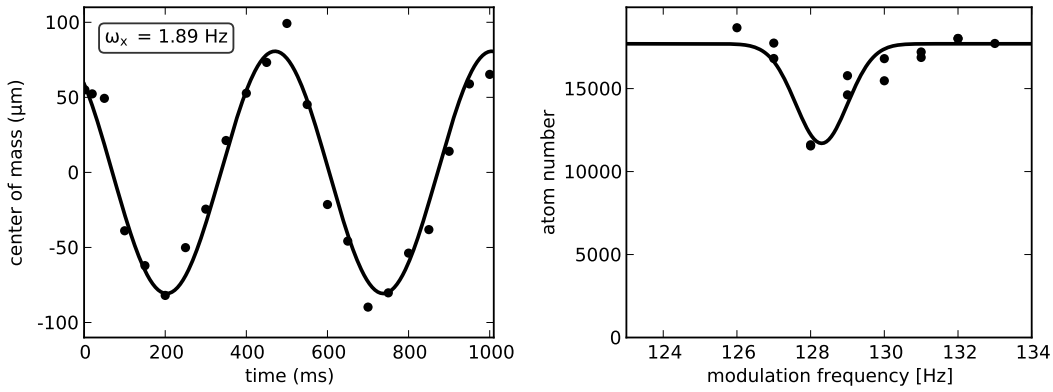

Figure 3.2.: Trap frequency measurements in the waveguide. The longitudinal trap frequency ω_x is extracted from a sinusoidal fit to the center of mass motion of an atomic cloud that was initially displaced from the trap center (left). The transverse frequency $\omega_\perp$ is determined by measuring atom loss due to parametric heating when modulating the intensity of the trap laser (right).

Waveguide

Like the charger, the waveguide consists of a single focused beam. However, its waist is larger[1] resulting in smaller trapping frequencies and a larger aspect ratio $\omega_\perp/\omega_x > 60$. In the experiments described in this thesis, the trap frequencies were measured to be $\omega_x = 2\pi \times 1.9\,\mathrm{Hz}$ and $\omega_\perp = 2\pi \times 128\,\mathrm{Hz}$. The longitudinal trap frequency was deduced from the center of mass motion of the atomic cloud which was initially displaced from the trap center. The transverse confinement was measured by atom loss due to parametric heating by an intensity modulation of the trap laser. The experimental data is shown in Figure 3.2. The shallow longitudinal confinement leads to an atomic cloud with a length $> 250\,\mu\mathrm{m}$, which is significantly larger than the typical spin patterns due to demixing. The field of view of our camera is about $215\,\mu\mathrm{m}$ wide, such that only a part of the atomic cloud can be detected as shown in the lower panel of Figure 3.1.

The downside of the shallow longitudinal confinement is an increased sensitivity to spatial excitations. Thus, the preparation of the atomic cloud in the waveguide is more complex than for the charger. In particular, the mode overlap with the magnetic trap is strongly reduced and the longitudinal confinement is not strong enough to directly transfer the atoms from the magnetic trap into the waveguide. Thus, an additional crossed dipole trap called 'Xdt' has to be used for the transfer from the magnetic trap into the optical traps, as well as for the evaporation where high densities are required for fast thermalization. Only after the evaporation ramp (where the intensity of the waveguide is linearly reduced), the Xdt can be switched off. As the longitudinal trap frequency of the waveguide is much smaller than the additional confinement by the Xdt and has a small absolute value, the power of the Xdt has to be reduced slowly in order to minimize spatial excitations. By employing a ramp consisting of three segments with decreasing slopes we can limit the duration of this process to about 1 second. Due to the low intensity of the Xdt beam in the last segment of the ramp small power fluctuations can excite breathing modes of the atomic cloud.

Furthermore, external forces can lead to a significant displacement of the atomic cloud in the longitudinal direction. Magnetic field gradients can cause such forces, because the atoms are in a magnetically sensitive state. For example, the displacement of the trap minimum due to the first

[1] A waist of 30 µm was measured in [65]. However, the fiber outcoupler was changed since.

order Zeeman shift and a magnetic field gradient of $dB/dx = 50\,\mu\text{G}/100\,\mu\text{m}$ is

$$\Delta x = \frac{m_F \mu dB/dx}{m\omega_x^2} = 11\,\mu\text{m}$$

with the magnetic moment $\mu = 700\,\text{kHz/G}$. Thus, the transfer of atoms from the initial state $|F = 1, m_F = -1\rangle$ to the state required for experiments employing the Feshbach resonance, $|F = 1, m_F = 1\rangle$, can initiate significant spatial oscillation dynamics in the presence of magnetic field gradients. In order to minimize such effects, the field gradient was canceled by positioning external permanent magnets. In addition, the Feshbach field is ramped up slowly on the timescale of 1 second in order to minimize spatial dynamics caused by a changing field gradient during the ramp-up.

In summary, the waveguide allows to prepare an elongated atomic cloud that is well suited for analyzing the formation of spin domains in one dimension. However, the increased sensitivity to external perturbations such as magnetic field gradients or power fluctuations of the trap beams leads to larger shot-to-shot fluctuations on the position of the condensate and requires a longer and more complex preparation sequence.

Dimensionality

The cigar-shaped atomic clouds trapped in the charger or the waveguide are not strictly one-dimensional, as the chemical potential is not smaller than the transverse trapping frequency. For example, the chemical potential for commonly employed atom numbers in the waveguide is $\mu \approx 300\,\text{Hz}$, which is larger than the transverse trapping frequency $\omega_\perp = 2\pi \times 128\,\text{Hz}$. The system is better described as quasi-one-dimensional. subsection B.1.1 contains more information about this dimensionality regime and its theoretical treatment.[2]

However, the spin degree of freedom, i.e. the difference density, can treated as one-dimensional. The smallest possible structure size in the spin is given by the spin healing length ξ_s and the smallest unstable wavelength due to modulational instability is $\lambda_c = \sqrt{2}\pi\xi_s$ as discussed in chapter 2. The full width at half maximum transverse extent of the atomic cloud in the trap is 1.1 µm in the charger and 2.0 µm in the waveguide. The smallest spin healing length we can produce is $\xi_s = 1.3\,\mu\text{m}$ close to the Feshbach resonance in the center of the trap, which is on the same order as the transverse size of the cloud. Thus, transverse spin excitations are strongly suppressed and cannot be observed in our experiments. The spin dynamics is restricted to one spatial dimension.

3.1.2. Linear coupling

During the condensation process, the atoms are in the $|F = 1, m_F = -1\rangle$ state. Using microwave and radio frequency radiation, we can transfer atoms to any state within the $5S_{1/2}$ manifold, which is sketched in Figure 3.3. The frequency of the microwave field is given by the hyperfine splitting of 6.834 GHz [67]. The required radio frequency is determined by the Zeeman splitting, whose linear contribution is $\mu = 700\,\text{kHz/G}$ leading to a few MHz at magnetic fields of a few Gauss. Typical single-photon Rabi frequencies for microwave transitions are 10 kHz and for radio frequency transitions 20 kHz, respectively. Two-photon transitions are detuned by 200 kHz from the intermediate level, such that typical two-photon Rabi frequencies are 500 Hz. These coupling strengths are large enough, such that the non-linear effects of interactions can be ignored during $\pi/2$ or π pulses which transfer atoms between different sublevels.

[2] In the language of the one-dimensional systems, our experimental parameters correspond to dimensionless interaction and temperature parameters of $\gamma \approx 6 \times 10^{-5}$ and $t \approx 2.6 \times 10^3$. This corresponds to being at the cross-over from thermal to the quantum quasicondensate regime. A phase diagram and can be found in [66].

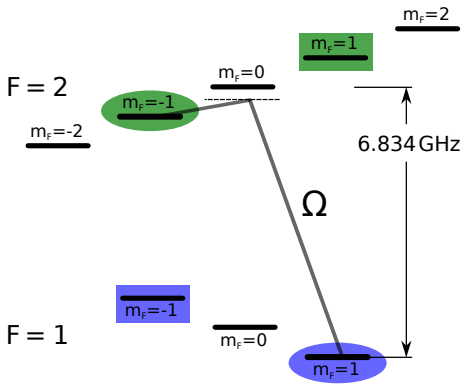

Figure 3.3.: Level scheme of the $5S_{1/2}$ ground state of ^{87}Rb. The pair of states featuring the Feshbach resonance are marked by ellipses, the ones with a 'magic field' by rectangles. A linear coupling via two-photon microwave - radio frequency radiation is sketched by gray lines for the example of the Feshbach states.

As the radio frequency signal is generated using an arbitrary waveform generator[3], all its characteristics such as amplitude, phase and frequency can be controlled and changed arbitrarily on time scales $< 1\,\mu s$. This high level of control makes the linear coupling an ideal control parameter for phase transitions as will be discussed in the following chapters.

Resonant linear coupling is critical for the experiments described in this thesis. The correct frequencies for a given magnetic field can be calculated using the Breit-Rabi formula. However, as we employ a two-photon transition the resonance condition is modified by the ac Zeeman shift (also referred to as 'light shift') due to the coupling radiation itself. Both the microwave and the radio frequency radiation are detuned from the intermediate level by about 10-20 times the coupling strength. The ac Zeeman effect of each field shifts the relative splitting of the involved atomic states (see [68] for details). The combined effect of the microwave and the radio frequency field has to be compensated by adjusting their frequencies. For our parameters this effect shifts the resonance by about $-80\,Hz$ to $-120\,Hz$. As the exact value of the light shift depends on the amplitude of the coupling fields it has to be adjusted when changing the coupling strength. The values of the individual light shifts stemming from the microwave or radio frequency field can be measured by a Ramsey sequence where the corresponding coupling field is present during the interrogation time. For the power settings used during the initial $\pi/2$-pulses light shifts of $-120\,Hz$ and $+35\,Hz$ were measured for the microwave and the radio frequency field, respectively.

Another effect that modifies the resonance condition is the mean field shift due to different interaction parameters of the two atomic components. Different intra-species scattering lengths a_{11} and a_{22} cause a difference in the chemical potentials of the two components when an equal superposition of them is prepared. This corresponds to an effective detuning $\delta_{MFS} \propto (g_{11} - g_{22}) \cdot n$ [34, 41]. As this effect depends on the atomic density, it creates a space-dependent detuning when working with harmonically confined and thus inhomogeneous atomic clouds, $\delta_{MFS} = \delta_{MFS}(x)$. The typical amplitude of the mean field shift is $\delta_{MFS} \approx 10\,Hz$ in the center of the atomic cloud for our experimental parameters. The average mean field shift can be compensated by adjusting the frequency of the radio frequency field. However, spatial variations of a few Hertz due to the inhomogeneity of the atomic cloud remain. This effect is negligible for $\Omega \gg \delta_{MFS}$, but can have significant implications if this condition is not fulfilled.

[3] Agilent 33522A

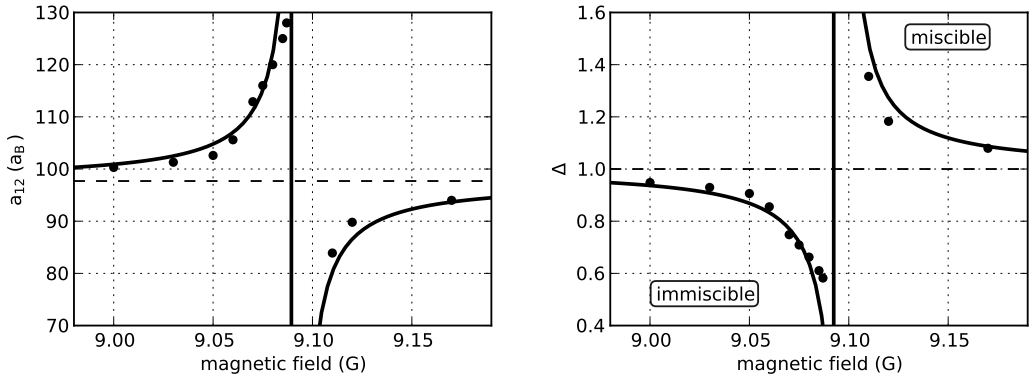

Figure 3.4.: Scattering lengths a_{12} (left) and miscibility parameter Δ (right) around the Feshbach resonance. The experimental data (black circles) was deduced from the frequency of plasma and π oscillations (see subsection 2.2.2) and independently confirmed by the experiments presented in this and the following chapters. The solid lines are taken from [32], the dashed lines correspond to the background value of a_{12}.

3.1.3. Employed atomic states and Feshbach resonance

An interesting pair of states in the ground state manifold of ^{87}Rb is $|1\rangle = |F = 1, m_F = -1\rangle$ and $|2\rangle = |2, 1\rangle$, since their differential Zeeman shift (which is already the quadratic shift) cancels to first order at the 'magic field' $B = 3.23\,\mathrm{G}$ [69]. In this configuration these states are only weakly sensitive to magnetic field fluctuations and very long coherence times have been reported [70, 71]. Similarly, magnetic field gradients act as common-mode forces on atoms in these two states and the differential effects are minimized.

Other interesting states are $|1\rangle = |F = 1, m_F = 1\rangle$ and $|2\rangle = |2, -1\rangle$, because they feature a narrow Feshbach resonance at $B = 9.09\,\mathrm{G}$ [72, 73, 74], which allows to change the inter-species scattering length a_{12} of these states by up to 30%. The background scattering lengths of ^{87}Rb are all equal within 5% and the system is close to the miscibility threshold $\Delta = 1$ far from resonance (see section 2.3). Thus we can tune the system both into the miscible and the immiscible regime by employing this Feshbach resonance as shown in Figure 3.4.

These two pairs of states will be used for the experiments described in this thesis. They are illustrated in Figure 3.3.

Magnetic field stabilization

Near the Feshbach resonance the differential shift of the involved atomic states due to the quadratic component of the Zeeman shift is $10\,\mathrm{Hz/mG}$, such that a stable magnetic field is required to increase the coherence time and to keep the two-photon coupling resonant. For example, when dressing the atoms with a coupling strength of a few ten Hertz, the detuning has to be kept below a few Hertz, which requires a magnetic field stability well below 1 mG.

In addition, the Feshbach resonance has a small width of a few milligauss and our measurements require interaction parameters that are constant over the duration of one experiment and shot-to-shot reproducible. For example, the relevant interaction parameter g_s (equivalent to the nonlinearity χ in the notation of the Josephson junction) increases by 50% when changing the magnetic field by 10 mG from 9.07 G to 9.08 G. Thus a magnetic field variation of 1 mG changes the interaction parameter by more than 5% when working close to resonance.

In order to fulfill these stability requirements we synchronize the experimental cycle to the 50 Hz power line and additionally employ an active field stabilization. A feedback loop reduces the shot-to-shot variations due to low frequency magnetic field fluctuations below 50 μG. A feed forward suppresses the amplitude of the remaining 50 Hz power line component from 200 μG [32, 39] below the shot-to-shot fluctuations. The magnetic field is generated by large coils with a size of 1 m × 1 m in Helmholtz configuration in order to ensure field homogeneity.

3.1.4. Detection of the atomic cloud

The observation of spatial patterns requires in-situ imaging of the atomic cloud. The two components are subsequently detected in the trap by high-intensity absorption imaging [64, 26] with a temporal delay between the pictures of 780 μs. The images are followed by a reference picture not containing any atomic signal in order to eliminate fringe noise. The imaging resolution of our experimental setup is 1.1 μm according to the Rayleigh criterion [75].

In previous experiments, the atomic populations of the involved states was 'frozen' by transferring them to the $F = 1$ manifold where losses are negligible. The magnetic field was subsequently reduced and the image was taken at a low magnetic field of a few hundred milligauss for optimized atom number resolution [26]. As the spatial spin pattern critically depends on the exact interaction parameters and adjusts to external changes within a few milliseconds, the density distribution cannot be frozen for these experiments. Instead the absorption images are taken at the magnetic field close to the Feshbach resonance at 9.09 G where the experiment was conducted. The Zeeman splitting of different m_F levels is on the same order as the line width of the employed D2 transition, which requires adjustments to the imaging calibration. The necessary steps are summarized in Appendix C.

3.2. Free evolution experiments and their analysis

In this section, we will discuss the experimental results on the free evolution of an equal superposition of the two components. By 'free', we mean the absence of any linear coupling, such that the dynamics is governed by the atomic interactions. We will begin with experiments performed in the charger at the 'magic field' with the background scattering lengths of ^{87}Rb. Afterwards we will focus on similar experiments in the waveguide but close to the Feshbach resonance, where the dynamics is dominated by modulational instabilities. Along the way, we will introduce the analysis methods for the interpretation of the experimental results that will be used throughout this thesis.

3.2.1. Free evolution far from the Feshbach resonance in the charger

We will first consider the time evolution of a superposition of atomic clouds far from the Feshbach resonance, i.e. with the background interaction parameters of ^{87}Rb. For maximum stability, we work at the 'magic' field of $B = 3.23$ G using the states $|1\rangle = |F = 1, m_F = -1\rangle$ and $|2\rangle = |2, 1\rangle$. These measurements were conducted in the charger with a longitudinal trap frequency of $\omega_x = 2\pi \times 23.4$ Hz and a transverse confinement of $\omega_x = 2\pi \times 490$ Hz. A condensate of about 5600 atoms in state $|1\rangle$ is prepared, an equal superposition of $|1\rangle$ and $|2\rangle$ is created by a two-photon $\pi/2$-pulse and the subsequent dynamics is observed. This experiment is similar to the first measurements on component separation in ^{87}Rb [76].

The background interaction parameters of ^{87}Rb are close to the miscibility threshold, $\Delta \approx 1$. Commonly used scattering lengths yield $\Delta = 1.0001$ [77], 0.9966 [78] and 0.9980 ± 0.0008 [79], so the literature is not definite about whether the system is miscible or immiscible (see Appendix A

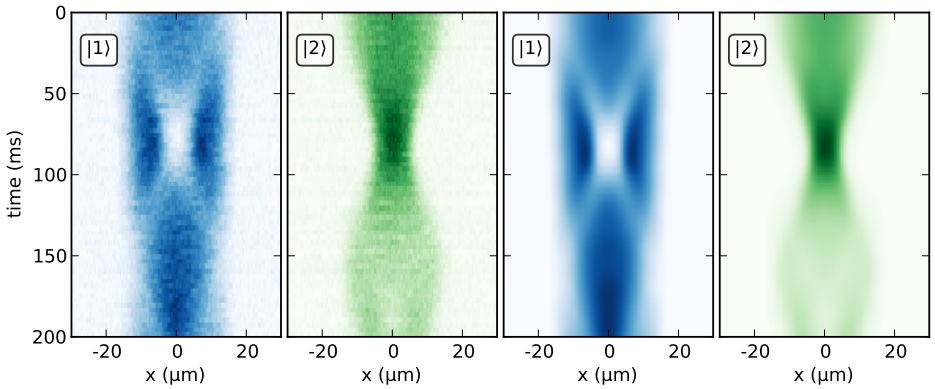

Figure 3.5.: Time evolution of an equal superposition of two condensates in the charger at the background scattering lengths. The left panels show the experimentally obtained density timetrace in the two components, while the corresponding numerical simulations are shown on the right. Component $|1\rangle$ is pushed to the edges of the trap due to its larger scattering length $a_{11} > a_{22}$. This dynamics is referred to as potential separation (see text). The excellent agreement with numerics demonstrates the experimental stability and reproducibility when working in the charger and at the 'magic field'.

for the values of the scattering lengths). Independent of the sign of $\Delta - 1$, the dynamics following the $\pi/2$-pulse will not be governed by unstable modes. If $\Delta > 1$, there are no unstable modes and considering $\Delta = 0.99 < 1$, the fastest predicted growth rate of 1 Hz is too slow to have an influence on the timescale of our measurements. Furthermore, the corresponding unstable mode has a wavelength exceeding 50 μm and cannot grow as it is larger than the size of our system. Thus, the dynamics is purely deterministic and reproducible.

The observed time evolution of the atomic density profiles is shown in Figure 3.5. Atoms in state $|1\rangle$ are pushed to the edges of the trap while component $|2\rangle$ occupies the trap center. After about 80 ms this dynamics is reversed and the density profiles oscillate back towards the initial configuration. The agreement with numerical simulations[4] is excellent. The spatial dynamics is caused by the asymmetry in the intra-species scattering lengths $a_{11} > a_{22}$, which favors lower densities of component $|1\rangle$. In miscible systems such dynamics occurs only if the translational symmetry is broken by the presence of an external trapping potential. No redistribution of the atomic density is expected in a homogeneous system as discussed in subsection 2.3.3. For this reason, the observed time evolution is referred to as potential separation [43].

The measurements can be understood as the evolution of each component in an effective potential given by the external trapping potential and the repulsive mean field interactions $V_{\mathrm{eff,\,i}}(x) = V(x) + g_{ii}|\psi_i(x)|^2 + g_{ij}|\psi_j(x)|^2$. Before the initial $\pi/2$-pulse all atoms are in state $|1\rangle$ and the density distribution is given by the corresponding ground state. The fast coupling pulse creates an equal superposition of the two states, each having the same spatial density profile as the initial state before the pulse. As this configuration is not the ground state of the two-component system, the mean field potentials $V_{\mathrm{eff,\,i}}(x)$ will initiate a redistribution of the atomic clouds. This effective potential is not a static one and changes with the spatial density profiles of the atoms, but it provides an intuitive approach for understanding the resulting dynamics.

The redistribution of the atomic clouds reduces the total potential energy of the system consisting of the external trapping potential and the mean field interaction energies. The kinetic energy

[4] A summary of the employed methods can be found in Appendix B, while the atomic and experimental parameters are given in Appendix A.

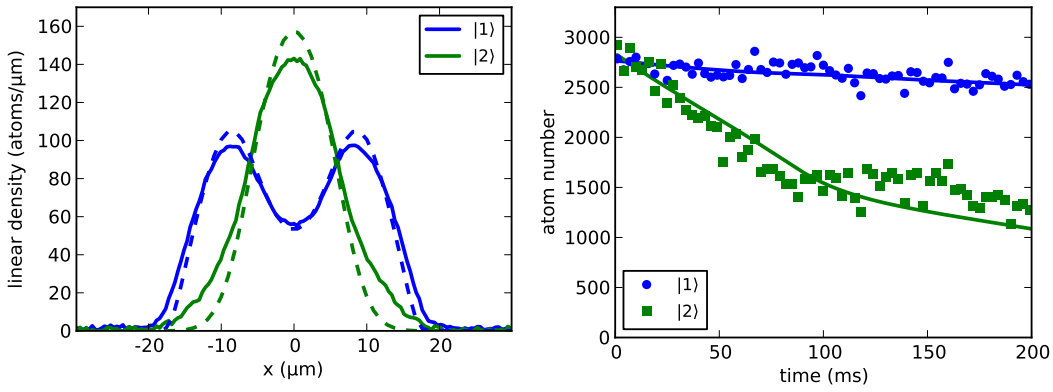

Figure 3.6.: Left panel: Comparison of the temporal mean of the measured density timetrace averaged over $0 \leq t \leq 140\,\mathrm{ms}$ (solid lines) with the numerically computed ground state (dashed lines). The mean atom number in each component in the chosen time range was used for the simulation. Right panel: Time evolution of the atom number in each component. Loss in state $|2\rangle$ is increased due to spin relaxation loss in agreement with the simulations (solid lines).

is increased by the dynamics. Similar to a classical particle, which is initially displaced from the minimum of a harmonic potential, the density configuration will move towards the potential minimum (representing the ground state) and pass through this point due to the accumulated kinetic energy. Assuming symmetric evolution around the energy minimum, we can estimate the ground state configuration of each component by calculating the temporal mean of their density profiles. The density profiles averaged over the first oscillation period of the time evolution are compared to the numerically computed ground state in the left panel of Figure 3.6.

One possible dissipation process for the oscillatory dynamics is atom loss. While loss in component $|1\rangle$ is negligible, spin relaxation loss limits the lifetime of component $|2\rangle$. The right panel of Figure 3.6 compares the measured loss with the numerical simulations employing the literature loss coefficients (see Appendix A).

3.2.2. Formation of spin domains near the Feshbach resonance in the waveguide

We have seen in the previous section that the dynamics in the charger far from the Feshbach resonance is governed by potential separation, while unstable excitation modes do not play a role. Only close to the Feshbach resonance, instabilities can be observed in the charger, but they are strongly influenced by the finite longitudinal size of the cloud and the inhomogeneity due to the external trapping potential.

The waveguide is better suited for the analysis of unstable modes. The time scale for potential separation depends on the chemical potential μ and the longitudinal trapping frequency ω_x. In the waveguide μ is smaller by a factor of 2 and ω_x by a factor 10 compared the charger, such that potential separation does not play a role on the time scale of our experiments. In addition, the increased size of the atomic cloud shifts the infrared cutoff in the excitation spectrum to larger wavelengths. The increased homogeneity leads to comparable experimental conditions over a large spatial range, such that the analytic predictions for homogeneous systems can be applied.[5]

[5]Validity criteria for the description of excitations in an elongated atomic cloud by a homogeneous theory have been discussed in [33] in the context of sound propagation in Bose-Einstein condensates [80, 81].

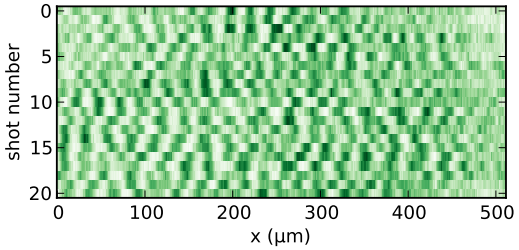

Figure 3.7.: Randomness of domain structures generated by phase separation due to unstable modes. The $F = 2$ density profiles of subsequent realizations under the same experimental conditions ($B = 9.08\,\mathrm{G}$, image taken after $t = 32\,\mathrm{ms}$) are shown in false color. The density pattern does not systematically repeat itself.

We can examine the unstable region of the Bogoliubov spectrum in the waveguide by preparing an equal superposition of the two components and subsequently analyzing the emerging spatial pattern of spin domains, which will be dominated by the unstable modes of the excitation spectrum. As the resulting spatial pattern is based on instability, small density variations in the prepared superposition act as a seed causing the growth of different modes. Due to the destructive detection method we cannot observe the dynamics in a single experimental realization and a new independent condensate has to be prepared for each absorption image. Thus, the position of the domains will not be deterministic but randomly vary from shot to shot. This randomness is illustrated in Figure 3.7.

For the experiments in the waveguide near the Feshbach resonance, the connection to the ground state cannot be drawn by the temporal mean of the density profile as it was the case for the potential separation in the charger. Thus, different analysis methods have to be applied, which will be introduced in the following section.

3.2.3. Analysis methods: Counting, Fourier spectra and correlations

The characteristic signature of spatial spin patterns is the time evolution of the typical size of the domains and their modulation depth. This section evaluates a few methods for the extraction of this data from the experimental images. One common requirement for all methods is that they must not rely on a reproducible position of the domains due to their random locations.

The input signal for all these methods is the experimental spin profile. It is calculated from the longitudinal density profile $n_i(x)$ of each component, which is extracted by summing over the rows around the corresponding absorption signal for each pixel column. The spin profile $J_z(x)$ is defined as the normalized difference profile, $J_z(x) = \frac{n_2(x)-n_1(x)}{n_1(x)+n_2(x)}$. As the extent of the atomic cloud is larger than the field of view of the camera, no extra care has to be taken to exclude boundary region with increased noise due to a vanishing atom signal. However, some experiments critically depend on a homogeneous density distribution. In this case, only a part of the spin profile around the center of the atomic cloud is used for further analysis. The requirements and the details of this spatial post-selection will be explained in the description of the respective measurements.

Counting domains

One analysis method proposed and employed in [18] is counting the number of domains in a given spatial region and deducing the 'domain density' i.e. the number of domains per unit length. For example, domain boundaries can be extracted from the spin profile as zero-crossings. Alternatively, domain centers can be localized by identifying local maxima and minima. These approaches require

the use of detection thresholds in order to distinguish the domain signal from detection noise. As atoms are lost during the time evolution, the signal-to-noise ratio is reduced and the threshold criteria change. The required choice of a threshold makes this method unreliable for small modulation depths of the domains.

Fourier analysis

A more robust analysis method is employing the Fourier spectrum of the spin profile, where the most dominant oscillatory mode, i.e. the typical domain size, is directly given by the highest peak in the spectrum. In order to have sufficient spatial resolution, the size of the domains must be significantly smaller than the spatial range where the spin profile is evaluated. The amplitude of the detected peak is directly proportional to the modulation depth of the spin patterns.

Autocorrelation function

Similarly, the autocorrelation function of the spin profile can be calculated. As every point in the correlation function is averaged over the whole profile, this intrinsic averaging suppresses technical noise.

The autocorrelation function is connected to the power spectrum of the spin profile via a Fourier transformation as stated by the convolution theorem. Thus, its information content is equivalent to the previously mentioned Fourier spectra. For periodic structures, a peak in the Fourier spectrum can be found more reliably than the oscillation period of the correlation function. Consequently, the Fourier method is preferred in this case.

However, the autocorrelation method additionally allows the analysis of spatial spin correlations even if the system is not prepared in the immiscible regime, where the growth of unstable modes leads to periodic spin structures. In the miscible regime, the autocorrelation function of the fluctuations on top of the spin profile is predicted to decay to zero with a power law or exponentially depending on the system parameters and the details of the measurement [82]. The length scale of the decay depends on the distance to the critical point and can be associated with a correlation length. Measurements in this regime will be discussed in subsection 5.3.1.

Both the Fourier spectra and the correlation functions do not depend on shot-to-shot variations in the positions of the domains, i.e. phase shifts of the oscillatory structures. Thus they can be averaged over different experimental realizations of the same physical settings (e.g. same magnetic field and evolution time). This averaging increases the signal to noise ratio and yields reliable results also for small modulation depths around 5% even in the presence of detection noise such as photon shot noise.

Post-processing of the spin profile

In many experiments presented in this thesis, we are interested in the linear response of the system to a sudden parameter change. The linear response regime is valid for small perturbations, e.g. periodic structures or correlations on top of the background state. In these measurements, we are analyzing the *spin* profile, such that inhomogeneity effects of the spatial sum density profile are already canceled.

However, both the Fourier and the autocorrelation methods are prone to asymmetries of the spin profile, e.g. to a mean imbalance $z \neq 0$ due to different densities in the two components. Such problems can occur in the experimental data for multiple reasons:

- Imperfect $\pi/2$ preparation pulses, e.g. due to temporal drifts or spatial gradients in the microwave or radio frequency fields

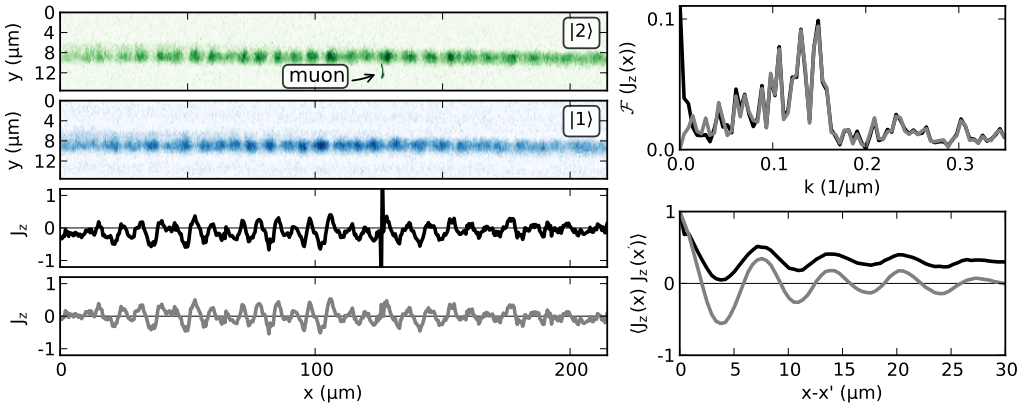

Figure 3.8.: Illustration of the post-processing of the spin profile and its impact on Fourier spectra and correlation functions. From the experimental images (top left), the spin profile is extracted (center left). The effect of spurious muon impacts on the CCD is visible as sharp spikes in the spin profile. The post-processing removes these artefacts and centers the spin profile around zero with the result shown on the bottom left. The Fourier spectra and correlation functions corresponding to the raw (black lines) and corrected (gray lines) spin profiles are shown on the right. The 'muon' causes a kink near the origin in the correlation function. The trend removal reduces low-frequency components in the Fourier spectrum and centers the correlation function around zero.

- Species dependent, asymmetric loss, such as spin relaxation loss in the $F = 2$ component
- Detuning of a linear coupling field
- Different detectivity of the imaging process to the different species, such that a balanced state is detected to be imbalanced (see Appendix C)

In addition the spin profile can have an overall trend across the spatial cloud caused by

- a local detuning of the linear coupling due to the mean field shift, which depends on the spatial density profile
- a gradient in the amplitude of the linear coupling field (see subsection 4.1.1) leading to an inhomogeneous temporal evolution and a local detuning due to the spatial variations of the light shift.

These effects are small, but can dominate the deduced Fourier spectrum or autocorrelation function as illustrated in Figure 3.8. For this reason, the spin profile extracted from the absorption images is post-processed before performing the analysis. This post-processing consists of the following steps:

1. Compensate for known different detectivities of the imaging system (see Appendix C)
2. Remove muons. Impact of particles from cosmic background radiation (which we refer to as 'muons') on the CCD chip cause bright or dark pixels on the absorption images roughly once every 50 shots. In some cases, the position of these pixels is within the picture of the atomic cloud and they affect the integrated density profiles. As these artefacts usually occur only on one of the absorption images of the two components, the muons manifest themselves in the spin profile as single pixels with an unphysical imbalance $z \gg 1$. These pixels are corrected

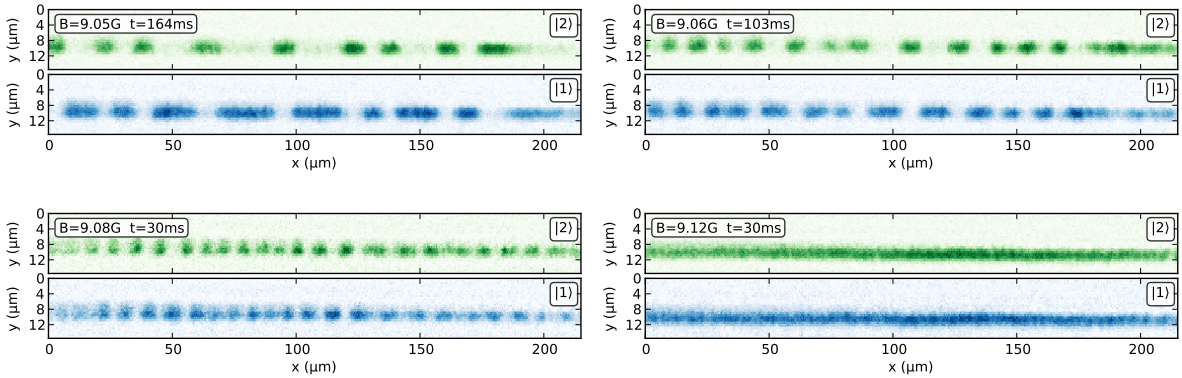

Figure 3.9.: Absorption images of the atomic density profiles at different magnetic fields close to the Feshbach resonance at 9.09 G. As both the growth rate of the domains and the loss rate are increased when approaching the resonance from the immiscible side, the images were taken after different evolution times as indicated in the graphs. The typical domain size decreases when approaching the resonance. The reduced atom number in state $|2\rangle$ due to spin relaxation loss causes an asymmetry in the domain sizes of the two components. This effect becomes less important when approaching the resonance as symmetric Feshbach loss dominates. No phase separation occurs on the miscible side of the resonance (bottom right panel).

by replacing them with the average imbalance of their neighboring pixels. Less than 1% of the shots are affected.

3. (optional) Remove an overall trend in the spin profile. In this step, the spin profile is smoothed by a Gaussian filter. The width of the Gaussian has a typical value of 80 µm and is thus much larger than the observed domain sizes of 2 to 10 µm. This smoothed profile is subtracted from the original spin profile, such that the small structures and fluctuations are conserved but centered around zero imbalance. This procedure corresponds to a applying a high-pass to the spin profile and is omitted for the analysis of phase separation dynamics near the immiscibility threshold, where the domain size exceeds 10 µm.

4. (optional) Discard the edges of the spin profile in order to neglect regions with a reduced atom density due to the inhomogeneity of the condensate. This ensures comparable experimental parameters over the remaining spin profile. In addition, this measure avoids artificial boundary effects introduced by the previous step.

3.2.4. Mapping out the Feshbach resonance

Using these analysis methods, we can investigate the demixing dynamics of an equal superposition of the two components prepared at various magnetic fields on the immiscible side of the Feshbach resonance. The phase separation is governed by the unstable modes of the Bogoliubov spectrum, which depends on the value of the inter-species scattering length a_{12}. When approaching the Feshbach resonance a_{12} is increased which shifts the most unstable mode towards smaller wavelengths and increases its growth rate. On the miscible side of the Feshbach resonance the overlap of the two atomic clouds remains high and no demixing occurs. This behavior is qualitatively illustrated by exemplary experimental images shown in Figure 3.9.

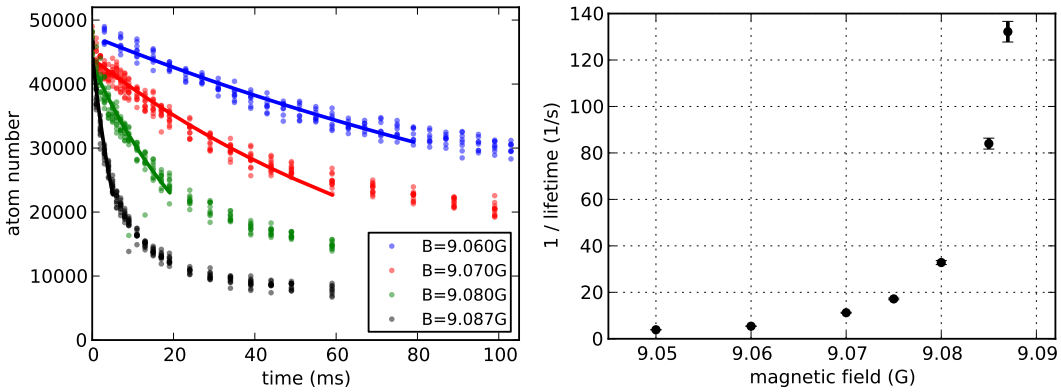

Figure 3.10.: Atom loss at different magnetic fields close to the Feshbach resonance. The lifetime of the atomic cloud strongly depends on the distance to the resonance. Fitting an exponential to the initial evolution of the detected atom numbers (solid lines in left panel) yields the dependence of the lifetime on the magnetic field (right panel).

While the Feshbach resonance offers control of the interaction parameters it has the disadvantage of increased three-body loss as summarized in Figure 3.10. This limits the lifetime of the condensate and thus the range of accessible evolution times. In addition, the temporal change in the linear atom density n affects both the wavelength and the growth rate of the most unstable mode, such that they dynamically change during the time evolution. This complicates the comparison with theoretical predictions. However, it will turn out that using the mean density yields reasonable agreement with experimental observations.

For a quantitative description of the observed dynamics, we recall the results of the Bogoliubov analysis in subsection 2.4.2. As derived in Equation 2.26, the wavelength of the most unstable mode λ_f (i.e. twice the domain size) and the smallest unstable wavelength λ_c are given by

$$\lambda_f = \frac{2\pi}{k_f} = 2\pi\xi_s = \frac{2\pi\hbar}{\sqrt{-mng_s}} \quad \text{and} \quad \lambda_c = \frac{2\pi}{k_c} = \frac{\lambda_f}{\sqrt{2}} \tag{3.1}$$

The most unstable mode grows exponentially with the time constant

$$\tau_f = \frac{2\hbar}{ng_s} \tag{3.2}$$

The inter-species scattering length a_{12}, which is changed in the vicinity of the Feshbach resonance, enters via the interaction parameters g_s (see Equation 2.11).

The Bogoliubov analysis predicts the linear response of an initially homogeneous superposition of the two components. The linear response corresponds to the initial dynamics of the spin profile when the modulation depth of the emerging spin structures is small. At longer evolution times when the modulation depth is a significant fraction of the atom density in each component, the growth will no longer be exponential but saturate. Beyond the linear response the Bogoliubov spectrum is modified by the changing density profiles of the two components. The growth rates may be changed and even previously stable modes may become unstable. These 'secondary' excitation modes have been predicted in the non-equilibrium dynamics after collisions of heavy nuclei [83]. We did not observe any additional unstable modes in our experiments when studying the time evolution of spin profiles beyond the linear response regime.

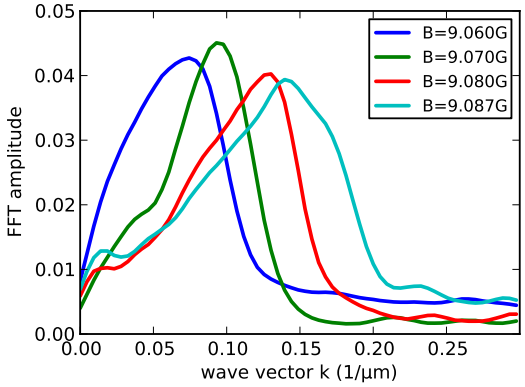

Figure 3.11.: Averaged Fourier spectra at different magnetic fields for a modulation depth of about 30%. The peak of the spectrum is shifted towards smaller wavelengths when approaching the Feshbach resonance indicating the decreasing size of the domains. The displayed spectra are obtained by averaging over about 20 realizations for each value of the magnetic field.

We analyze the observed spin patterns via their Fourier spectra. For each experimental run we calculate the Fourier spectrum of the spin profile and average over about 10 . . . 20 experimental realizations taken under the same conditions, i.e. magnetic field and evolution time. This averaging process increases the signal-to-noise ratio and allows the detection of structures with a small modulation depth, i.e. in the linear response regime. From the peak of this mean spectrum we extract both the amplitude and the wavelength λ_f of the most unstable mode. The domain size is given by half of the wavelength corresponding to the position of the peak in the spectrum. Similarly, we associate the smallest unstable wavelength λ_c with the position of the small-wavelength edge of the spectrum, i.e. the smallest wavelength where the amplitude of the spectrum exceeds a threshold of 0.01. Exemplary Fourier spectra are shown in Figure 3.11.

From these averaged Fourier spectra, we deduce the time evolution of both the modulation depth and the domain size. The amplitude of the spin structures grows exponentially and with an increasing growth rate when approaching the Feshbach resonance. The typical domain size decreases close to resonance and grows in time due to atom loss. These observations are summarized in Figure 3.12.

For a quantitative comparison to the Bogoliubov predictions for a homogeneous system, we average the domain sizes extracted from the mean Fourier spectra over different evolution times with a modulation depth between 5% and 15%. We similarly determine the smallest unstable wavelength λ_c. A comparison of the experimental results to the Bogoliubov predictions for the homogeneous system is given in Figure 3.13.

Magnetic fields between 9.07 G and 9.08 G are suited best for studying phase separation in our experimental configuration. The lifetime of an initial superposition state is 30 . . . 90 ms and thus larger than typical formation times of the spin excitations of 15 . . . 40 ms. On the other hand, the symmetric Feshbach loss is strong enough to dominate over the asymmetric spin relaxation loss affecting only atoms in state $|2\rangle$. This imbalance between the two components causes differently sized domains in the two components and thus complicates the extraction of typical domain sizes as the analysis methods rely on the periodicity of the spin patterns. This effect along with the large domains limits the experimental accuracy when working further away from the Feshbach resonance. Closer to the resonance, both the loss rate and the sensitivity of the interaction parameter to fluctuations and drifts in the magnetic field increase rapidly.

In this chapter we have discussed the experimental system along with its capabilities and limi-

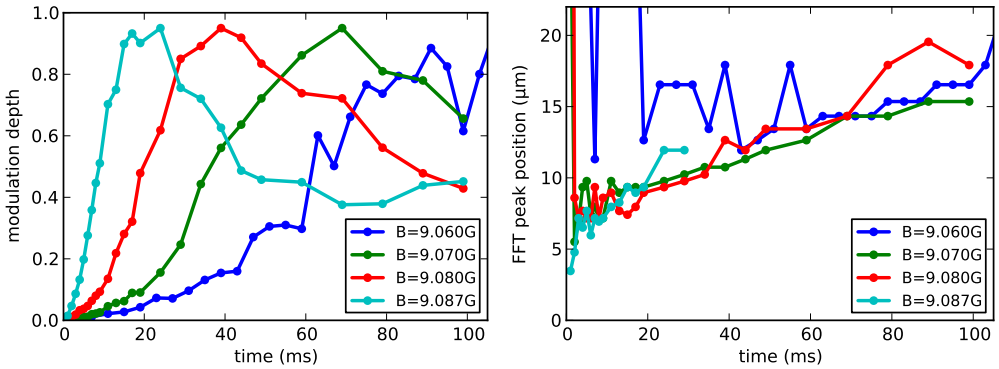

Figure 3.12.: Time evolution of modulation depth (left panel) and domain size (right) corresponding to the peak in the Fourier spectra at different magnetic fields. The growth rate is increased at magnetic fields close to the Feshbach resonance. The reduction in modulation depth following the maximum is due to a lower signal-to-noise ratio as atoms are lost. Atom loss also causes the increase of the domain size in time. The initial noise is due to an amplitude of the spin pattern below the detection threshold.

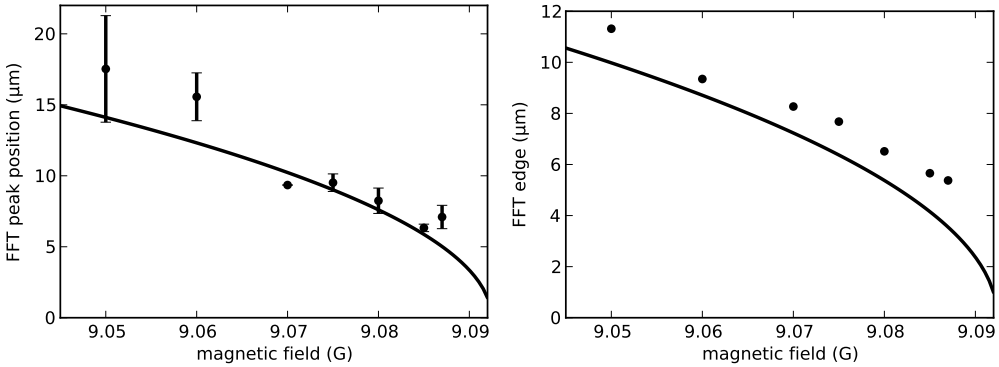

Figure 3.13.: Most unstable mode (left) and smallest-wavelength unstable mode (right) at different magnetic fields. The most unstable mode is extracted from the position of the peak of the Fourier spectrum, while the smallest-wavelength unstable mode is associated with the position of the small-wavelength edge of the spectrum, i.e. the largest wave vector whose Fourier amplitude is larger than a threshold of 0.01. The solid lines are Bogoliubov predictions for k_f and k_c without free parameters based on the values of a_{12} summarized in Figure 3.4 and the initial linear atom density in the center of the atomic cloud. Our experimental findings confirm that the assumption of a homogeneous system is a valid description of our experiment close to the Feshbach resonance. The constant offset in the value of the smallest unstable mode is due to the finite amplitude threshold necessary to exclude detection noise effects.

tations. The Feshbach resonance was presented as a tool to change the miscibility of two atomic clouds. The two dynamical regimes of potential and phase separation were studied experimentally and compared to theoretical predictions. Finally, we have discussed analysis methods for quantifying the relevant properties of the emerging spin patterns. These techniques will be applied throughout the remainder of this thesis.

4. Interacting dressed states

In the previous chapter, we have introduced the experimental system and a Feshbach resonance as a means to tune inter-atomic interactions. Now we will employ this Feshbach resonance to study the interplay between interactions and a linear coupling of two atomic states. In particular, we will analyze the dynamical amplitude reduction of Rabi oscillations in the presence of interactions and its connection to the density distribution of the atomic clouds. The results can be explained in the picture of *interacting* dressed states, which spatially separate similar to the atomic states in the experiments discussed in the previous chapter. Our observations are published in [22], which this chapter is based on while providing more detailed explanations.

4.1. Rabi oscillations in the presence of interactions

A linear coupling field resonantly acting on a two-level system will induce coherent oscillation of the population between the states. These 'Rabi oscillations' were first demonstrated with Bose-Einstein condensates by the group of Eric Cornell in 1998 [84] (see [85] for a review). Figure 4.1 shows the evolution of the imbalance $z = \frac{N_2 - N_1}{N_1 + N_2}$ for Rabi oscillations in our experimental setup using two-photon microwave - radio-frequency radiation. N_1 and N_2 denote the populations of the two atomic levels. The amplitude A of the oscillations, often called visibility, is compatible with 1, the Rabi frequency Ω is about $2\pi \times 520\,\mathrm{Hz}$.

Remembering the theoretical description in subsection 2.2.1 these oscillations are modeled by

$$\begin{aligned} |\psi(t)\rangle &= \cos(\Omega/2\,t)|1\rangle + \sin(\Omega/2\,t)|2\rangle \\ &= \frac{1}{\sqrt{2}}\left(e^{-i\Omega/2\,t}|+\rangle + e^{+i\Omega/2\,t}|-\rangle\right) \end{aligned} \tag{4.1}$$

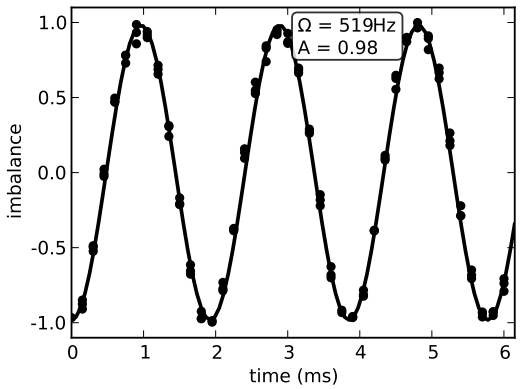

Figure 4.1.: Rabi oscillations driven by two-photon microwave - radio-frequency radiation. The solid line is a sinusoidal fit to the evolution of the measured imbalance (black circles) yielding an oscillation amplitude A compatible with 1 and a corresponding frequency Ω of about $2\pi \times 520\,\mathrm{Hz}$.

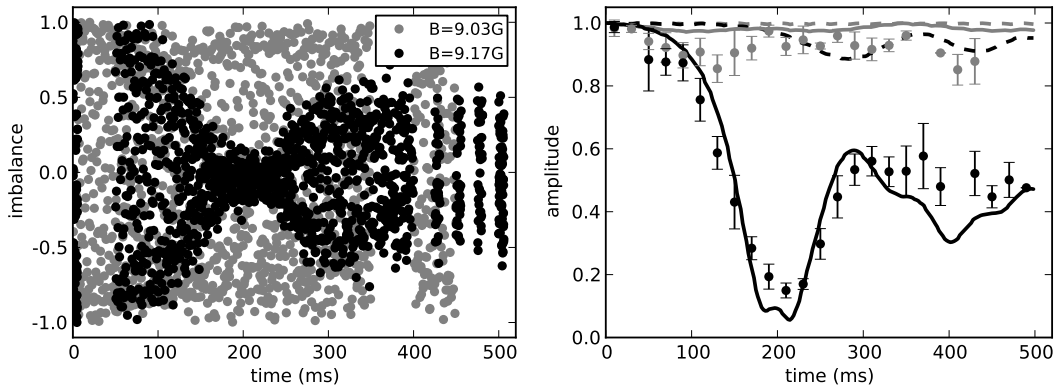

Figure 4.2.: Amplitude of Rabi oscillations in the miscible regime at $B = 9.17\,\mathrm{G}$ (black) and for immiscible parameters (gray, $B = 9.03\,\mathrm{G}$). The raw data in the left panel shows a reduction in the oscillation amplitude in the miscible regime after $\approx 200\,\mathrm{ms}$, which does not occur in the immiscible case. Individual oscillation cycles are not resolved due to the different time scale compared to Figure 4.1. For a quantitative analysis, the envelope of the oscillations is found by extracting the maximum imbalance in each cycle and averaging it over ten subsequent periods (right panel). The error bars correspond to two standard deviations of the mean value. Numerical simulations without free parameters reproduce the results in the immiscible regime, but deviate significantly for miscible parameters (dashed lines). However, after including a gradient in the Rabi frequency the simulations reproduce the observed dynamics well (solid lines).

with the atomic states $|1\rangle$ and $|2\rangle$ and the dressed states $|+\rangle$ and $|-\rangle$ as defined in Equation 2.5. Thus, the oscillation corresponds to the interference of an equal superposition of dressed states. The population of each dressed state is constant and the dynamics occurs only in their relative phase.

4.1.1. Amplitude of long Rabi oscillations

In order to examine the influence of interactions on the oscillation dynamics we measure Rabi oscillations in an elongated Bose-Einstein condensate near the Feshbach resonance. The employed atomic states $|1\rangle = |F = 1, m_F = +1\rangle$ and $|2\rangle = |2, -1\rangle$ are tuned immiscible at a magnetic field of 9.03 G and miscible at 9.17 G. The cloud containing 4400 atoms is confined in the 'charger' (see subsection 3.1.1) with trap frequencies of $\omega_x = 2\pi \times 22.0\,\mathrm{Hz}$ and $\omega_x = 2\pi \times 460\,\mathrm{Hz}$. The system is initially prepared in state $|1\rangle$ before the linear coupling field initiates the oscillation dynamics.

On short time scales of a few oscillation cycles, the Rabi oscillations are not affected by the interactions and no difference can be seen between the miscible and the immiscible case. However, after an evolution time of 200 ms corresponding to roughly 100 cycles, the spatially averaged oscillation amplitude is strongly reduced in the miscible case as shown in Figure 4.2. Here, absorption images of the two atomic clouds reveal a reduced spatial overlap of the two components, i.e. one component occupies the wings of the trap while the other is in the center. Counter-intuitively, this spatial separation occurs only in the *miscible* regime, while the overlap of the atomic clouds remains high in the immiscible case.

We can model our experiments by numerical simulations without free parameters employing the nonpolynomial nonlinear Schrödinger equation (subsection B.1.2). While the agreement in the immiscible regime is good, the simulations do not correctly capture the observed amplitude reduction

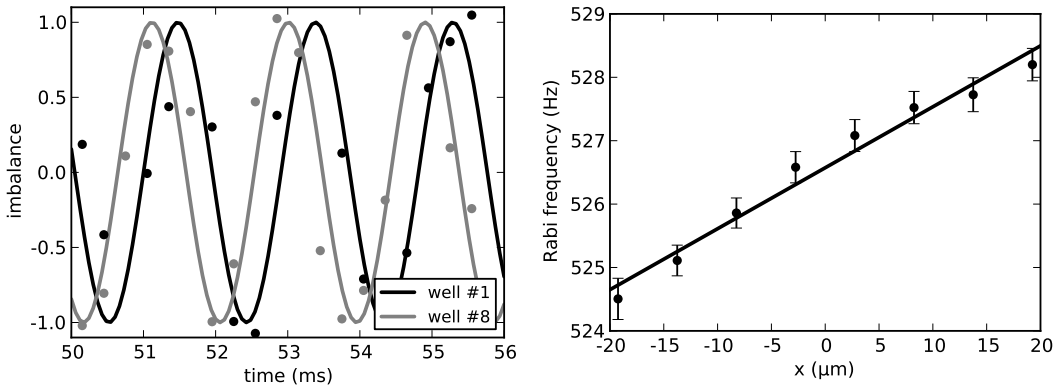

Figure 4.3.: Spatial dependence of the Rabi frequency. The elongated atomic cloud is split into eight independent lattice sites by a standing wave potential. In each well, Rabi oscillations are measured for 130 ms and fitted with a sine. The accumulated phase difference after 50 ms (26 cycles) in the outermost wells due to different oscillation frequencies is illustrated in the left panel. The extracted frequencies (right panel) reveal the spatial variation of the Rabi frequency. Error bars are the two s.d. uncertainty of the fit. The solid line is a linear fit with a slope of $2\pi \times (94 \pm 6)\,\mathrm{mHz}/\mu\mathrm{m}$.

in the miscible case (dashed lines in Figure 4.2). We attribute this deviation to an inhomogeneity in the linear coupling strength, $\Omega = \Omega(x)$.

The spatial dependence of the Rabi frequency can be characterized independently by slicing the atomic cloud into eight separate wells using an optical standing wave potential with a lattice period of 5.5 μm. This technique allows to create independent condensates, each populating a single spatial mode as employed for the experiments in [86, 23, 24, 25]. Thus, the local resonant Rabi frequency can be measured in each well, which reveals a spatial gradient of $\kappa \equiv \nabla\Omega = 2\pi \times (94 \pm 6)\,\mathrm{mHz}/\mu\mathrm{m}$ corresponding to about $2\pi \times 3.8\,\mathrm{Hz}$ or 0.7% across the entire atomic cloud. Coherent oscillations over 130 ms or 70 cycles were fitted in order to obtain this accuracy. These experimental results are summarized in Figure 4.3 and we confirmed that the gradient is independent of the magnetic field. Using Ramsey spectroscopy in each lattice site, we independently checked that the spatial variation in the oscillation frequency does not result from a local detuning $\delta(x)$, e.g. due to a magnetic field gradient, that changes the oscillation frequency via $\Omega_{\mathrm{eff}}(x) = \sqrt{\Omega^2 + \delta(x)^2}$. We determined an upper bound of 0.1% for the contribution of a detuning to the observed gradient in the oscillation frequency.[1] Including this spatial dependence of the linear coupling strength, the numerical simulations (solid lines in Figure 4.2) yield good agreement with the experimental observations.

As we are working in the proximity of the Feshbach resonance atom loss is enhanced. Both at 9.03 G and 9.17 G, the $1/e$-lifetime is 310 ms. Due to the ongoing interconversion of the two components, which is much faster than the loss rate, the spin-relaxation loss of the $F = 2$ component does not cause any asymmetries. These loss effects are included in the numerical simulations as depicted in Figure 4.4.

Note that a similar amplitude reduction of Rabi oscillations in cold atoms was observed in [87, 88]. This effect was attributed to different trapping potentials for the two atomic states as they had different magnetic moments and the magnetic trapping resulted in different gravitational sags. We

[1] Later experiments revealed an inhomogeneous power distribution of the radio frequency radiation to be the cause of this gradient. It can be reduced by a different spatial configuration of the antennas.

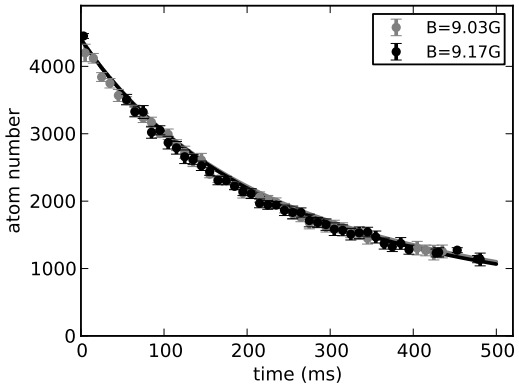

Figure 4.4.: Simulated and measured atom loss. At both magnetic fields, the total atom number decays with a $1/e$-lifetime of 310 ms. The loss due to the Feshbach resonance is included in the simulations (solid lines) as a three body process.

have checked that a similar effect cannot explain our observations. As we employ optical dipole potentials both components experience the same confinement. External forces, e.g. caused by magnetic field gradients acting differently on the two atomic components due to different second order Zeeman shifts could not explain the observations either.

4.2. Interacting dressed states

In order to understand the reduced amplitude of Rabi oscillations on the miscible side of the Feshbach resonance, we describe our system in the basis of dressed states. In contrast to the discussion in subsection 2.2.1, we will include the effects of interactions, which leads to a break down of the single spatial mode approximation. This approach provides an intuitive explanation of the observations as demixing dynamics of the dressed states. The properties of *interacting* dressed states were derived by Search et al. [33] and Jenkins et al. [89, 90] and these papers serve as the theoretical foundation for this section.

The equations of motion Equation 2.3 can be rewritten in the dressed state basis, i.e. in the eigenstates of the linear coupling Hamiltonian when neglecting interactions. In this basis, the linear coupling terms vanish, which simplifies the description of the dynamics because the population in each dressed state is conserved.

When including interactions, this advantage does not hold any more as the interactions introduce two classes of additional terms: Some conserve the number of particles in the new basis states while others exchange population between them [33]. However, in the limit of strong coupling, when the energy difference between the dressed states dominates over the mean field interactions, $\hbar\Omega \gg n g_{ij}$, two-body interactions can be simplified and the non-population-conserving terms are suppressed.[2] This effect can be illustrated by the following energetic consideration [33]: The conversion from one dressed state into the other requires the energy $\hbar\Omega$. If the inequality above is fulfilled, the mean field energy is not sufficient to overcome this energy difference.

Therefore, Rabi oscillations can be expressed as a superposition of interacting dressed states, each of whose populations are conserved in the limit of strong linear coupling. The equations of motion

[2]The condition for the strong coupling regime was derived for the general case of arbitrary detuning. In our case of a resonant coupling, it relaxes to $\hbar\Omega \gg \frac{n}{2}(g_{11}-g_{22})$, $\frac{n}{2}(g_{11}+g_{22}-2g_{12})$. This condition is fulfilled for our experimental parameters as $520\,\mathrm{Hz} \gg 25\,\mathrm{Hz}$.

for the dressed states are equivalent to those for atomic states in the experiments of the previous chapter, where we discussed the evolution of an initial superposition of two components in the absence of linear coupling. For resonant coupling, the interactions between the dressed states are parametrized by the effective scattering lengths $a_{++} = a_{--} = \frac{1}{4}(a_{11} + a_{22} + 2a_{12})$ and $a_{+-} = \frac{1}{2}(a_{11} + a_{22})$ [33, 89], which take over the role of the atomic scattering lengths a_{11}, a_{22}, a_{12} in the equations of motion.

In analogy to the (im-)miscibility condition for atomic condensates (Equation 2.9), the condition for stability against demixing reads $a_{+-}^2 < a_{++}a_{--}$ for the dressed states [89]. In terms of the atomic scattering lengths, this corresponds to $a_{12} > \frac{1}{2}(a_{11} + a_{22})$. Thus, for equal intra-species scattering lengths $a_{11} = a_{22}$, which is a good approximation for ^{87}Rb, the miscibility conditions for atomic and dressed states are mutually exclusive – dressed states are immiscible where atomic states are miscible and vice versa.

In this context, the slow dynamics in the envelope of the Rabi oscillations results from a reduced overlap of the dressed states due to spatial separation [90]. The complementary stability condition for atomic and dressed states is the reason for the counter-intuitive behavior of a reduced oscillation amplitude in the miscible regime of the atoms. In the numerical simulations, both the amplitude and the relative phase of the two atomic components are known, such that the density profiles of the corresponding dressed states can be calculated. The results are shown in Figure 4.5.

The dressed state picture also provides an intuitive explanation for the role of the gradient κ in the linear coupling strength. As $a_{++} = a_{--}$ the two dressed states are initially symmetric with respect to spatial separation and in a metastable state. Small perturbations, e.g. in the relative population of the dressed states, lead to symmetric demixing as shown in the left panel of Figure 4.5. However, the symmetry can be broken, for example by external state-dependent forces. As the energy shift of the dressed states is given by $\pm\frac{\hbar\Omega}{2}$ (see subsection 2.2.1), the gradient leads to an effective state-dependent potential $V_\pm(x) = V(x) \pm \frac{\hbar}{2}\kappa x$. The minima of $V_\pm(x)$ are displaced by $\Delta x = \pm\frac{\hbar\kappa}{2m\omega_x^2} = \pm 11\,\mathrm{nm}$ with respect to the state-independent optical dipole potential $V(x)$. This small perturbation leads to biased antisymmetric demixing and thus a qualitative change in the dynamics, which demonstrates the criticality of the system to symmetry breaking. Furthermore, the persistent spatial overlap in the miscible regime of the dressed states shows that the bare effect of the state dependent effective potential is small.

As Rabi oscillations result from interference of the dressed states, the oscillation amplitude decreases as the profiles of the dressed states deviate from a balanced superposition. This connection is essential for the reconstruction of spatial dressed state profiles from the experimental data and will be discussed in the next section.

4.2.1. Reconstruction of dressed states from spatially resolved Rabi oscillations

In the experimentally observed Rabi oscillations only the density profiles of the atomic states are measured and their relative phase is not directly accessible. Thus, the spatial profiles of the dressed states cannot be directly calculated. For their reconstruction we need a deeper understanding of the connection between the amplitude and phase of Rabi oscillations and the underlying dressed states. It follows that the density profiles of the dressed states can be extracted from an analysis of the *local* amplitude $A(x)$ and phase $\varphi(x)$ of the oscillations.

Let us expand Equation 4.1 to include a possible imbalance in the dressed states as well as a relative

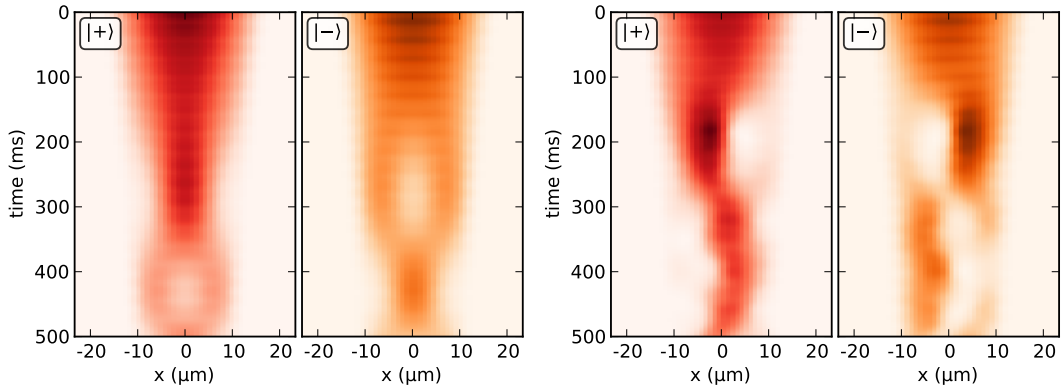

Figure 4.5.: Simulated dressed state density timetrace at $B = 9.17\,\mathrm{G}$, i.e. in the dressed state immiscible regime, without (left) and with (right) the gradient in the coupling strength. In numerical simulations, both the probability amplitude profile and the relative phase of the atomic states are accessible allowing to directly deduce the density timetrace of the dressed states. Ignoring the gradient in the coupling strength leads to symmetric component separation (left). The symmetry breaking caused by the inhomogeneity in the coupling strength manifests itself in a faster, more pronounced and antisymmetric spatial separation of the dressed states (right). Data shown in the left panel corresponds to the dashed black line in Figure 4.2, the right panel to the solid one.

phase φ

$$\begin{aligned} |\psi(t)\rangle &= \cos\alpha \cdot e^{-i\Omega t/2} e^{-i\varphi/2} |+\rangle + \sin\alpha \cdot e^{+i\Omega t/2} e^{+i\varphi/2} |-\rangle \\ &= \frac{1}{\sqrt{2}} (\cos\alpha \cdot e^{-i(\Omega t+\varphi)/2} + \sin\alpha \cdot e^{+i(\Omega t+\varphi)/2}) |1\rangle \\ &\quad + \frac{1}{\sqrt{2}} (\cos\alpha \cdot e^{-i(\Omega t+\varphi)/2} - \sin\alpha \cdot e^{+i(\Omega t+\varphi)/2}) |2\rangle \end{aligned} \tag{4.2}$$

where the mixing angle α describes the relative population of the dressed states and the use of sin () and cos () ensures normalization. The corresponding imbalance z of the atomic states is given by

$$z = \frac{N_2 - N_1}{N_1 + N_2} = \frac{|\langle 2|\psi(t)\rangle|^2 - |\langle 1|\psi(t)\rangle|^2}{|\langle 1|\psi(t)\rangle|^2 + |\langle 2|\psi(t)\rangle|^2} = -2 \sin\alpha \cdot \cos\alpha \cdot \cos(\Omega t + \varphi) \tag{4.3}$$

Thus, the local phase $\varphi(x)$ of the Rabi oscillations is equivalent to the relative phase of the dressed states, while a spatial change in the amplitude

$$A(x) = |2 \cdot \sin\alpha(x) \cdot \cos\alpha(x)| = |\sin(2\alpha(x))| \tag{4.4}$$

corresponds to a changing imbalance of the dressed states. The amplitude is maximal for an equal superposition of the dressed states, $\alpha = \pi/4$, and is reduced as their imbalance increases. Thus, the decrease of the integrated, i.e. global oscillation amplitude shown in Figure 4.2 can be explained by a reduced overlap of the dressed states due to their spatial separation.

Due to the $\pi/2$-periodicity of the amplitude A in α, the mixing angle deduced from the measured oscillation amplitude can not be unambiguously mapped onto the amplitudes of each dressed state. For example, the superpositions of dressed states $|\psi_1\rangle = \cos\alpha|+\rangle + \sin\alpha|-\rangle$ and $|\psi_2\rangle = \sin\alpha|+\rangle +$

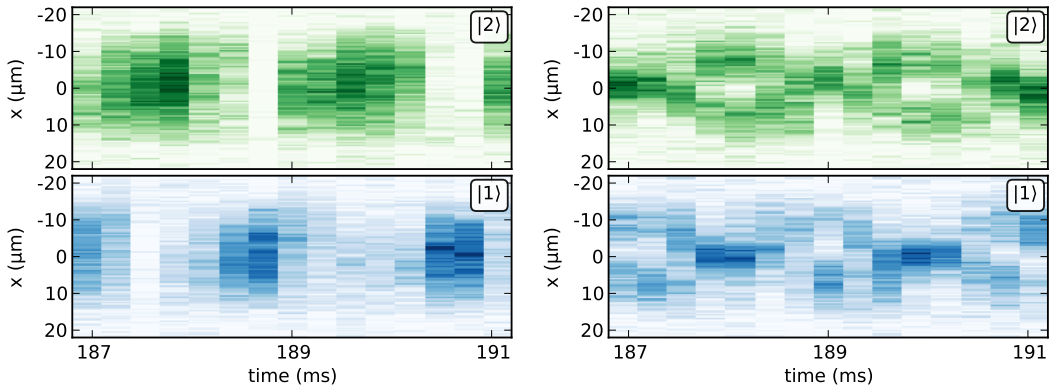

Figure 4.6.: Spatially resolved Rabi oscillations. At $B = 9.03\,\mathrm{G}$ (left), the oscillations are in phase over the extent of the atomic cloud. In contrast at $B = 9.17\,\mathrm{G}$ (right) the phase of the oscillations in the wings of the cloud is shifted by π with respect to its center and the oscillation amplitude is reduced for intermediate distances from the cloud center. This information about the local amplitude and phase allows to reconstruct the profiles of the dressed states.

$\cos\alpha|-\rangle$ both yield the same amplitude in the corresponding Rabi oscillations. Consequently, only the difference of the amplitudes at each point in space can be deduced and it is not clear which amplitude is mapped onto which dressed state.

Further information is required to reconstruct the profiles of the dressed states. For example, a phase jump of π in the oscillations corresponds to a node in the amplitude of one of the dressed states, i.e. it changes its sign with respect to the other state. Furthermore, we can assume the integrated populations of the dressed states to remain equal during the time evolution, as their reduction in amplitude due to atom loss is symmetric. Using these phase and symmetry arguments, the relative probability amplitudes of the dressed states can be reconstructed. Their absolute density profile can be deduced by multiplying the square of the relative amplitudes with the measured atomic sum density profile.

As an example, we consider the Rabi oscillations at $B = 9.03\,\mathrm{G}$ and $B = 9.17\,\mathrm{G}$ around $t \approx 190\,\mathrm{ms}$ shown in Figure 4.6. A sinusoidal fit to the time evolution in each spatial bin yields the local amplitude and phase of the oscillations. Using these fit results, the profiles of the dressed states can be reconstructed using the procedure outlined above. Figure 4.7 illustrates the method along with the results.

In order to assign the extracted dressed state density profiles to the $|+\rangle$ or the $|-\rangle$ state, we remember that the gradient κ causes an effective potential for the dressed states. As the Rabi frequency increases for increasing x, the energy of the ground state $|+\rangle$ is decreased. Thus, we identify the state on the right with $|+\rangle$ and the left one with $|-\rangle$.

The dressed state profiles reconstructed from the Rabi oscillations at $B = 9.17\,\mathrm{G}$ confirm the model of antisymmetric demixing in the dressed basis. Their overlap is minimized, where the $|+\rangle$ state occupies the right half of the trap and the $|-\rangle$ state is on the left. At $B = 9.03\,\mathrm{G}$, the overlap of the inferred dressed state profiles is only slightly decreased. This demonstrates the miscibility of the dressed states and confirms that the gradient in the linear coupling strength is only a small perturbation. The separation between the maxima of the dressed state densities is about $4\,\mu\mathrm{m}$. This increase compared to the shift of the effective potentials is due to the remaining repulsive interactions between the miscible dressed states.

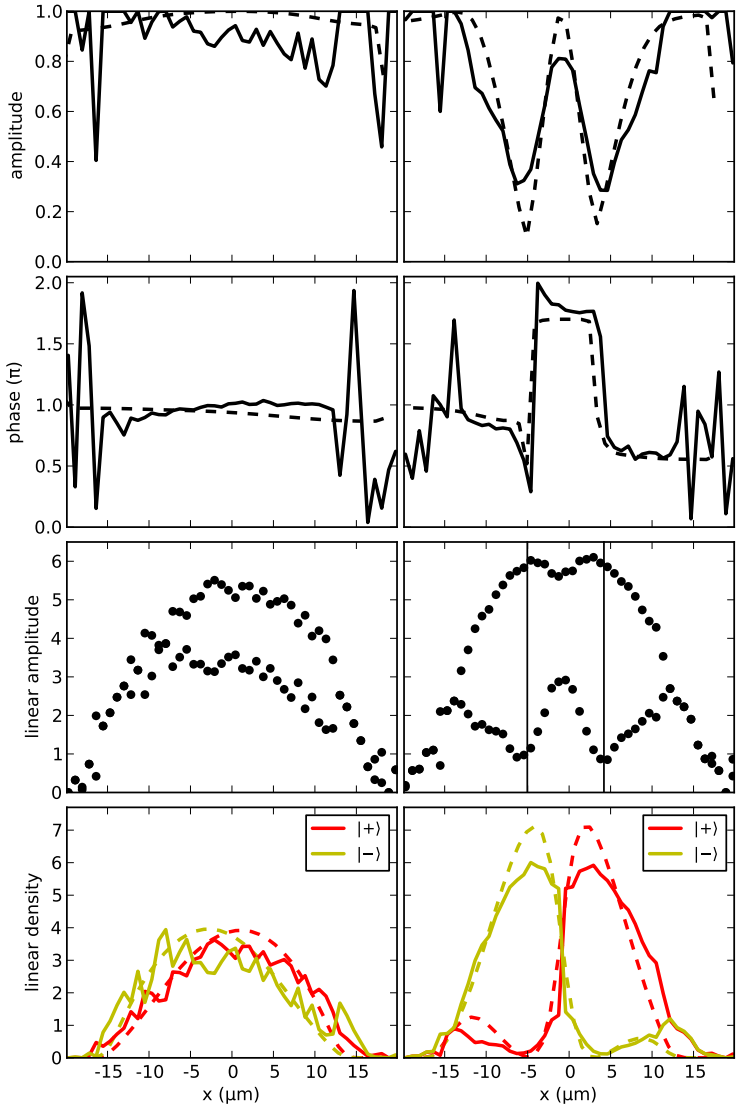

Figure 4.7.: Reconstruction of the dressed state profiles from the local amplitude (top row) and phase (second row) of the Rabi oscillations at $B = 9.03\,\mathrm{G}$ (left column) and $B = 9.17\,\mathrm{G}$ (right column) shown in Figure 4.6. On the left, neither amplitude nor phase of the oscillations vary in space. On the right, the oscillations in the center of the cloud are out of phase with respect to its edges. This phase jump is accompanied by a reduction in oscillation amplitude. The increased noise of the fit results at the edges of the atomic cloud is due to the reduced atom density. Using Equation 4.4 the relative probability amplitudes of the dressed states are deduced at each pixel (third row), but cannot be assigned to the dressed states (i.e. it is not clear how to connect the points in order to yield the dressed state profiles). Using the fact that a phase jump of π (vertical lines) corresponds to a node in the amplitude of one of the dressed states and assuming equal populations of the two components, the normalized density profiles of the dressed states (bottom row) are inferred. For comparison, the dashed lines show the corresponding data of the numerical simulations, where the dressed state profiles in the bottom row have been calculated directly from the amplitudes and relative phase of the atomic wave functions.

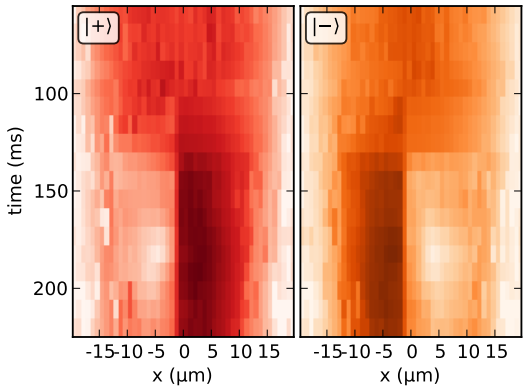

Figure 4.8.: Timetrace of the dressed state density profile reconstructed from the observed Rabi oscillations. The demixing dynamics of an initially overlapping superposition of dressed states is in good agreement with numerical simulations shown in Figure 4.5.

This reconstruction procedure can be repeated at different evolution times in order to obtain the full timetrace of the demixing dynamics of an equal superposition of interacting dressed states. The results are illustrated in Figure 4.8 and are in good agreement with the simulations shown in Figure 4.5. Note that the reconstruction of the dressed states relies on fitting a sine to the local oscillations for the extraction of amplitude and phase and thus requires *coherent* oscillations. This requirement is not necessary for analyzing the dynamics in the envelope of the oscillations shown in Figure 4.2. There, only the 'single shot amplitude' is relevant, i.e. the maximum observed amplitude per oscillation cycle. This makes the reconstruction of the dressed states unreliable for evolution times $> 230\,\mathrm{ms}$.

In summary, we have prepared a superposition of *interacting* dressed states, realized by Rabi oscillations in an interacting Bose-Einstein condensate. The reduced oscillation amplitude could be attributed to phase separation of the dressed states, whose miscibility criterion is opposite to that of the atomic states. In particular, the intra-species scattering lengths of the dressed states are equal resulting in an intrinsically symmetric system ideal for the study of criticality and symmetry breaking. In our experiments, the symmetry is broken by an inhomogeneous Rabi frequency, which results in a qualitative change in the demixing dynamics and illustrates the criticality as revealed by comparison with numerical simulations. The spatial profiles of the dressed states were reconstructed by a local analysis of the amplitude and phase of the Rabi oscillations.

5. A miscible-immiscible phase transition

In the previous chapter we have presented the concept of interacting dressed states, which result from the interplay between atomic interactions and a linear coupling in a two-component Bose-Einstein condensate. We have analyzed Rabi oscillations between atomic states as a superposition of interacting dressed states and found that their miscibility condition is opposite to the atomic states.

We begin this chapter by reporting on the experimental generation of single dressed states via a novel non-adiabatic preparation scheme. Dressed states are an equal superposition of the atomic states and are stationary if the amplitude of the linear coupling exceeds the energy scale of the atomic interactions. Their stationarity implies that the two atomic states are effectively miscible even if their scattering parameters in the absence of the linear coupling are immiscible. The linear coupling strength acts as a control parameter for this theoretically predicted miscible-immiscible phase transition [17, 18].

We extend the discussion beyond the strong coupling limit of the dressed states and observe the phase transition from miscible to immiscible. We characterize the phase transition by the linear response of the system to sudden quenches to the proximity of the critical point. We observe a power law scaling in the characteristic length scales on both sides of the phase transition in agreement with mean field predictions. The dynamic range for the scaling measurements is expanded by employing effectively negative coupling strengths.

5.1. Non-adiabatic generation of dressed states

The concept of dressed states has been introduced in subsection 2.2.1 and the previous chapter discussed effective interactions in a superposition of dressed states. Single dressed states have been generated in quantum gases [87, 91] following an adiabatic preparation scheme [31] as follows: All atoms are initially prepared in a single atomic hyperfine state, which in the limit of large detuning is an eigenstate of the linear coupling Hamiltonian. The linear coupling field is switched on with a low amplitude and far detuned from the atomic transition. The amplitude is subsequently increased and the detuning is decreased slowly such that the atomic state adiabatically follows. When the frequency of the coupling field reaches resonance with the atomic transition a dressed state is prepared.

For a large amplitude of the coupling field dressed states are very stable against external perturbations, e.g. magnetic field fluctuations. For example it has been demonstrated that a microwave dressing increases the coherence times in trapped ions by more than two orders of magnitude while still allowing for fast quantum logic with the ions [92]. This experiment employed a similar adiabatic preparation scheme via an incomplete stimulated Raman adiabatic passage and has been proposed as a route to improve coherence times for quantum computing [92].

These adiabatic methods for the generation of dressed states require a controlled change of the detuning from the atomic transition. The duration of the state preparation is given by multiple Rabi periods. In this section we present a novel non-adiabatic scheme for the generation of dressed states which does not require a sweep in the detuning but only a sudden change in the phase of the linear coupling [22]. For transitions involving radio-frequency radiation this method is straightforward

to implement as arbitrary waveforms can be generated for radiation in the Megahertz range. The time scale for the preparation is given by a quarter of a Rabi period and is significantly shorter than the adiabatic scheme. This is advantageous in the presence of increased atom loss. In our experiments the duration of the $\pi/2$-pulse ranges from tens to hundreds of microseconds depending on the employed transitions.

5.1.1. Experimental sequence

The experimental sequence begins with a Bose-Einstein condensate of atoms in a single substate of the $F = 1$ manifold. A resonant $\pi/2$-pulse creates an equal superposition of two hyperfine components $|1\rangle$ and $|2\rangle$ corresponding to a coherent spin state. After the pulse we switch the phase of the coupling field by $\Delta\varphi = \pi/2$ relative to the first pulse within 1 µs. This phase shift aligns the rotation axis of the linear coupling to be parallel with the atomic state on the Bloch sphere. As discussed in subsection 2.2.1 the effective spin is stationary under the action of the linear coupling Hamiltonian and a $|+\rangle$ dressed ground state is prepared. Similarly a phase shift of $\Delta\varphi = 3\pi/2$ aligns the rotation axis to be antiparallel to the atomic state and corresponds to the generation of an excited $|-\rangle$ dressed state. In the following, we refer to a linear coupling whose rotation axis is aligned with the pseudo-spin of the atomic states as a *dressing field*.

The dressed state picture is valid if the energy of the linear coupling exceeds the energy scale of the interactions and can be applied if $\Omega \gg \Omega_c = -ng_s$ as defined in subsection 2.4.1. In the context of the internal Josephson junction discussed in subsection 2.2.2 this scheme for the generation of dressed states is equivalent to zero-amplitude plasma and π-oscillations and the limit of strong coupling corresponds to being deep in the Rabi regime [24].

5.1.2. Experimental results

We have experimentally implemented the experimental sequence sketched above and realize dressed states in a Bose-Einstein condensate of 3500 atoms trapped in the charger (see subsection 3.1.1 for an introduction to the experimental system). In order to probe the effect of atomic interactions in the strong linear coupling regime we prepare dressed states both on the miscible ($B = 9.17G$) and the immiscible ($B = 9.05G$) side of the Feshbach resonance. The Rabi frequency for the initial $\pi/2$-pulse as well as the subsequent dressing is $\Omega \approx 2\pi \times 600\,\mathrm{Hz}$, which is much larger than the critical coupling strength of $\Omega_c \approx 2\pi \times 30\,\mathrm{Hz}$.

In the single spatial mode approximation a dressed state is represented by a stationary pseudo-spin vector on the Bloch sphere. Both the population imbalance of the two states and their relative phase are constant. In order to verify the generation of a dressed state we test for these two characteristics. If the effect of interactions can be neglected also the extended atomic cloud in the charger can be described by a single spatial mode and no spatial structure in the imbalance or relative phase of the condensates is expected.

The corresponding experimental observations are summarized in Figure 5.1. The upper rows show the density timetraces of the two atomic states revealing equal density in the two components for the experimental time scale of 500 ms. Furthermore no spatial structure can be detected within the cloud, also at the immiscible side of the Feshbach resonance. This demonstrates that a dressing field prevents demixing dynamics because the system can be described as a stationary dressed state as predicted in [17]. The observed change in the atomic density profiles is due to atom loss.

In order to detect the relative phase of the two components we apply an additional $\pi/2$-pulse before detection, which translates the relative atomic phase into a population imbalance. In particular the $|+\rangle$ state is mapped onto the atomic state $|2\rangle$ and $|-\rangle$ onto $|1\rangle$. This sequence corresponds to a Ramsey interferometer [93] with a dressing field during the interrogation time. The results shown

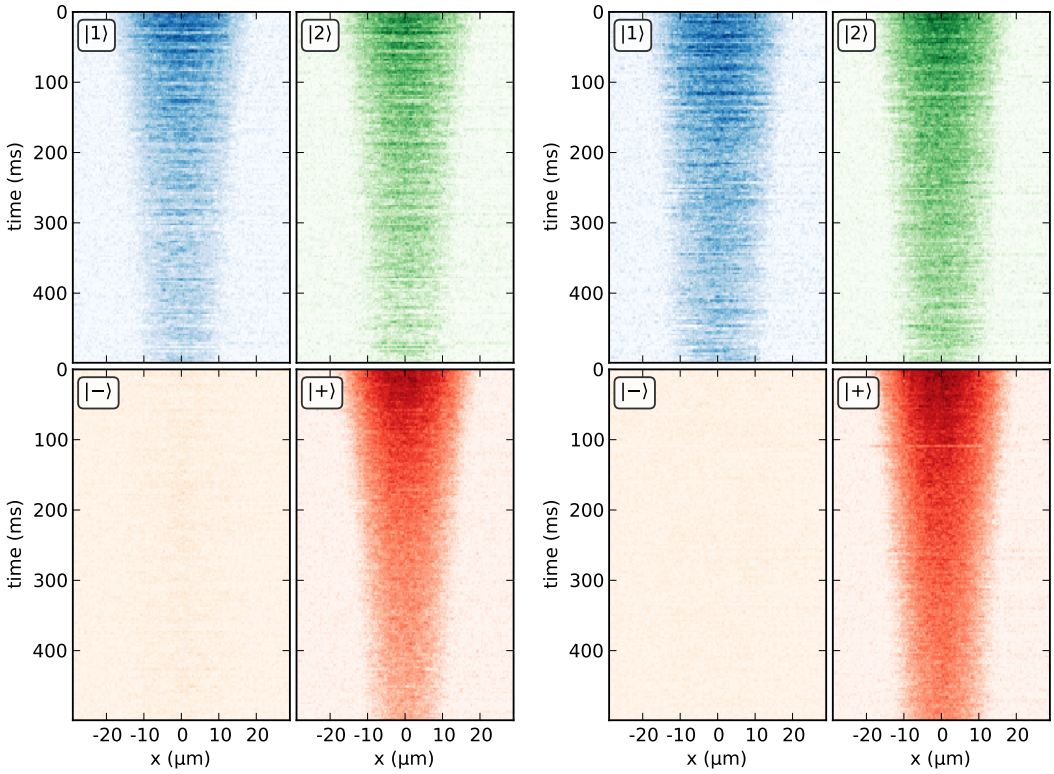

Figure 5.1.: Density timetrace of dressed states prepared at 9.05 G (left, immiscible) and 9.17 G (right, miscible). We generate a $|+\rangle$ dressed state employing the non-adiabatic preparation scheme. The overlap of the density profiles of the atomic states (top row) remains high both in the miscible and the immiscible regime and confirms that the dressing field stabilizes the system. An additional phase shifted $\pi/2$-pulse before detection allows to measure the relative phase of the two components and maps the dressed state $|+\rangle$ onto the atomic state $|2\rangle$ and $|-\rangle$ onto $|1\rangle$. The small population of the $|-\rangle$ state demonstrates the high fidelity of the preparation scheme of more than 96%.

in the bottom row of Figure 5.1 demonstrate a constant phase over the time evolution, i.e. phase coherence over hundreds of milliseconds. The population in $|1\rangle$ after the last $\pi/2$-pulse can be used to estimate the fidelity of the preparation scheme yielding $> 96\%$.

In conclusion we have experimentally generated dressed states using a non-adiabatic scheme. The preparation time is given by the duration of the initial $\pi/2$-pulse. We have shown that in the limit of strong coupling dressed states are stationary and that demixing dynamics of immiscible states is prevented.

5.2. Dynamics beyond the strong coupling limit

In order to study the effect of interactions and the resulting break-down of the dressed state picture we measure the time evolution in the presence of weak dressing fields. This allows us to observe the transition from the stationary dressed states presented in the previous section to interaction-dominated evolution for weak linear couplings strengths. The experiments are performed in the charger at the 'magic field' of $B = 3.23\,\mathrm{G}$. The employed atomic states are $|1\rangle = |1, -1\rangle$ and

$|2\rangle = |2,+1\rangle$ and their the scattering parameters are close to the miscible-immiscible threshold resulting in a critical coupling strength of $\Omega_c \approx 0$. The interaction properties of these states and their dynamics in the absence of a linear coupling field was discussed in subsection 3.2.1.

We employ the same experimental sequence as for the generation of dressed states, but reduce the amplitude of the microwave radiation after the initial $\pi/2$-pulse. The change in amplitude is performed along with the phase shift within 1 µs. The strength of the coupling field is reduced to various values ranging from $\Omega = 2\pi \times 0\,\mathrm{Hz}$ to $2\pi \times 45\,\mathrm{Hz}$ in order to study the dependence of the dynamics in the two components on the linear coupling strength. The power reduction in the coupling fields also causes a change in the light shift and their frequencies have to be adjusted accordingly to maintain resonance as discussed in subsection 3.1.2. Note that the power of the initial $\pi/2$-pulse is not reduced in order to minimize nonlinearity effects resulting e.g. in a phase error of the prepared superposition state.

We first discuss the dynamics for a phase shift of $\Delta\varphi = \pi/2$ after the initial coupling pulse. The observed dynamics for various coupling strengths is illustrated in the left panel of Figure 5.2. In the absence of a linear coupling we observe the same potential separation dynamics as presented in subsection 3.2.1. Atoms of component 2 are pushed to the edges of the trap and component 1 gathers in the trap center before the atomic clouds 'oscillate back' towards the spatial superposition state. As the dressing amplitude Ω is increased the depth of the density modulation in the trap center is reduced and the corresponding oscillation frequency increased. For $\Omega = 2\pi \times 45\,\mathrm{Hz}$ (bottom row of the Figure 5.2) the oscillations are barely visible. The density profiles of the atomic clouds are stationary and can be described as a $|+\rangle$ dressed state.

As discussed in subsection 3.2.1 the temporal average of the density profiles can be used as an estimate for the ground state of the system. The right panel of Figure 5.2 compares the mean of the observed density profiles of each component to the numerically computed stationary states employing Newton's method and the nonpolynomial nonlinear Schrödinger equation including the linear coupling (see subsection B.1.2 for details on the numerical methods). The transition to the dressed state for increasing Ω is apparent in the increasing overlap of the two components and the agreement of the experimental observations with the numerical calculations is good.

We similarly examine the break-down of the $|-\rangle$ dressed state by changing the phase of the radio frequency radiation by $\Delta\varphi = 3\pi/2$ after the initial coupling pulse. The resulting dynamics is summarized in Figure 5.3. The striking difference to the previous measurements occurs at small coupling strengths of about $\Omega = 2\pi \times 7\,\mathrm{Hz}$, where the frequency of the oscillation dynamics in the two components is reduced. In addition the role of the two components is reversed as component 1 is predominantly found in the center of the trap. However, as Ω is further in increased the overlap of the components is maximized again and the $|-\rangle$ dressed state is observed. These features are well visible in the temporal mean of the density profiles shown in the right panel of Figure 5.3. As the $|-\rangle$ state is not the ground state the numerically calculated profiles correspond to lowest energy stationary state with a relative phase of π between the atomic state and the linear coupling (corresponding to a negative value of Ω as discussed in section 2.5). While stationary, this state is not the ground state of the system. The measured mean density profiles agree well with the computed stationary states.

5.3. Linear response to quenches near the critical point

While the charger is well suited for experiments estimating stationary states via potential separation dynamics, the small longitudinal extent of the atomic cloud prevents a detailed study of the miscible immiscible transition. A quantitative characterization of the phase transition requires an experimental system much larger than the characteristic length scales to be measured. In addition,

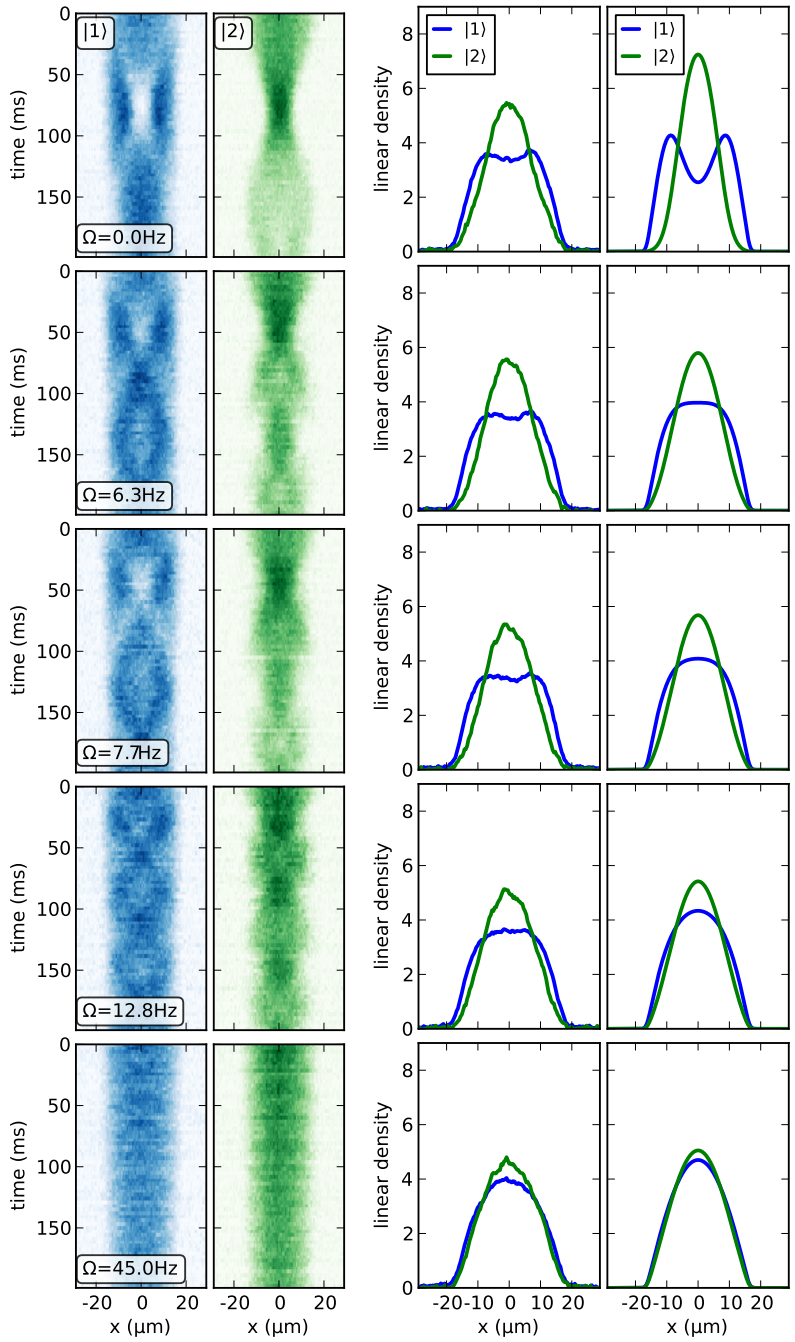

Figure 5.2.: Spatial dynamics of the two components for various amplitudes Ω of the linear coupling field. The phase is changed by $\Delta\varphi = \pi/2$ after the initial $\pi/2$-pulse. (left panel) Component separation is suppressed by the dressing field while the frequency of the density oscillations in the center of the trap increases. At $\Omega = 45\,\mathrm{Hz}$ (bottom row) no component separation is observed and a $|+\rangle$ dressed state is generated. (right panel) The temporal mean of the measured density profiles is in good agreement with numerically simulated ground state profiles in the presence of the linear coupling.

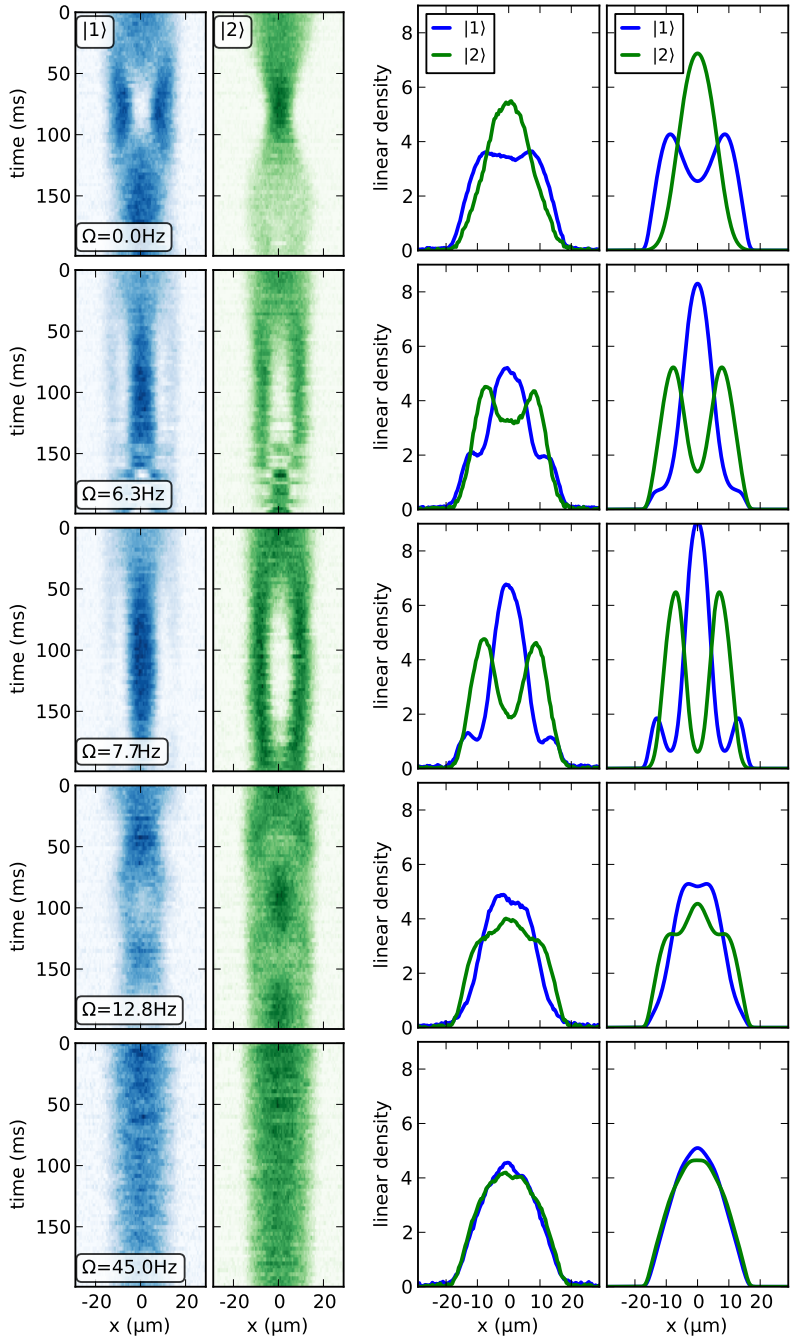

Figure 5.3.: Spatial dynamics of the two components for various amplitudes of the linear coupling field. The experimental sequence is the same as for Figure 5.2 but $\Delta\varphi = 3\pi/2$. This corresponds to the generation of the $|-\rangle$ dressed state for strong coupling (bottom row). (left panel) Compared to the absence of a coupling field the roles of the two states are inverted for small Ω as atoms in state $|2\rangle$ are pushed to the edges of the trap while component $|1\rangle$ occupies the trap center. (right) This behavior is apparent in the temporally averaged density profiles in agreement with numerically computed stationary states of the system shown on the right. The reduced modulation depth of the experimental profiles may be attributed to spin relaxation loss in state $|2\rangle$.

the value of the critical coupling strength marking the transition point depends on the atom density, which in inhomogeneous systems leads to a spatial dependence of the critical point. In order to reduce this effect an atomic cloud with a close-to-homogeneous density distribution is required.

As discussed in subsection 2.4.4 and subsection 3.2.2 the waveguide fulfills these requirements. We concluded in chapter 3 that magnetic fields of 9.07 G to 9.08 G near the Feshbach resonance are the optimal working points for the study of the phase transition as they offer a good compromise of small characteristic length scales, fast growth rates, a sufficient life time and atom loss which is symmetric in the two components. The experiments presented in the remainder of this chapter are conducted at these magnetic fields. The interaction parameters along with our typical linear atom densities of about 230 atoms/µm result a critical coupling strength of $\Omega_c \approx 2\pi \times 50\,\mathrm{Hz}$ at 9.07 G and $\Omega_c \approx 2\pi \times 70\,\mathrm{Hz}$ at 9.08 G.[1]

We characterize the phase transition by measuring the response of the system to sudden quenches of the control parameter Ω. We parametrize the distance to the critical point by the dimensionless quantity $\varepsilon = (\Omega - \Omega_c)/\Omega_c$ which vanishes at the critical point. $\varepsilon > 0$ ($\varepsilon < 0$) denotes the miscible (immiscible) side of the phase transition. The quenches start deep in the miscible regime $\varepsilon \gg 1$ and end in the proximity of the critical point. The experimental observable in our measurements is the autocorrelation function of the spin profile (or equivalently the corresponding Fourier spectrum) at a hold time t after the quench (see subsection 3.2.3 for a summary of the analysis methods).

On the miscible side of the phase transition, $\Omega > \Omega_c$, we expect correlations in the fluctuations on top of a flat spin profile, i.e. the autocorrelation function decays to zero on a characteristic length scale ξ_c. The value of ξ_c depends on the distance to the critical point as $\xi_c(\varepsilon) = \xi_0/|\varepsilon^\nu|$ with a mean field scaling exponent of $\nu = 1/2$. ξ_0 is proportional to the spin healing length ξ_s as discussed in chapter 2. The spin correlations need a finite time to develop after the quench. This relaxation time is given by $\tau = \hbar/g(\varepsilon)$, where g denotes the energy gap in the Bogoliubov spectrum as discussed in subsection 2.4.3.

On the immiscible side of the phase transition, $\Omega < \Omega_c$, the initial equal superposition of the two components is unstable. Small fluctuations of the spin profile act as a seed for excitation modes and are amplified in a range of wave vectors resulting in the formation of spin patterns. The characteristic length scale in the immiscible regime is given by the unstable mode with the smallest wavelength k_c. As we have seen in subsection 2.4.3 it diverges near the critical point like $\sqrt{\Omega_c - \Omega}$. Using the same notation as in the miscible regime the characteristic length shows the same behavior $\xi_c(\varepsilon) = \xi_0/|\varepsilon^\nu|$ with $\nu = 1/2$ and $\xi_0 = 2\pi/k_c(\Omega = 0) = \sqrt{2}\pi\xi_s$. The characteristic time scale in the immiscible regime is the maximum growth rate of the unstable modes. Close to the critical point at $\Omega_c/2 < \Omega < \Omega_c$ it is given by the inverse modulus of the gap, but stays constant for $\Omega < \Omega_c/2$. Thus, we expect temporal scaling only close to the critical point. The mean field spatial and temporal scaling properties are summarized in Figure 5.4.

The experimental sequence for the implementation of the sudden quenches is identical to the one employed in the previous section for the experiments in the charger. We prepare an equal superposition of the two atomic clouds by an initial $\pi/2$-pulse and subsequently change the phase of the radio frequency radiation by $\Delta\varphi = \pi/2$. The amplitude of the coupling field is simultaneously reduced to a value near the critical coupling Ω_c.

As we will now argue, the initial configuration after the $\pi/2$-pulse corresponds to the equilibrium state for $\Omega \gg \Omega_c$. As the pulse duration of $\tau_{\pi/2} \approx 700\,\mu\mathrm{s}$ is shorter than the typical time scale for the dynamics of the atomic cloud and the spin correlations, the density profile of each component after the pulse is the same as the spatial profile of the $|1\rangle$ component before the pulse (only reduced in amplitude by a factor 2). Thus, the density fluctuations in the two components are in-phase, and the

[1] For simplicity the values for Ω are given in some graphs without the preceding factor of 2π. The unit Hertz always denotes temporal frequencies and not angular frequencies in order to avoid ambiguity.

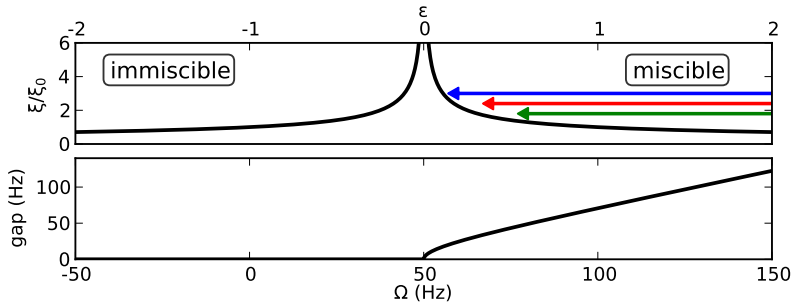

Figure 5.4.: Scaling of the characteristic length and time scales at the miscible-immiscible phase transition in the mean field approximation. The length scale on the miscible side of the phase transition is given by the correlation length of the spin fluctuations and on the immiscible side by the wavelength of the unstable modes in the excitation spectrum. Both diverge at the critical point with a scaling exponent of $\nu = 1/2$. The relaxation time scales as the inverse of the energy gap in the excitation spectrum. Close to Ω_c the corresponding scaling exponent is $\nu z = 1/2$. The arrows illustrate the experimental sequence of quenches from $\Omega \gg \Omega_c$ to the proximity of the critical point.

corresponding spin profile is flat. Only uncorrelated shot noise due to the splitting process is present. As the $\pi/2$-pulse creates a coherent state, the shot noise fluctuations have no preferred length scale and all spin excitation modes are equally populated with a small amplitude. This configuration corresponds to a dressed state, i.e. the eigenstate in the system in the limit of large coupling $\Omega \gg \Omega_c$. In the effective magnetic field picture of the dressing field presented in subsection 2.4.3, this configuration corresponds to a strong magnetic field. Each spin is aligned to the axis of the field and all spin fluctuations are suppressed, which leads to a vanishing of the associated correlation length. We have tested these assumptions about the state after the $\pi/2$-pulse by dressing the atoms with a strong linear coupling field of $\Omega = 2\pi \times 340\,\mathrm{Hz}$ after the pulse. No dynamics in the density profiles or in the spin correlations could be detected within the spatial resolution of the imaging system.

5.3.1. Scaling on the miscible side of the transition

We begin the discussion of the experimental observations with sudden quenches to the miscible side of the phase transition $\Omega \gtrsim \Omega_c$ as illustrated by the arrows in Figure 5.4. We quench to several values of ε and measure the spin correlations of the system at different hold times t after the quench. As our detection method is destructive, we cannot detect the dynamics of the correlations in a single experimental realization but have to repeat the experiment under the same conditions and vary the hold time after the quench. We average over $10 - 20$ experimental realizations for each hold time t and distance from the critical point ε.

When experimentally probing the dynamics in the spin correlations it is important to keep the distance from the critical point ε constant. Due to the proximity to the Feshbach resonance, atom loss is strongly enhanced and the $1/e$-lifetime of the atomic cloud for these measurements is approximately 30 ms. Many parameters of the system depend on the linear atom density, in particular $\Omega_c \propto n$. In order to compensate for the changing atom density, we adjust the amplitude of the linear coupling $\Omega(t) \propto n(t)$, such that the ε remains constant. This procedure compensates for the first order effects of the atom loss, but some other effects remain, e.g. a change in the spin healing length $\xi_s \propto 1/\sqrt{n}$. Note that whenever Ω is used as a control parameter in the remainder of this chapter, for example as an axis label in graphs, we refer to its initial value $\Omega(t = 0)$.

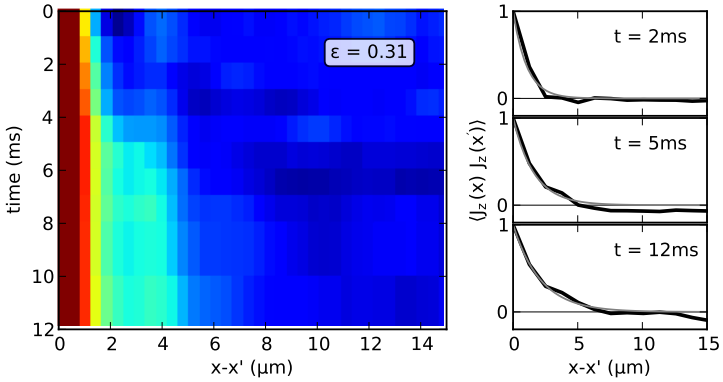

Figure 5.5.: Dynamics of spin correlations after a sudden quench to an exemplary value of ε on the miscible side of the phase transition. (right panel) The autocorrelation function of the spin profile (black lines) decays to zero with in a few micrometer. The decay length increases with the hold time t after the quench. An exponential fit (gray lines) is employed to extract the characteristic length scale. (left) Time evolution of the correlation functions in false color illustrating the growth of the correlation length.

The linear atom density not only changes temporally, but also spatially as the atomic cloud is confined in an elongated harmonic trap. The spatial profile $n(x)$ results in a spatial variation of the previously mentioned parameters such as the critical coupling strength, $\Omega_c = \Omega_c(x)$. In order to reduce these inhomogeneity effects we restrict the analysis to the central part of the atomic cloud where the gradient of the density profile is minimal. We choose a region with a width of about 150 µm around the trap center. The density at the edge of this analysis region is reduced by about 15% compared to the peak density, such that the value of Ω_c is smeared by about this amount in the experiments.

An example of the observed spin correlation functions and their change in time is shown in Figure 5.5. The normalized correlation functions decay to zero within a few micrometers. Immediately after the quench the length scale of the decay is minimal and is determined by the detection limit of our imaging system given by the resolution of imaging optics. The size of one pixel of the CCD chip corresponds to 420 nm in the plane of the atomic cloud and is thus smaller than the resolution of the imaging optics of 1.1 µm in the Rayleigh criterion [75]. In order to reduce the effect of photon shot noise we bin the spin profile over three neighboring pixels before calculating the correlation functions. The decay length of the correlations functions increases during the time evolution after the quench. In order to quantify the characteristic length scale of the system, we associate the correlation length ξ with the $1/e$-decay length of an exponential fit to the autocorrelation functions. Using this method we extract the correlation length from the averaged correlation functions at each value of ε and hold time t.

The time evolution of the correlation length for three values of ε is shown in Figure 5.6. After the quench we observe a linear growth in ξ with a slope independent of the value of ε After a characteristic time depending on ε, this growth rate is reduced and the correlation length saturates. We identify the saturation value of the correlation length with the characteristic length scale of the spin fluctuations ξ_c at a given ε. Note that the numerical value of ξ_c is not necessarily identical to the equilibrium spin correlation length. However, in the linear response regime it is expected to show the same scaling behavior with ε.

The resulting scaling of ξ_c with ε is summarized in Figure 5.7. ξ_c increases when approaching the critical point Ω_c and agrees well with a power law fit. The power law scaling becomes apparent by

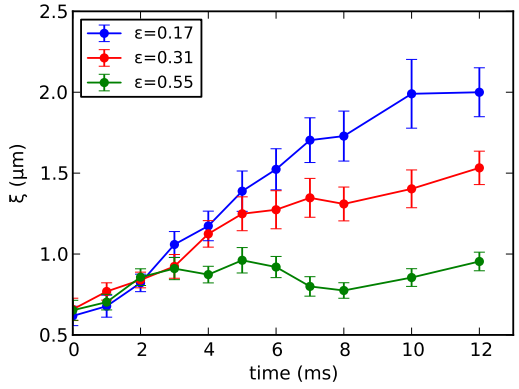

Figure 5.6.: Temporal evolution of the correlation length. The correlation length is extracted using an exponential fit to the autocorrelation function of the spin profile at each value of ε and t. Its time evolution is plotted for different distances ε from the critical point. After an initial linear growth with a rate independent of ε the growth slows down and the value of the correlation length saturates at ξ_c. This saturation value increases when approaching the critical point.

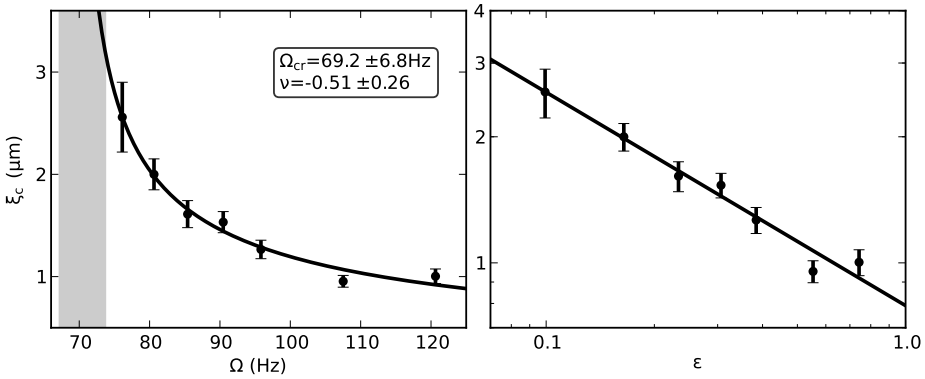

Figure 5.7.: Scaling of the correlation length with the distance from the critical point. The correlation length after an evolution time of $t = 12\,\mathrm{ms}$ (black circles) increases with a power law when approaching the critical point. A fit (solid line) yields an exponent of $\nu = 0.51 \pm 0.26$, which agrees with the mean field prediction of $\nu = 1/2$. A critical coupling strength of $\Omega_c = 69.2 \pm 6.8\,\mathrm{Hz}$ is found in agreement with the prediction of $\Omega_c = 70.5\,\mathrm{Hz}$ based on independent measurements of the atom density and the interspecies scattering length (gray shaded area). The right panel shows the same data on a double-logarithmic scale, where linearity indicates a power law scaling. All errors are given as two standard deviations.

the linearity on a double logarithmic scale. Both the scaling exponent $\nu = 0.51 \pm 0.26$ and the value of the critical coupling $\Omega_c = 69.2 \pm 6.8\,\mathrm{Hz}$ are extracted from a power law fit to the experimental data and in good agreement with the theoretical mean field prediction of $\nu = 1/2$. These values result from a fit $\xi_c(\Omega) = \xi_0 \left(\frac{\Omega - \Omega_c}{\Omega_c}\right)^{-\nu}$ with three free parameters ξ_0, ν and Ω_c. Reducing the number of fit parameters by fixing them to the theoretically predicted values for our system parameters yields smaller uncertainties. Setting $\nu = 1/2$ results in a fit value of $\Omega_c = 69.5 \pm 1.5\,\mathrm{Hz}$, while using the theoretical prediction $\Omega_c = 70.5\,\mathrm{Hz}$ yields $\nu = 0.47 \pm 0.05$. The fit with three free parameters yields $\xi_0 = 0.79 \pm 0.10\,\mu\mathrm{m}$, which is smaller than the prediction for the equilibrium

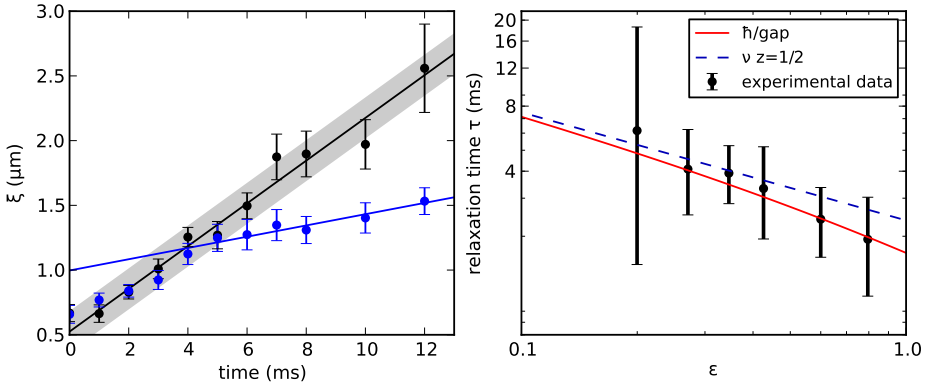

Figure 5.8.: Scaling of the relaxation time after a sudden quench. (left panel) We associate the relaxation time of the system with the position of the kink in the time evolution of the correlation length, which separates the fast initial growth from the subsequent saturation. The kink is found by linearly fitting the evolution of the correlation length (blue line) where it deviates from the initial growth (gray shaded area) and calculating the intersection point with a fit to the initial dynamics (black line). This procedure is repeated for each ε. The results are summarized in the right panel and agree well with the prediction of $\hbar/\text{gap}$ (red line). The error bars correspond to 2 s.d and are obtained by propagation of the uncertainties of the linear fits. The power law scaling prediction of $\nu z = 1/2$ (blue dashed line) is only valid close to the critical point. All theory curves are without free parameters.

value of $\xi_0 = \xi_s/\sqrt{2} = 0.90\,\mu\text{m}$. All errors are given as two standard deviations corresponding to a 95% confidence interval.

A characteristic time scale in the temporal evolution of the correlation length is the position of the kink where the growth of ξ slows down and saturates. We associate the position of the kink with the relaxation time τ of the system. It is determined from the intersection point of linear fits to the evolution of the correlation length before and after the kink as illustrated in the left panel of Figure 5.8. As the initial growth rate of the correlation length is the same for all values of ε, we model it by a linear fit to the evolution of the smallest value of ε, which remains linear within the measurement time. We associate the evolution after the kink with hold times where the measured correlation lengths ξ deviate from the fitted slope of the initial dynamics. The evolution of the correlation lengths in this regime is also fitted linearly and we identify the intersection point of the two linear fits with the relaxation time $\tau(\varepsilon)$. This procedure is repeated for all values of ε where at least three data points can be used for each of the linear fits.

The extracted values for τ are shown in the right panel of Figure 5.8. The predicted mean field temporal scaling exponent is given by $\nu z = 1/2$ with the dynamical exponent $z = 1$. However, this prediction is valid only close to the critical point as the square root scaling of the energy gap $g = \hbar\sqrt{\Omega(\Omega - \Omega_c)}$ changes to a linear behavior as the distance from the critical point increases. The experimental data agrees with the prediction based on the energy gap and deviates from the power law scaling with increasing ε as indicated in Figure 5.8. However, the power law scaling remains within the uncertainty of the experimental data.

Another method to visualize the spatial and temporal power law scaling of the spin correlations is to directly compare the observed correlation functions at different hold times and ε. This method does not require a reduction of the full information contained in the correlation function to a single number ξ_c. When rescaling space and time with the predicted power law, the correlation functions

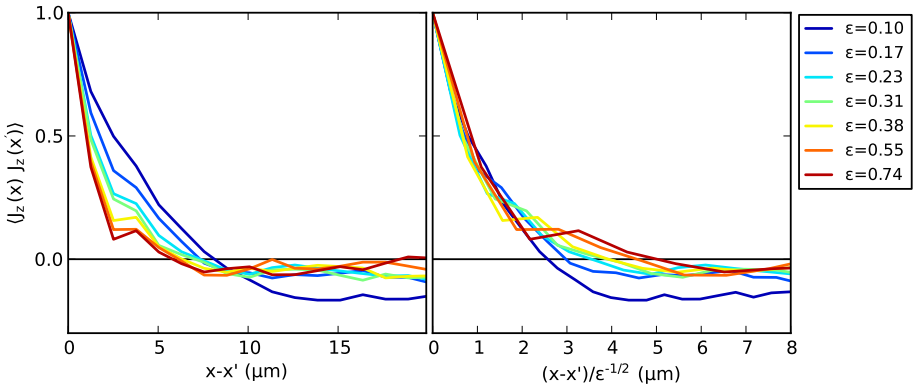

Figure 5.9.: Rescaling of the correlation functions. The measured spin correlation functions at the relaxation time $t = \tau(\varepsilon)$ are plotted in the left panel. The overlap of the correlation functions increases significantly after rescaling the spatial coordinate with the predicted power law behavior, which indicates a collapse of the correlation functions to a single curve. However, deviations at large displacements remain significant.

are predicted to collapse to a single function [94]. For each value of ε we plot the correlation function at the relaxation time $t = \tau(\varepsilon)$ in the left panel of Figure 5.9. In a second step we normalize the spatial coordinate of the correlation functions by the predicted power law scaling $\varepsilon^{-1/2}$. The resulting correlation functions collapse to a common curve for small displacements, but a deviation remains on larger length scales.

In order to understand the experimental observations we[2] model the spin correlations using the mean field Bogoliubov excitation spectra. For the coherent state immediately after the initial $\pi/2$-pulse we assume a population of the excited modes given by the equipartition theorem at high temperatures. The spectrum of the spin fluctuations in k space at thermal equilibrium configuration can be calculated by employing the equipartition theorem. The convolution theorem allows to obtain the spin correlation function in real space from the mode populations in momentum space via Fourier transformation. The resulting correlation function is an exponential with a characteristic length scale $\propto \sqrt{\Omega - \Omega_c}$, which confirms the mean field power law scaling of the correlation length near the critical point.

A quench in ε projects the initial equal population of the spin excitation modes onto the new basis given by the excitation spectrum $\omega_\varepsilon(k)$ for the configuration after the quench. In the subsequent time evolution each mode k evolves with its characteristic frequency $\omega_\varepsilon(k)$ and the spin excitations de-phase. The resulting correlation functions and the evolution of the correlation length determined from an exponential fit are compared to the experimental observations in Figure 5.10. The initial growth of the correlation length is well modeled by the mean field theory. However, the theory predicts oscillations in the correlation length that are not observed in the experiment. This deviation might be caused by the population of transverse excitation modes as the atomic cloud is not strictly one-dimensional, effects of atom loss or beyond-mean field corrections.

[2]The credit for these ideas and calculations goes to Isabelle Bouchoule.

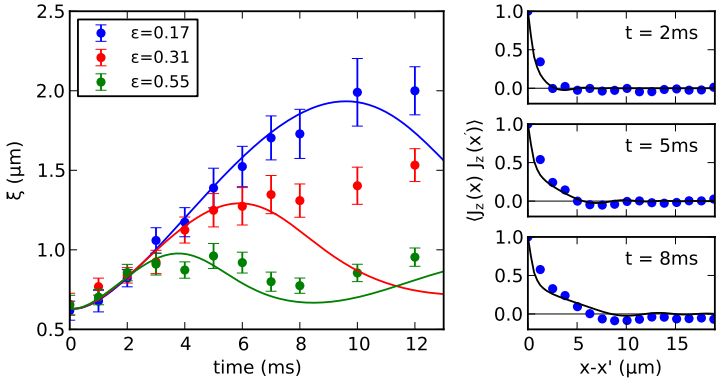

Figure 5.10.: Comparison of the observed correlation functions and time evolution of the correlation length to the mean field prediction. (right) The observed correlation functions (blue circles) are compared to the mean field prediction (solid lines) for $\varepsilon = 0.17$ at various hold times. (left) The measured and predicted time evolution of the correlation length is compared. The predicted oscillations in the correlation length are not observed experimentally.

5.3.2. Scaling in immiscible regime

After discussing quenches to the miscible side of the phase transition, we now focus on quenches through the critical point into the immiscible regime at $\Omega < \Omega_c$[3]. As in the miscible case, the mean field linear response of the system to a quench is given by the Bogoliubov spectrum of the spin excitations. However, for $\Omega < \Omega_c$ the dynamics is dominated by modulational instabilities of the spatial superposition of the two components. The growth rate of the unstable modes is given by the imaginary part of the excitation spectrum.

Before presenting the experimental observations on the emergence of spin domains we recall the discussion of the imaginary part of the excitation spectrum in the context of Figure 2.11. We have seen that the region of unstable modes is shifted towards larger wave vectors with a square-root scaling as Ω is decreased. This square-root corresponds to the value of the critical exponent $\nu = 1/2$.

A quantity that is accessible experimentally is the typical size of the domains in the emerging spin pattern as it is given by the strongest mode in the Fourier spectrum of the spin profile. The domain size corresponds to the most unstable mode in the Bogoliubov spectrum. The discussion of the instability diagram revealed that the most unstable mode deviates from $k = 0$ as $\Omega < \Omega_c/2$. Thus, the domain size will diverge at $\Omega_c/2$ instead of Ω_c. The quantity diverging at Ω_c is the largest unstable mode in the system. It can be associated to the smallest structure present in the observed spin profiles, which is difficult to determine due to detection noise. However, as the width of the instability region in Ω is constant, the domain size is governed by the same scaling exponent as the largest unstable mode.

We perform quenches into the immiscible regime by employing the same experimental sequence as in the previous section. However, the amplitude of the linear coupling is reduced below the critical value after the initial $\pi/2$-pulse. In order to increase the dynamical range for the scaling of the characteristic length we also quench to negative values of Ω. Negative values of Ω are realized by

[3]Note that we consider only sudden quenches through the critical point, such that dynamical effects depending on the quench rate through the critical point can be ignored. The resulting spin dynamics is determined only from the state before the quench and the system parameters after the quench [95].

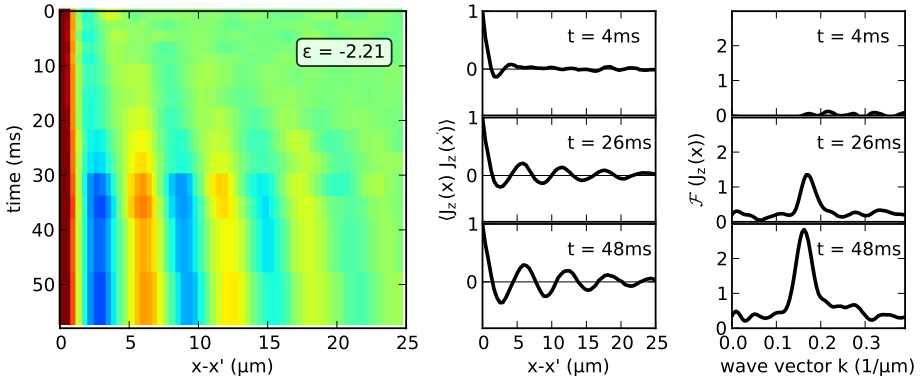

Figure 5.11.: Dynamics of spin correlations after a sudden quench to an exemplary value of ε on the immiscible side of the phase transition. (middle panel) The autocorrelation function of the spin profile shows oscillatory behavior with a decaying amplitude. The oscillations period corresponds to the typical size of the spin domains and marks a characteristic length scale. The right panel shows the corresponding Fourier spectra. (left panel) Time evolution of the correlation functions in false color showing the growth of the oscillation amplitude with time.

changing the phase of the radio frequency radiation by π compared to the configuration at positive Ω. This corresponds to a phase shift $\Delta\varphi = 3\pi/2$ instead of $\pi/2$ after the initial superposition pulse as discussed in section 2.5. These experiments are performed at $B = 9.07\,\mathrm{G}$, where we expect a critical coupling strength of $\Omega_c \approx 50\,\mathrm{Hz}$.

Exemplary correlation functions and Fourier spectra along with their dependence on the hold time after the quench are depicted in Figure 5.11. The unstable excitation modes cause the growth of a periodic spin pattern, which manifests itself in oscillations in the autocorrelation function of the spin profile. The periodicity of the oscillations corresponds to the typical size of the spin domains, while the decay of the envelope of the oscillations is a measure for the spectral width of the excitations. These quantities can be equivalently determined from the Fourier spectra of the spin profiles, which are a direct measure for the contribution of an excitation mode with a given wave vector.

We quantify the dynamics in the domain size by averaging the Fourier spectra at each value of ε and hold time t over about 10 to 20 experimental realizations and determining the wavelength corresponding to the mode with the maximum amplitude in the spectrum. The time evolution of the typical domain size is shown in Figure 5.12 for several values of ε. At short evolution times $t < 15\,\mathrm{ms}$ the modulation depth of the spin domains is below 8% and the domain size cannot be detected reliably due to photon shot noise in the imaging process. At longer times the observed domain sizes are almost constant for each value of ε. The remaining drift towards larger wavelengths can be explained by atom loss. The small drift in the domain size with time is not self-evident as the excitation spectrum can be modified by the back-action of the unstable modes onto the excitation spectrum (see the discussion of secondaries in subsection 3.2.4). However, we do not observe any evidence for such effects. The typical size of the domains increases when approaching the critical point.

For a quantitative study of the domain size scaling with the distance from the critical point we average the Fourier spectra for hold times of $20\,\mathrm{ms} < t < 30\,\mathrm{ms}$ and subsequently determine the domain size from the peak in the spectrum. We choose this time range as it offers a good signal-to-noise ratio at a small modulation depth of $10 \ldots 25\%$ ensuring the validity of the linear response

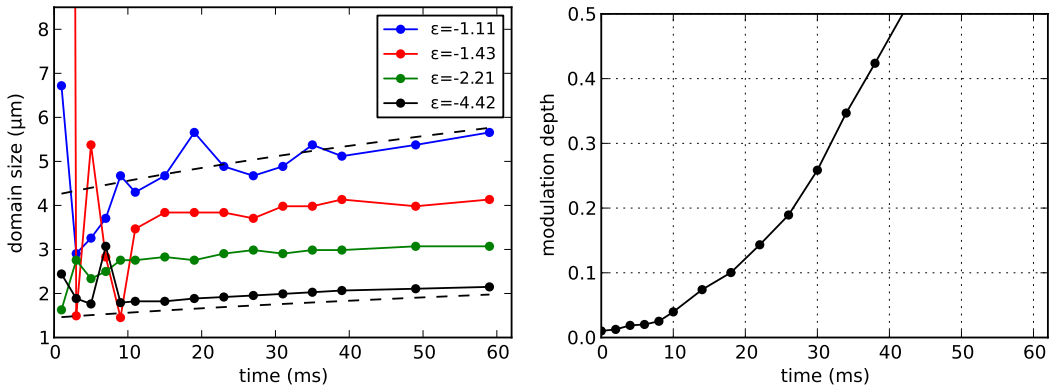

Figure 5.12.: Time evolution of the typical size of the emerging domains at different distances ε from the critical point (left) and the modulation depth of the spin domains (right). At short evolution times $< 15\,\mathrm{ms}$, the modulation in the spin profile is too small ($< 8\%$) to reliably detect the domain size due to the presence of detection noise. At longer times the increase of the domain size when approaching the critical point is visible. At each ε the typical domain size grows slowly in time, which is compatible with the effects of atom loss (dashed lines). The relative change due to atom loss is independent of ε, such that it does not affect the scaling behavior (see Figure 5.19).

approximation[4]. The resulting scaling of the domain size with ε is plotted in Figure 5.13. The linearity of the experimental data points in a double logarithmic plot reveals a power-law scaling in a dynamic range of more than one order of magnitude in ε. A fit yields a scaling exponent of $\nu = 0.49 \pm 0.07$, where the error corresponds to two standard deviations. This result is in good agreement with the predicted mean field exponent of $\nu = 1/2$.

The divergence point for the domain size scaling is $\Omega_c/2$, which can be extracted from a power law fit to the experimental data. The resulting value of $\Omega_c/2 = 24.9 \pm 4.5\,\mathrm{Hz}$ is in agreement with the theoretical prediction for our system parameters of $\Omega_c = 52 \pm 3\,\mathrm{Hz}$. The uncertainty in the predictions is given by the accuracy of the determination of the inter-species scattering length a_{12}.

The length scale diverging at Ω_c is the largest unstable wave vector in the excitation spectrum, which is difficult to obtain from the Fourier spectra due to detection noise. We determine an approximate value as follows: As a first step we determine the full width at half maximum (FWHM) of the peak in the Fourier spectrum. Then we associate the largest unstable wave vector with the mode that is shifted by one FWHM from the position of the peak. The results are summarized in Figure 5.14 confirm the previously obtained values for the scaling exponent ν and the critical coupling Ω_c. The value $\Omega_c = 43.9 \pm 15.0\,\mathrm{Hz}$ obtained from a power law fit may be offset from the true value due to the difficulty of determining an estimate for smallest-wavelength unstable mode, but agrees with both the previously obtained value and the theoretical prediction within the experimental uncertainty.

The large range of validity of the power law scaling is remarkable and is due to the fact that we probe the *mean field* scaling behavior. We will now discuss limitations of the dynamic range in our experiments.

In the long wavelength limit our measurement range is limited by the size of the atomic cloud. However, the limitation is not directly given by the size of the domains approaching the system size, but rather the inhomogeneity of the atomic density leading to a spatial dependence of the

[4]However, the scaling of the domain size is constant in time as we will discuss towards the end of this chapter (see Figure 5.19).

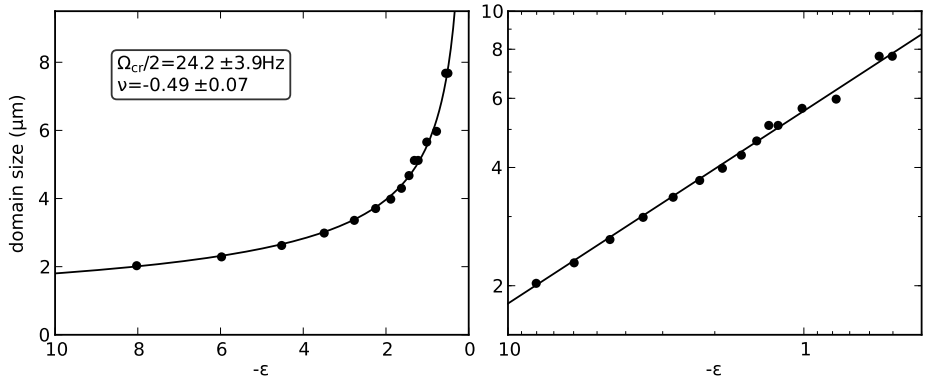

Figure 5.13.: Scaling of the domain size with the distance from the critical point. The data (black circles) is well captured by a power law fit (solid line), also shown by the linearity in a double logarithmic plot (right panel). The extracted scaling exponent agrees with the predicted value of $\nu = 1/2$. The domain size diverges at $\Omega_c/2$, whose value extracted from the fit agrees with the theoretical prediction.

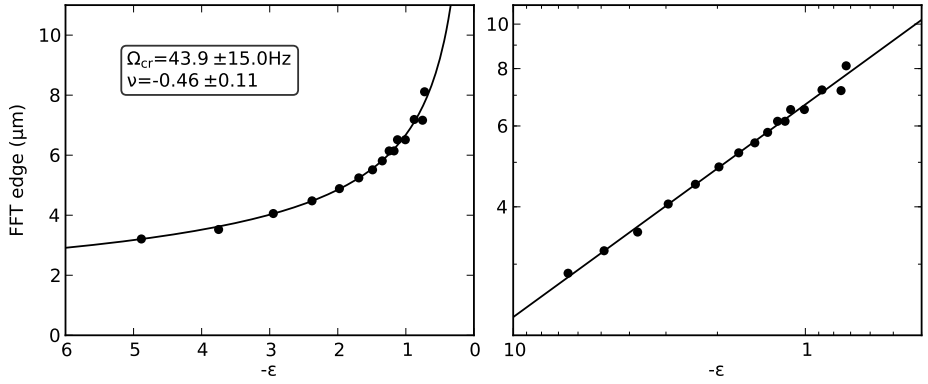

Figure 5.14.: Scaling of the smallest-wavelength unstable mode with the distance from the critical point. The previous results for the scaling exponent and the critical coupling strength are confirmed.

mean field shift (see subsection 3.1.2). For positive Ω the local detuning due to the mean field shift is such that population is transferred to state $|2\rangle$ in the center of the trap, where the density is highest. The smaller atom density at the wings of the trap causes population transfer to state $|1\rangle$. This configuration acts as a seed for the similarly shaped three-domain ground state configuration (see Figure 2.4). For small values of Ω, where the sensitivity to detuning is large, the amplitude of this seed is sufficient such that the three-domain ground state dominates the emerging domain pattern. Numerical integration of the equations of motion confirms that this mode grows faster than other instabilities.

In the small wavelength limit the dynamic range is limited by the optical resolution of our detection system, which is about 1.1 μm in the Rayleigh criterion [75, 26]. As the domain size approaches the imaging resolution the observed modulation depth is reduced due to the convolution of the spin pattern with the point spread function of the imaging system. As the domain size decreases, this effect eventually reduces the amplitude of the observed pattern below the detection noise threshold and prevents a reliable determination of the domain size.

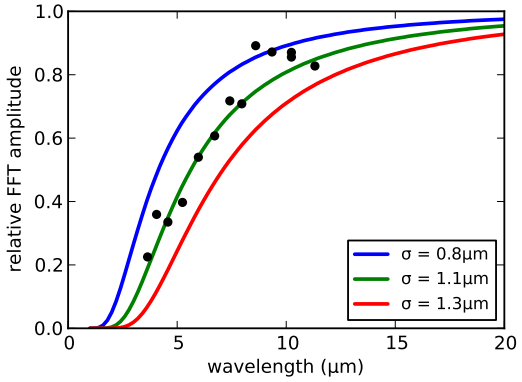

Figure 5.15.: Influence of a finite imaging resolution on the detected modulation depth of sinusoidal structures with different wavelengths. The amplitude of the peak in the Fourier spectra of the spin profiles at different ε decreases for decreasing domain size. The relative change in amplitude (black circles) is compared to the relative modulation depth of a sinusoidal pattern after convolution with a Gaussian of width σ, which models the point spread function the detection optics (solid lines). The good agreement for $\sigma = 1.1$ μm confirms the imaging resolution as a limitation for the detectable dynamic range of the domain sizes.

This effect can be modeled numerically by convolving a sinusoidal oscillation with a Gaussian profile of width σ as an estimate of the point spread function of the imaging optics. The relative amplitude reduction due to convolution can be compared with the observed relative amplitude of the peaks in the Fourier spectra for different domain sizes. The results are summarized in Figure 5.15 and confirm that the decrease in detected modulation depth is compatible with $\sigma = 1.1$ μm.

Within the dynamic range accessible in our experiment, the scaling of the domain size with ε is well described by a power-law with exponent $\nu = 1/2$. This scaling behavior can also be visualized by comparing directly the autocorrelation functions of the spin profiles, where the typical domain size is encoded in the wavelength of the oscillations. Due to the different domain sizes at different ε, the autocorrelation look very different as shown in the left panel of Figure 5.16. After rescaling the spatial coordinate by $\varepsilon^{-1/2}$ the correlation functions collapse to a single oscillation frequency demonstrating the power law scaling. The remaining deviation in the oscillation amplitude stems from the previously discussed finite imaging resolution.

The characteristic time scale in the immiscible regime is the maximum growth rate of the unstable modes. As discussed in section 2.5 it is is constant for $\Omega < \Omega_c/2$. Only for $\Omega_c/2 < \Omega < \Omega_c$ the maximum growth rate decreases when approaching Ω_c. Here, the growth rate of the $k = 0$ mode is given by the modulus of the energy gap $|g(\Omega)|$, which approaches zero like a square-root corresponding to the temporal critical scaling exponent $\nu z = 1/2$. Thus the temporal scaling is imprinted on the growth rate of the $k = 0$ mode, which is difficult to access experimentally due to the previously discussed limitations of in the long wavelength regime of the experiments. This problem can be circumvented by using a tight confinement such that the condensates can be described in the single spatial mode approximation and the gap in the excitation spectrum corresponds the frequency of π-oscillations given by $\omega_\pi = \sqrt{\Omega(\Omega - \Omega_c)}$ (see subsection 2.2.2). However, the square root scaling is only valid close to Ω_c and its observation requires the measurement of oscillation frequencies $\ll \Omega_c$. For our experimental parameters with $\Omega_c \approx 50 \ldots 70$ Hz this corresponds to oscillation frequencies $< 10 \ldots 20$ Hz, which are in the order of the lifetime of atomic cloud of $90 \ldots 30$ ms. As Ω_c and thus the π-oscillation frequency are further reduced by atom loss it is difficult to conduct a

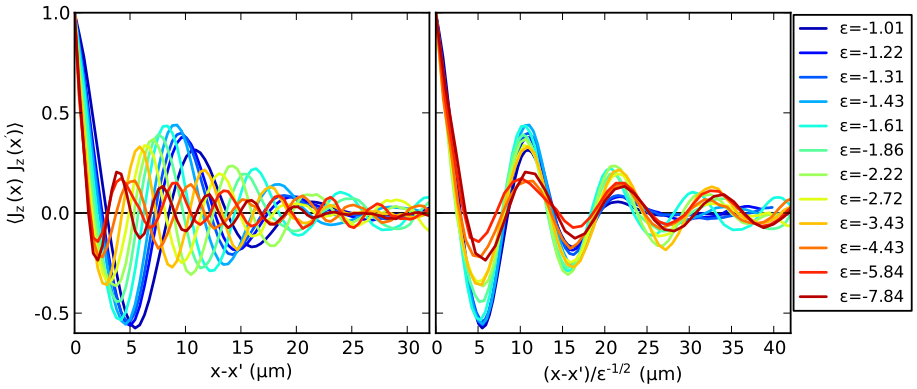

Figure 5.16.: Rescaled correlation functions. The autocorrelation functions of the spin density profile are plotted for different distances from the critical point ε and equal hold times of $t = 35\,\mathrm{ms}$ (left panel). The power law scaling of the domain size becomes apparent by the collapse of the correlation function to a single curve when rescaling the spatial coordinate with $\varepsilon^{-1/2}$ (right panel). The reduced oscillation amplitude for large ε is caused by the finite resolution of our imaging optics (see Figure 5.15).

quantitative analysis of the temporal power law scaling in our experimental system.

On the miscible side of the Feshbach resonance the two components are naturally miscible and there is no phase transition in the ground state of the system. However, the system can be destabilized by a negative linear coupling as discussed in section 2.5. The system becomes unstable for $\Omega < 0$, but the most unstable mode differs from $k = 0$ only for $\Omega < \Omega_c/2$. Here, Ω_c is defined as previously but takes on negative values for miscible scattering parameters. Thus, the detected domain size will have a divergence point at $\Omega_c/2$ as in the previously discussed immiscible case.

We perform quench experiments at $B = 9.11\,\mathrm{G}$ and observe the instabilities induced by the linear coupling field. The scaling of the resulting domain sizes is summarized in Figure 5.17. A power-law fit to the experimental data yields $\Omega_c/2 = -13 \pm 17\,\mathrm{Hz}$, which is compatible with the expected value of $\Omega_c = -45 \pm 3\,\mathrm{Hz}$. The absolute size of the domains is expected to depend only on the distance to the divergence point $(\Omega - \Omega_c/2)^{-1/2}$ and the atomic density $n^{-1/2}$ and should be independent of the scattering parameters of the system and the value of Ω_c. We compare the domain sizes to the previous measurements in the immiscible regime at $B = 9.07\,\mathrm{G}$ in the right panel of Figure 5.17. The good agreement of the measurements performed on the two sides of the Feshbach resonance demonstrates the independence of the domain size from the scattering parameters. For this comparison the 9.11 G data was corrected for a total atom density being about 10% smaller than for the 9.07 G measurements.

The experimental observations on scaling of the unstable excitation modes can be summarized in an instability diagram similar to the theory prediction given in Figure 2.11. The measured Fourier spectra at different values of the coupling strength and both for immiscible and miscible scattering parameters are shown in Figure 5.18.

5.4. Summary, outlook and applications

In conclusion we have realized a miscible-immiscible transition by applying a linear dressing field to interacting binary Bose-Einstein condensates. We have experimentally confirmed the concept of negative linear coupling strengths, which in the strong coupling limit corresponds to the generation of the excited $|-\rangle$ dressed state. In this regime a miscible system can be destabilized and the two

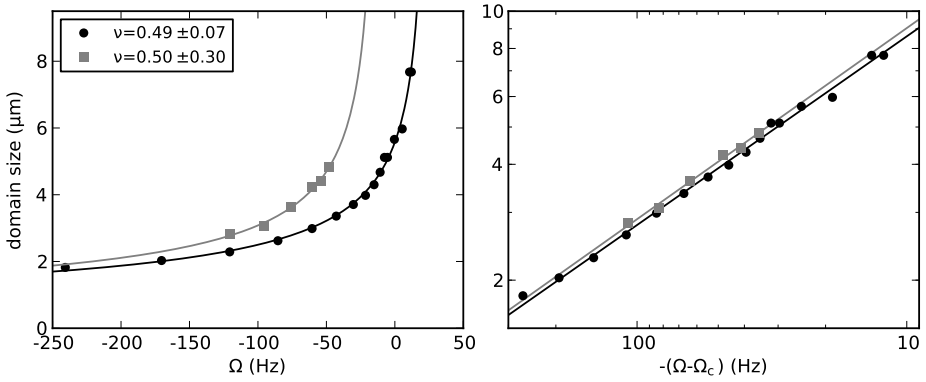

Figure 5.17.: Scaling of the domain size with the distance from the critical point. Both on the immiscible ($B = 9.07\,\mathrm{G}$, black circles) and the miscible ($B = 9.11\,\mathrm{G}$, gray squares) side of the Feshbach resonance, the scaling of the domain size is well modeled by a power law fit. The power law scaling is also shown by the linearity in a double logarithmic plot (right panel). The extracted scaling exponents agree with the predicted value of $\nu = 1/2$. The domain size diverges at $\Omega_c/2$, whose values extracted from the fit agree with the theoretical predictions. The absolute value of the domain size for a given distance $(\Omega - \Omega_c/2)$ from the critical point is independent of the details of the atomic interactions as demonstrated by the small difference in domain sizes at $B = 9.07\,\mathrm{G}$ and $9.11\,\mathrm{G}$ (right panel). The $9.11\,\mathrm{G}$ data was corrected for a 10% smaller total atom density.

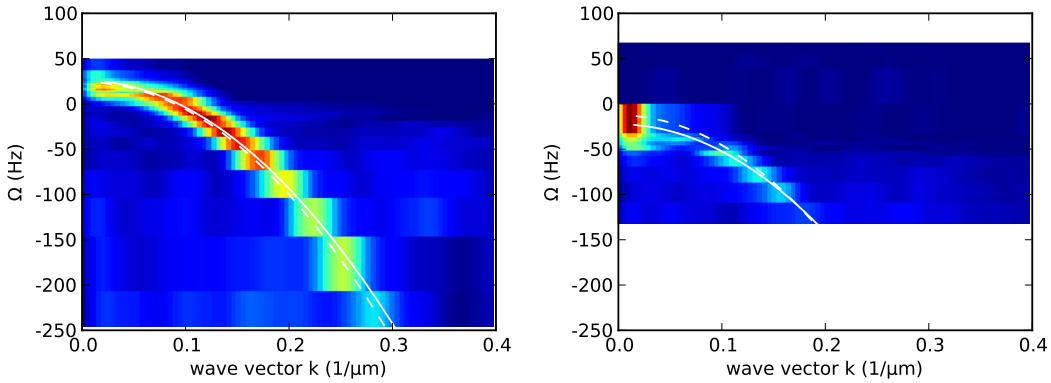

Figure 5.18.: Experimentally observed spectrum of unstable modes versus the linear coupling strength Ω for immiscible ($B = 9.07\,\mathrm{G}$, left) and miscible ($B = 9.11\,\mathrm{G}$, right) scattering parameters. The normalized Fourier spectra of the spin profile after quenches to different values of Ω are shown in false color. The square root scaling of the instability spectrum with Ω is clearly visible. Dashed lines correspond to the power law fits to the experimental data and solid lines denote the Bogoliubov prediction.

components phase separate. Similarly, a linear coupling of positive value (resembling the preparation of the $|+\rangle$ dressed ground state) tunes an immiscible system to miscible when Ω exceeds a critical value Ω_c.

We have investigated the scaling of the characteristic length scales on both sides of the phase transition and found power law scaling in good agreement with theoretical mean field predictions. We

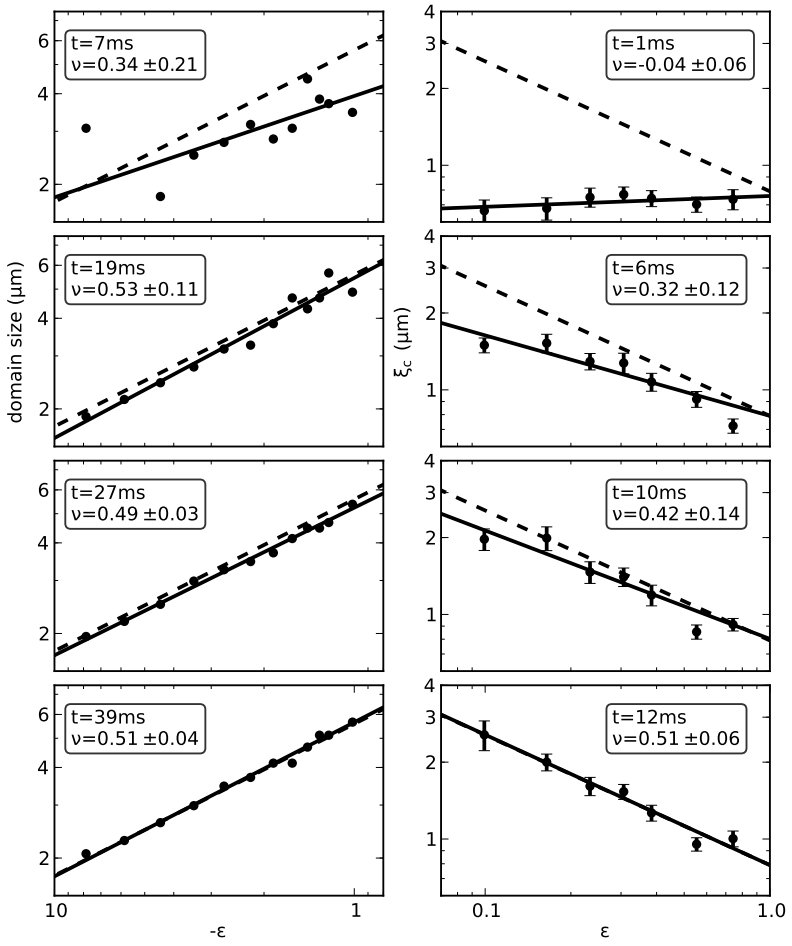

Figure 5.19.: Emergence of the scaling law in the immiscible (left) and miscible regime (right). In the immiscible regime spin domains with a characteristic wavelength grow. This length scale of this spin modulation is immediately imprinted on the spin profile, but can be measured only when the modulation amplitude exceeds detection noise. In the miscible regime the correlation length of the initially uncorrelated system grows with a finite speed. Thus the emerging scaling law is visible first far from the critical point and then propagates towards $\varepsilon = 0$. In contrast to the domain size, the scaling law of the correlation length cannot be detected immediately but requires a growth of the correlations whose duration depends on the value of ε. Solid lines are power law fits to the experimental data (black circles). Dashed lines are the fits taken from Figure 5.13 and Figure 5.7.

will now contrast the emergence of the scaling law on the two sides of the transition as summarized in Figure 5.19.

On the miscible side the spin correlations grow from an initially uncorrelated state after the quench. As the spin correlations propagate with a finite speed, the duration of the growth of the correlation length needs a finite time depending on its saturation value. Thus, the final correlation length ξ_c is proportional to the relaxation time τ as indicated by the dynamical scaling exponent $z = 1$ and the scaling in the correlation length can only be observed after waiting sufficiently long for the correlations to develop.

In contrast the emerging spin domains on the immiscible side are the result of a modulational instability. Initial fluctuations of the spin profile, for example due to shot noise of the prepared coherent state, grow exponentially in a range of wavelengths and the fastest growing mode will dominate the emerging domain pattern. Thus the characteristic length scale, the size of the domains, is determined as soon as the modulation depth of the spin pattern exceeds the initial spin fluctuations. The scaling law can be observed experimentally as soon as the amplitude of the domains exceeds detection noise. The scaling law does not change in time subsequently. As previously explained the temporal scaling can be observed only in the single spatial mode approximation and close to the critical point where $\Omega_c/2 < \Omega < \Omega_c$, which is not accessible in our experiments.

The herewith characterized phase transition offers prospects for further studies. The control parameter Ω can be changed on short timescales faster than microseconds and almost arbitrarily when generating the RF radiation with an arbitrary waveform generator. For example, this system has been proposed [18, 56] as a realization for testing the predictions of the Kibble-Zurek mechanism [96, 97] by ramping the amplitude of the linear coupling through the critical point with various speeds. The feasibility of such schemes with our experimental system and the current status of experiments will be discussed in the next chapter.

6. Dynamics of phase transitions and the Kibble-Zurek mechanism

When studying phase transitions, one usually focuses on the *equilibrium* scalings of physical properties near the critical point of a *homogeneous* system [55, 1]. In the previous chapter, we have seen that the corresponding spatial and dynamical scaling exponents ν and z can also be deduced from the linear response of the system to sudden quenches of the control parameter. The Kibble-Zurek mechanism describes the *dynamics* of phase transitions, for example of a system that is initially in equilibrium and subsequently ramped through a critical point with a finite speed. This chapter explains the general ideas behind the Kibble-Zurek mechanism and a possible implementation of its quantum version employing the miscible-immiscible phase transition discussed in the previous chapter. We will summarize the status of the experiments and the feasibility and challenges for the observation of the Kibble-Zurek mechanism in our experimental setup.

The dynamics of phase transitions was first discussed in the context of the early universe. After the successful unification of weak and electromagnetic interactions involving a spontaneously broken gauge symmetry, Tom Kibble suggested in 1976 that the universe has undergone a series of phase transitions in its early phase after the big bang as the temperature decreased [98, 96]. He argued that space-like separated points independently choose their symmetry broken states. Thus causality, i.e. the speed of light, limits the size of the domains over which the choice of the symmetry broken state is propagated. Kibble discussed the resulting topological structures in the early universe that may have survived and triggered the formation of structures still visible today (see [99] for a review from Kibble's perspective).

Kibble's ideas have been generalized and applied to laboratory-scale systems by Wojciech Zurek in 1985. He associated cosmological strings with vortex lines in superfluids that spontaneously form for example after a pressure quench in ^{4}He [97]. The spontaneous formation of vortices was predicted to cause a measurable macroscopic rotation of superfluid Helium in an annular geometry after the transition to superfluidity. Zurek calculated the dependence of the mean velocity on the rate at which the temperature is quenched through the normal to superfluid transition.

A general model was developed that predicts the number of topological defects after finite-time quenches through the critical point of a second order thermodynamic phase transition. The scaling of the number of defects, or equivalently their size, with the speed of the quench is the main prediction of the Kibble-Zurek mechanism. This concept has been applied to systems ranging from low temperature Bose-Einstein condensates to the energy scales of grand unification in cosmology. A review by Zurek is found in [100].

The Kibble-Zurek mechanism has been tested both numerically and experimentally for second order classical phase transitions in various experimental system ranging from liquid crystals [101, 102] to annular Josephson junctions [103, 104] and nonlinear optical systems [105]. The ^{4}He experiment originally proposed by Zurek was initially reported to be conducted successfully [106], but the results had to be retracted [107] concluding that the vortex production in the experiment is at least two orders of magnitude lower than predicted by the Kibble-Zurek mechanism. However, similar experiments were successfully performed in ^{3}He [108, 109]. In the context of cold atomic gases the formation of defects after reaching degeneracy has been predicted. The production of vortices

was observed experimentally [7, 110] in three-dimensional atomic clouds. The formation of solitons in one-dimensional systems has been predicted [111, 112] and is currently under experimental investigation.

The ideas of the Kibble-Zurek mechanism have been expanded from second order classical phase transitions to quantum phase transitions and were found to be compatible with the Landau-Zener model [113]. The prediction of the Kibble-Zurek mechanism agrees with analytical solutions of the quantum Ising model [114, 115].

Symmetry breaking at quantum phase transitions has been observed in antiferromagnetic spinor gases [8, 9], at the Dicke phase transition [11] and in immiscible binary condensates (see [60] and this thesis). Another well characterized quantum phase transition is the Mott-to-superfluid transition [4]. However, observations of the dynamical scaling of the number of defects with the quench rate through the critical point are rare. Experiments quenching from the superfluid to the Mott regime [5] have studied the microscopic atom number statistics across the transition. The inverse quench has been analyzed and found indications of Kibble-Zurek scaling in the "amount of excitation produced during the quench" [116]. Very recently the formation of defects in linear ion chains has been studied [117] and their dependence on the quench rate in the longitudinal trap frequency was observed to follow the predicted power law behavior [118].

6.1. Proposed implementation in binary Bose-Einstein condensates

An experimental scheme recently proposed by Sabbatini et al. allows for the direct observation of scaling in the number of topological defects in binary Bose-Einstein condensates [18, 56]. The employed phase transition is the miscible-immiscible transition discussed in the previous chapter. The proposal is supported by numerical simulations, also including finite-size effects and inhomogeneities. In this section, we discuss this proposal in the context of our experimental parameters and present the basic ideas behind the Kibble-Zurek mechanism along the way.

The proposed experimental system consists of a one-dimensional two-component Bose-Einstein condensate with immiscible interaction parameters. As discussed in the previous chapter the system can be stabilized and become miscible in the presence of a linear coupling field whose strength exceeds a critical value Ω_c. When preparing the system in the miscible regime $\Omega > \Omega_c$ and subsequently ramping Ω below the critical value, the system becomes unstable and spin domains form. In a homogeneous system translational symmetry is spontaneously broken and the position of the domains depends on spin fluctuations acting as a seed for domain formation. Thus, the absolute position of the domains is random. The dependence of the number of defects, i.e. spin domains, on the speed of a quench from $\Omega_i > \Omega_c$ to $\Omega_f < \Omega_c$ can be derived from the following adiabaticity argument.

6.1.1. A criterion for adiabatic quenches

A general property of second order phase transitions is a divergence of both the relaxation time τ and the equilibrium value of the correlation length ξ at the critical point. We derived the mean field scaling of the correlation length in chapter 2 and found a power law scaling with a critical exponent $\nu = 1/2$, i.e. $\xi(\varepsilon) = \xi_0/|\varepsilon^\nu|$. Here $\xi_0 = \xi_s/\sqrt{2}$ is given by the spin healing length ξ_s of the system and $\varepsilon = (\Omega - \Omega_c)/\Omega_c$ denotes the distance from the critical point.

The relaxation time τ is a measure for the duration the system needs to adjust to external changes of the control parameter, in our case Ω. It is given by the inverse of the energy gap in the excitation spectrum $\tau = \hbar/g$. Consistently with a diverging relaxation time the gap must vanish at the critical point.

In our experimental system the gap is given by $g = \hbar\sqrt{\Omega(\Omega - \Omega_c)}$ (see subsection 2.4.3), which shows a square root behavior in the vicinity of Ω_c. Thus, the associated mean field critical exponent is $\nu z = 1/2$ and because $\nu = 1/2$ one can conclude that $z = 1$. The relaxation time close to the critical point scales as $\tau = \tau_0/|\varepsilon|^{\nu z}$ with $\tau_0 = 1/\Omega_c$. It is important to note that this scaling only holds close to the critical point and for $\Omega \gg \Omega_c$ the gap scales linearly. This change in the scaling exponent was indicated in the experimental observations shown in Figure 5.8. For the following review of Zurek's adiabaticity criterion we will assume a power law scaling in the relaxation time and ignore the deviations far from the critical point. However, this effect will be included whenever numerical predictions about the scaling behavior in our experimental system are made.

The experimental sequence initially discussed by Zurek is the following. The system is prepared in equilibrium on the symmetric side of the phase transition at a given distance from the critical point ε_i. Subsequently the control parameter ε is linearly changed to a final value ε_f on the symmetry-broken side of the transition. We denote the duration of the quench with τ_Q.

When the relaxation time $\tau(\varepsilon)$ is smaller than the transition time associated with the quench, the system can adjust adiabatically to the external change and remains in the equilibrium configuration corresponding to the instantaneous value of ε. If the time evolution was always adiabatic through the critical point, the system would smoothly change from the miscible ground state to the one of the equivalent immiscible ground state. However, as τ diverges at the critical point the time evolution eventually becomes non-adiabatic and excitations enter the system. The time when the evolution becomes non-adiabatic is called the freezing time $\hat{t}$.

Mathematically, the freezing time can be determined by equating the relaxation time τ with the transition time τ_t given by the relative change of the energy gap due to the quench [28]

$$\tau(\hat{t}) = \tau_t(\hat{t}) \quad \Leftrightarrow \quad \frac{\hbar}{g(\hat{t})} = \frac{g(\hat{t})}{\dot{g}(\hat{t})} \quad \Leftrightarrow \quad g(\hat{t})^2 = \hbar\dot{g}(\hat{t}) \tag{6.1}$$

where the dot indicates the derivative with respect to time. Note that this argument is equivalent to the condition that the equilibrium correlation length ξ grows as fast as the speed of sound given by ξ_0 and τ_0, i.e. $\frac{d\xi}{dt}(\hat{\varepsilon}) = \frac{\xi_0}{2\pi\tau_0}$. In analogy to the freezing time $\hat{t}$ we define the correlation length $\hat{\xi} = \xi(\hat{t})$ and the distance from the critical point $\hat{\varepsilon} = \varepsilon(\hat{t})$ at the instant when the evolution of the system becomes non-adiabatic. This criterion for adiabaticity is illustrated in Figure 6.1.

Equation 6.1 can be solved for the freezing time $\hat{t}$, which allows to calculate the relevant experimental parameters $\hat{\varepsilon}$ and $\hat{\xi}$. Assuming a linear ramp from $\Omega_i = 2\Omega_c$ to $\Omega_f = 0$ with the duration τ_Q we obtain

$$\begin{aligned}
\hat{t} &= \tau_0^{\frac{1}{1+\nu z}} \tau_Q^{\frac{\nu z}{1+\nu z}} \\
\hat{\varepsilon} &= \varepsilon(\hat{t}) = -1 + 2\hat{t}/\tau_Q = -1 + 2\tau_0^{\frac{1}{1+\nu z}} \tau_Q^{\frac{\nu z}{1+\nu z}-1} \\
\hat{\xi} &= \xi(\hat{t}) = \xi_0(\tau_Q/\tau_0)^{\frac{\nu}{1+\nu z}}
\end{aligned} \tag{6.2}$$

The central assumption behind the Kibble-Zurek mechanism is that the correlations are 'frozen' as the evolution becomes non-adiabatic. In particular, the characteristic length scale of the system remains $\hat{\xi}$ throughout the evolution in the non-adiabatic regime. As the system crosses the critical point symmetry is broken and it becomes unstable. The frozen configuration of the correlations acts as a seed for the growth of defects. Causality requires that topological defects are chosen independently in space-like separated areas, i.e. information only propagates with the finite speed of sound of the system. As $\hat{\xi}$ is the only characteristic length scale in the system, it determines the typical size of the emerging defects. Thus, Equation 6.2 predicts a power law scaling of the domain

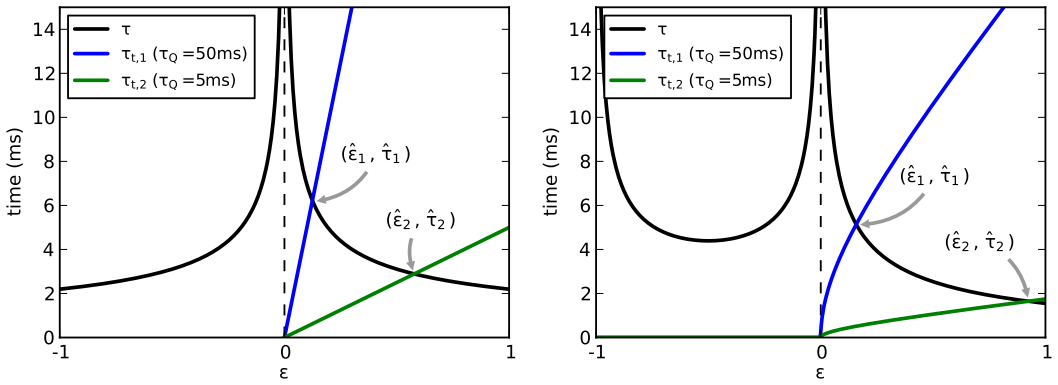

Figure 6.1.: Illustration of the adiabaticity criterion given by Equation 6.1 for quenches through the critical point. The left panel depicts the situation for the power law scaling in the relaxation time $\tau \propto |\varepsilon|^{-\nu z}$, which is valid only close to the critical point. The data shown in the right panel is for $\tau \propto g^{-1}$. Adiabatic evolution is possible if the relaxation time τ (solid black line) is smaller than the transition time, which depends on the duration of the quench (blue and green solid lines). The freezing points $\hat{\varepsilon}$ are depicted.

size with the quench duration. The associated scaling exponent is $\frac{\nu}{1+\nu z}$. For our experimental system with $\nu = 1/2$ and $z = 1$ an exponent of $1/3$ is predicted for the scaling of the domain size with the duration of a linear quench.

The Kibble-Zurek mechanism only predicts a *proportionality* between $\hat{\xi}$ and the resulting defect size. Numerical simulations show that the resulting domain structures are larger than $\hat{\xi}$ by a factor on the order of 10, which depends on the details of the system [114, 111]. By comparing the numerically observed domain sizes [18] with the predictions for $\hat{\xi}$ in the specific case of two linearly coupled atomic clouds we find that the resulting domain size is larger than $\hat{\xi}$ by a factor of 18.2. However, the details for an a priori determination of the value of this proportionality factor are not known.

One aspect of this question is the range of unstable modes in the symmetry-broken regime. It determines which of the seeded excitation modes are unstable and lead to the formation of topological defects. In our experimental system only modes with a wave vector $k < k_c$ are unstable and the value of k_c depends on ε (see subsection 2.4.3). When the evolution of the system becomes adiabatic again after the crossing of the critical point at $\varepsilon(t) = -\hat{\varepsilon}$ [114], the wavelength corresponding to k_c is given by $\lambda_c(-\hat{\varepsilon}) = \sqrt{2}\pi\xi_s|\hat{\varepsilon}|^{-1/2} = 2\pi\hat{\xi}$, which is larger than the frozen correlation length $\hat{\xi}$. Thus, modes with a wavelength given by the frozen correlation length $\hat{\xi}$ will not grow when adiabatic evolution is regained. After the quench has ended at $\varepsilon_f = -1$ ($\Omega_f = 0$), the cut-off is given by $k_c = 1/\xi_s$ and smaller structures can not be observed in the emerging domain pattern. Thus, the validity of the Kibble-Zurek scaling argument can only hold if the proportionality factor between $\hat{\xi}$ and the corresponding defect size is large enough.

In summary, the Kibble-Zurek mechanism predicts the scaling of number of defects (or equivalently their size) with the quench rate through a symmetry breaking phase transition. The argument is based on the transition from adiabatic to non-adiabatic evolution and the assumption that the system's correlations are frozen as soon as the evolution becomes non-adiabatic. Thus, the model requires a Hamiltonian with an energy gap in its excitation spectrum which vanishes at the critical point. If the excitation spectrum of the Hamiltonian does not have an energy gap, long wavelength excitations can enter the system no matter how slow the change in the control parameters is and

adiabatic evolution is not possible.[1]

6.1.2. Numerical simulations and inhomogeneity effects

Finite time quenches through the miscible-immiscible transition of linearly coupled Bose-Einstein condensates have been simulated numerically by Jacopo Sabbatini et al. [18]. In a homogeneous system confined in a ring trap they observed the predicted power-law scaling over two orders of magnitude with an exponent of 0.341 ± 0.006 close to the predicted value of $1/3$. Similar simulations were performed for the experimentally relevant case of an inhomogeneous one-dimensional atomic cloud confined in a harmonic trapping potential. We will now summarize the insights gained from the numerical simulations [18, 56] on the effects caused by inhomogeneities.

The linear density of an atomic cloud confined in a trapping potential is not constant spatially. Several system parameters depend on the atomic density, in particular the critical coupling $\Omega_c \propto n$, but also the correlation length $\xi_0 \propto 1/\sqrt{n}$ and the formation time of spin domains $\tau_f \propto 1/n$. Thus, the reduced density in the outer region of an inhomogeneous atomic cloud leads to a slower growth of larger domains compared to the trap center.

According to simulations the largest effect is the spatial dependence of $\Omega_c(x)$ [18]. The higher density in the center of the trap leads to a larger value of Ω_c. As the coupling strength is reduced during the ramp, the critical point is first crossed in the trap center while the edges of the trap are still on the miscible side of the transition. The front of the phase transition subsequently propagates from the trap center to the outside regions with a lower atom density. This moving front leads to a faster decrease of the number of domains with longer quench times due to:

1. Suppression of domain formation. If the velocity of the moving front is smaller than the local speed of sound in the atomic cloud, information about the choice of the broken symmetry propagates along the front of the phase transition. Domains in different regions are not formed independently but causally connected, which favors the same choice of broken symmetry in the newly unstable regions and thus suppresses domain formation. This effect only affects long quenches and becomes more dominant as τ_Q increases leading to an increased scaling exponent. If the front moves faster that the speed of sound, the defect density is expected to the same as for a homogeneous transition [56]. As estimated in [119] this effect does not affect our experiments. It becomes relevant for ramp times $\tau_Q > 200\,\mathrm{ms}$, which is longer than the life time of the atomic cloud. A detailed discussion of this effect in the context of soliton formation in one-dimensional condensates is found in [111].

2. Increased annihilation of domains after their formation. As the front of the transition moves from the trap center to the edges translational symmetry is broken and the domains have a preferred direction of movement. This causes a larger annihilation rate of the domains compared to the homogeneous phase transition. [18]

These effects lead to an increased scaling exponent of ≈ 0.47 in the simulation of the inhomogeneous system. The two aforementioned effects have been studied independently by further 'numerical experiments' [56]. The suppression of domain formation due to causality can be simulated in a homogeneous atomic cloud with a position-dependent coupling strength $\Omega(x)$, which resembles the spatial dependence $\Omega_c(x)$ of the inhomogeneous system. A similarly increased scaling exponent of 0.497 ± 0.015 was found. The increased domain annihilation was confirmed by simulating the time evolution of seeded domains in an inhomogeneous system.

[1] This is the case when implementing the miscible-immiscible phase transition in Bose-Einstein condensates by changing the atomic interactions, for example with a Feshbach resonance. As discussed in subsection 2.4.3 the excitation spectrum is gapless in the absence of a linear coupling field.

Another consequence of the inhomogeneous density distribution and the resulting variation in Ω_c is a position-dependent quench time. This effective quench time $\tau_Q(x)$ is decreased in the wings of the trap [56], which partly compensates the previously discussed effects and decreases the domain size in the outer regions of the atomic cloud.

The inhomogeneity in the atomic density profile not only causes a spatial dependence of the value of the critical coupling, but also introduces a local detuning of the coupling field caused by the mean field shift (see subsection 3.1.2). In our experiments we tune the frequency of the linear coupling field such that the spatial average of the mean field shift is compensated. Thus atoms in the center of the trap have a detuning of a different sign than atoms in the outer regions of the trap. This detuning creates a corresponding local imbalance during the quench. As we will see in subsection 6.2.2 this effect has important consequences for slow ramps through the critical point.

The configuration in our experiments is such that the density of $|1\rangle$ atoms is increased in the wings of the trap while the center contains more $|2\rangle$ atoms. This acts as a seed for the three-domain ground state of the atomic cloud presented in subsection 2.3.3. For slow ramps, this seed is large enough and the ground state configuration dominates the resulting domain pattern. The formation of smaller domains is suppressed.

Numerical time integration of the equations of motion for our experimental parameters revealed that the three-domain configuration grows faster than any other unstable mode. A numerical Bogoliubov - de Gennes analysis is difficult as the asymmetry $a_{11} \neq a_{22}$ breaks the symmetry of the superposition state prepared by the initial $\pi/2$ pulse. Consequently, this 'background' state is not stationary and the Bogoliubov - de Gennes analysis can not be applied (see subsection B.2.2).

6.1.3. Experimental feasibility

In order to estimate the experimental feasibility of the Kibble-Zurek scheme in our system we calculate the requirements for adiabatic evolution and compare them to the lifetime of the atomic cloud. We assume the same parameters as for the phase transition experiments discussed in section 5.3, i.e. a critical coupling of $\Omega_c \approx 2\pi \times 70\,\mathrm{Hz}$ and a $1/e$ lifetime of about 30 ms.

Using the adiabaticity criterion Equation 6.1 we calculate the maximum rate of change of the control parameter that allows for adiabatic evolution of the system. Due to the divergence of the relaxation time this quench rate depends on ε (and equivalently Ω) as shown in the left panel of Figure 6.2. From this quench rate one can calculate the minimum duration of a ramp starting at Ω that permits adiabatic behavior. The evolution of the system for shorter ramps is never adiabatic.

A further requirement on the ramps is that $\hat{\varepsilon} < 1$, because the system returns to adiabatic behavior at $-\hat{\varepsilon}$ and the ramps stop at $\Omega = 0$ corresponding to $\varepsilon = -1$. This restricts possible experiments to $\hat{\Omega} < 2\Omega_c = 2\pi \times 140\,\mathrm{Hz}$.[2]

Along with the effects of atom loss these requirements restrict the parameter range for experiments to ramps starting at $\Omega_i = 2\pi \times (110 \ldots 140)\,\mathrm{Hz}$ if the duration of the ramp must not exceed the $1/e$-lifetime of the cloud. The largest possible range of ramp durations is $\tau_Q = 15 \ldots 30\,\mathrm{ms}$ at $\Omega_i = 2\pi \times 140\,\mathrm{Hz}$. This small dynamic range does not allow for an experimental observation of a power law scaling in the domain size with the quench rate. Note that these requirements are a lower bound as the effects of atom loss on adiabaticity criterion were neglected. A reduction in the atomic density decreases the speed of sound in the system and thus requires smaller quench rates and longer ramps.

[2] This restriction may be circumvented by extending the ramps to negative values of the coupling strengths as defined in section 2.5.

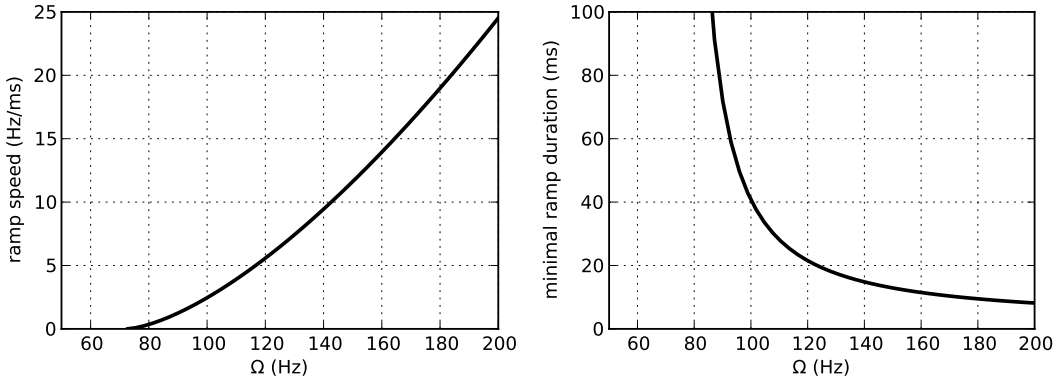

Figure 6.2.: Requirements for adiabatic ramps in our experimental system. (left) The maximum ramp speed allowing for adiabatic evolution is plotted versus Ω. The corresponding minimal duration of ramps starting at $\Omega_i = \Omega$ is shown in the right panel. Faster ramps are never adiabatic.

6.2. Experimental results

As previously discussed the limited tunability of the critical coupling strength (and the corresponding time scales for ramps and the subsequent growth of the domains) in combination with the finite lifetime of the atomic cloud due to atom loss hamper the implementation of the Kibble-Zurek scheme in our experimental setup. However, one can study some aspects of the Kibble-Zurek mechanism using slow ramps towards the critical point or also fast non-adiabatic ramps through the transition. In this section we discuss experimental observations in the context of these modified experimental schemes.

6.2.1. Adiabatic and non-adiabatic ramps towards the critical point

A central element of Zurek's argument is the transition from adiabatic to non-adiabatic behavior when approaching the critical point with a finite speed. We probe this transition by ramping towards the critical point with various ramp speeds and observe the spin correlations during the ramp.

The experimental system and the parameters are identical to the sudden quenches performed on the miscible side of the phase transition discussed in subsection 5.3.1. The experimental sequence is similar to the aforementioned experiments: We create an equal superposition of the two components employing a fast $\pi/2$-pulse, suddenly change the phase of the radio frequency field by $\Delta\varphi = \pi/2$ and simultaneously reduce the amplitude of the field to Ω_i. In contrast to the previous quench experiments we now change the amplitude of the linear coupling during the subsequent evolution and linearly ramp towards the critical point with a fixed slope $\Omega(t) = \Omega_i - \frac{d\Omega}{dt}t$. Atom loss affects relevant system parameters such as the value of Ω_c and we compensate for these effects by adjusting $\Omega(t)$ such that the slope in ε is constant (see subsection 5.3.1) for the details. As previously the values for Ω and $\frac{d\Omega}{dt}$ given in the following text and figures refer to their initial values.

In a first experiment we quench the system to $\Omega_i = 2\pi \times 120\,\mathrm{Hz}$ and subsequently ramp towards the critical point with three different slopes ranging from $\frac{d\Omega}{dt} = 2\pi \times 2.0\,\mathrm{Hz/ms}$ to $2\pi \times 13\,\mathrm{Hz/ms}$. According to Zurek's adiabaticity criterion the slowest ramp is expected to be adiabatic during the time scale of our experiments while the faster ramps are or become non-adiabatic. Note that it is important to include the effect of the changing atom density due to atom loss in this calculation, which is the cause for the deviation from the numbers given in Figure 6.2. As in subsection 5.3.1 we

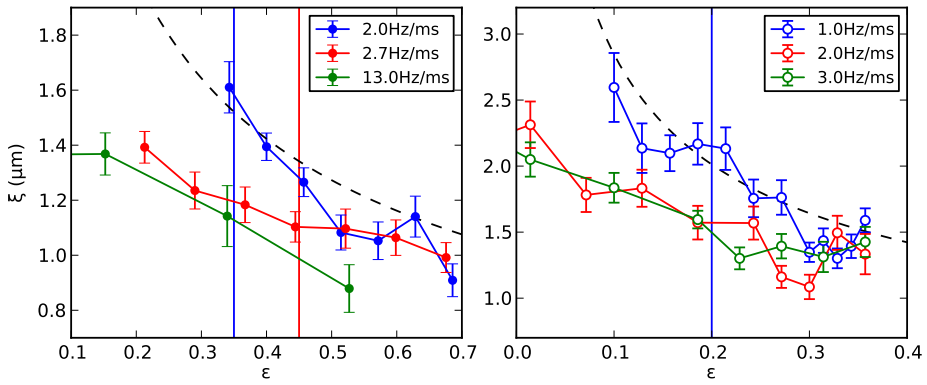

Figure 6.3.: Correlation length versus ε for ramps of different slopes towards the critical point. The slowest ramps are adiabatic, while faster ramps are predicted to become non-adiabatic at $\hat{\varepsilon}$ indicated by the vertical lines. The correlation length at a given value of ε is larger for slow ramps than for fast ramps, which indicates the (non-)adiabaticity. The ramps shown in the left panel started at $\Omega_i = 2\pi \times 120\,\mathrm{Hz}$ and the ones on the right at $\Omega_i = 2\pi \times 95\,\mathrm{Hz}$ after an initial equilibration time of 6 ms. The dashed lines indicate the predicted mean field equilibrium values of the correlation length.

calculate the autocorrelation function of the spin profile and determine the correlation length from an exponential fit. The time evolution of the correlation length during the ramps is shown in the left panel of Figure 6.3

The correlation length of the system is expected to follow the equilibrium configuration for adiabatic ramps. For non-adiabatic ramps the equilibrium correlations grow faster than the system can adjust, which results in correlation lengths smaller than the equilibrium value at the instantaneous value of ε. When adiabatically ramping to a given value of ε we measure a correlation length that is larger than for a non-adiabatic sequence, which indicates the observation of adiabatic and non-adiabatic evolution.

We perform a similar experiment by starting the ramps closer to the critical point at $\Omega_i = 2\pi \times 95\,\mathrm{Hz}$ and reducing the slopes to $\frac{d\Omega}{dt} = 2\pi \times 1.0\,\mathrm{Hz/ms}$ to $2\pi \times 3.0\,\mathrm{Hz/ms}$ such that the slowest ramp remains adiabatic. In order to let the system equilibrate before the ramp we hold it at Ω_i for $t = 6\,\mathrm{ms}$ after the initial quench. The results are summarized in the right panel of Figure 6.3 and show a behavior similar to the previous observations: Slower ramps result in a larger correlation length at a given value of ε.

In order to test the prediction that the system follows the equilibrium configuration during adiabatic ramps we compare the results of the slowest ramps to the saturation values of the correlation lengths after the sudden quenches presented in subsection 5.3.1. As shown in Figure 6.4 the observed absolute value of the correlation lengths and their scaling with ε agree nicely and are close to the theoretical prediction. Note that the saturation value after the quench is not necessarily the equilibrium value and the absence of oscillations in the correlation length remains to be understood (see discussion in subsection 5.3.1). However, the agreement of the different experiments and the consistence with the theoretical prediction provide further indications for observation of adiabatic behavior.

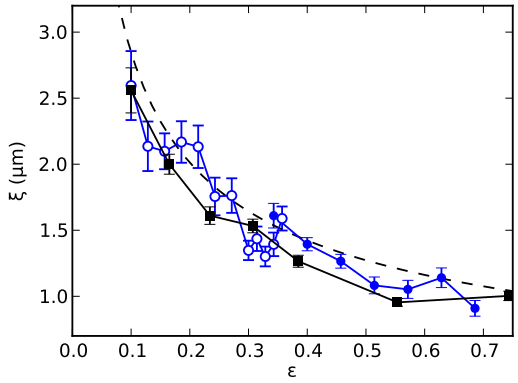

Figure 6.4.: Growth of the correlation length during the adiabatic ramps (blue circles) compared to the saturation values after sudden quenches to a fixed ϵ (black squares; same data as in Figure 5.7). The good agreement of the absolute length scales is a further indication for adiabatic behavior. The dashed line shows the theoretical prediction for the equilibrium correlation length.

6.2.2. Non-adiabatic ramps through the critical point

A central ingredient for Zurek's scaling argument is the transition from adiabatic to non-adiabatic behavior at $\hat{\epsilon}$ as we discussed in the previous section. The size of the resulting topological defects after the quench is proportional to the correlation length $\hat{\xi}$ at this point. However, the value of the proportionality factor and the influence of the system properties in the symmetry-broken regime after the crossing of the critical point remain unclear [114]. It was argued that the size of the defects is actually determined after the critical point was passed and numerical evidence supports this view [120, 56]. While the lifetime of the atomic cloud does not allow for the experimental realization of a wide range of ramps through the critical point with $\hat{\epsilon} < 1$, we can perform faster ramps and study the spin structures emerging due to effects in the symmetry-broken regime. Many observations in the context of these experiments are summarized in [119].

We implement the ramps through the critical point by changing the amplitude of the dressing field from $1.4\Omega_c$ to $0.1\Omega_c$ after the initial $\pi/2$-pulse with ramp durations of $\tau_Q = 1 \ldots 20\,\mathrm{ms}$. The linear coupling field is switched off after the ramp, i.e. $\Omega = 0$. In order to have similar mean atomic densities during the different ramps, shorter ramps with a duration $\tau_Q < 20\,\mathrm{ms}$ are delayed by $\frac{1}{2}(\max(\tau_Q) - \tau_Q)$. During the delay the system is exposed to a strong dressing field with $\Omega = 2\pi \times 340\,\mathrm{Hz}$ such that the overlap of the two clouds remains unchanged and the spin correlation length is small. All hold times are given relative to the initial superposition pulse such that all ramps are centered around $t = \max(\tau_Q)/2 = 10\,\mathrm{ms}$. In this notation the ramps begin and end at different times t depending on τ_Q. This experimental scheme is sketched in Figure 6.5.

We study the spin structures emerging after the crossing of the critical point by analyzing the autocorrelation function and the Fourier spectrum of the spin profile. Their dependence on the ramp duration τ_Q at different hold times t is shown in Figure 6.6. Small spin domains dominate the spectrum after fast quenches $\tau_Q < 9\,\mathrm{ms}$, while large structures emerge after long ramps $\tau_Q > 14\,\mathrm{ms}$. The size of the small domains is given by the most unstable mode in the Bogoliubov spectrum as discussed in the context of the free demixing experiments in subsection 3.2.2.[3] The large structures correspond to the three-domain ground state configuration we also observed when dressing the

[3] In the free evolution experiments the linear coupling is switched off after the $\pi/2$-pulse, which corresponds to a sudden quench with $\tau_Q = 0$.

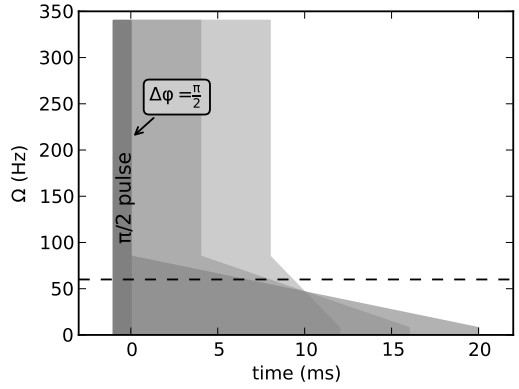

Figure 6.5.: Sketch of the experimental sequence for the ramps through the critical point (dashed line) for three exemplary ramps with durations of 4 ms, 8 ms and 20 ms. The ramps are symmetric around $t = 10$ ms.

system with a weak coupling field with an amplitude near $\Omega \approx \Omega_c/2$ (see subsection 5.3.2). For intermediate durations of the ramp $9\,\text{ms} < \tau_Q < 14\,\text{ms}$ both of these length scales are visible in the Fourier spectrum which has bi-modal characteristics. However, at $\tau_Q = 9$ ms there is a sharp reduction in the contribution of the long-wavelength mode and the large structures do not occur for faster ramps.

We model the spin dynamics during and after the ramps by integrating over the imaginary part of the mean field excitation spectra at each hold time. For $\Omega < \Omega_c$ the excitation spectrum has unstable modes which grow exponentially. The range of unstable modes and their growth rates depend on the value of Ω, which is changed during the ramp. Thus different modes grow during the course of the ramp and their relative amplitude can be calculated by integrating $\int_0^t dt' \exp\{\text{Im}[\omega(k, \Omega(t'))] \cdot t'\}$, where $\Omega(t')$ models the experimental sequence and depends on τ_Q. The results of the numerical integration including the effects of atom loss are shown in the right panel of Figure 6.6. At early hold times it shows a similar crossover of the dominating length scales around $\tau_Q \approx 10$ ms. The size of the small modes agrees well with our observations while the size of the large structures is given by the finite size of the atomic cloud and thus not contained in the homogeneous theory.

When integrating the unstable part of the spectrum for longer times, the short wavelength mode always dominates as it is the fastest growing mode in the absence of a linear coupling after the ramp. However, it is important to remember that the theoretical model is valid only for small modulation depths of the spin structures as the excitation spectrum may change when the density profiles deviates from the equal superposition state. Thus, the validity of this approach breaks down at the hold time t when the modulation depth exceeds a threshold. The sharp change of the spin structures at τ_Q can be understood in this context: If the amplitude of the long-wavelength mode after the ramp is large enough, the subsequent growth of the small domains is suppressed and the long-wavelength mode prevails also for longer times. If this condition is not fulfilled, the growth of the small domains supersedes the large structures. This threshold is passed at $\tau_Q = 9$ ms according to the experimental observations. We estimate this threshold to be a modulation depth of approximately 30%, as this the typical modulation amplitude for $\tau_Q = 9$ ms and $t = 19$ ms.

In summary, we have discussed the classic Kibble-Zurek scenario. It states that the size of topological defects after finite-time quenches through a critical point is proportional to the correlation length at the freezing time. At that instant the relaxation time of the system is larger than the transition time of the quench and the system fails to follow adiabatically. We have observed indications of a transition from adiabatic to non-adiabatic behavior by analyzing the growth of spin correlations

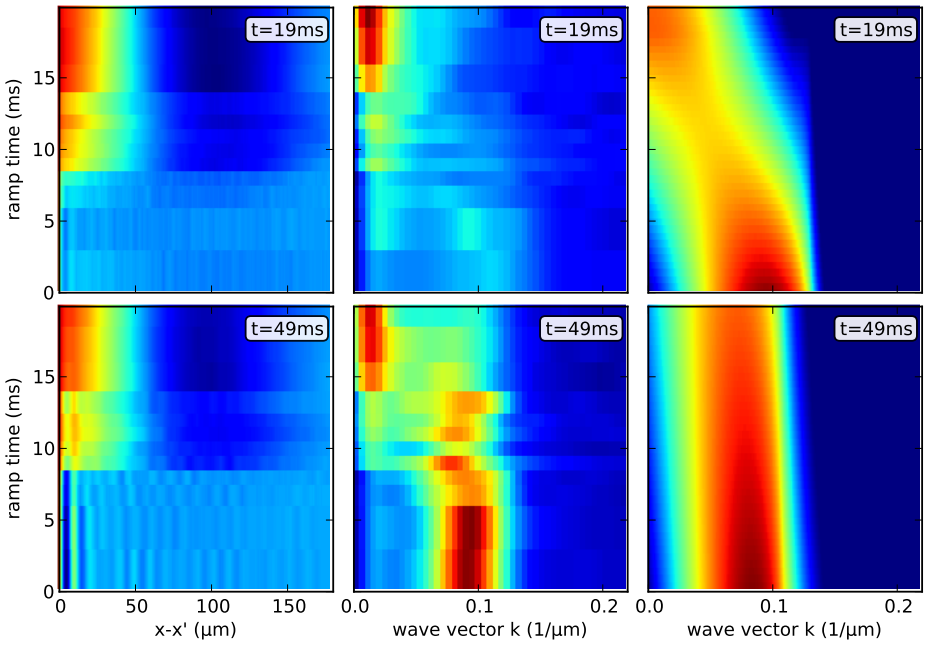

Figure 6.6.: Observed correlation functions (left column) and Fourier spectra (center column) in false color for different ramp durations and hold times after the initial $\pi/2$-pulse. Red color indicates correlations, blue color anti-correlations in the correlation functions. For the Fourier spectra red color means a strong amplitude of the corresponding wave vector and blue color denotes weakly populated modes. The spin pattern is dominated by small structures for $\tau_Q < 9\,\mathrm{ms}$, while large structures prevail for $\tau_Q > 14\,\mathrm{ms}$. The small structures correspond to the most unstable mode for $\Omega = 0\,\mathrm{Hz}$ and the large pattern is given by the three-domain ground state in the trap. Both length scales contribute in the intermediate regime $9\,\mathrm{ms} < \tau_Q < 14\,\mathrm{ms}$. A sharp change in the amplitude of the long-wavelength mode occurs at $\tau_Q = 9\,\mathrm{ms}$. The Bogoliubov prediction for the spectrum of the spin pattern is shown in the right column. The imaginary part of the Bogoliubov spectrum is integrated over the experimental sequence employed in the measurements. It reproduces well the experimentally observed cross-over of length scales at $\tau_Q \approx 10\,\mathrm{ms}$. This model is valid only for small times as it requires a small modulation depth of the spin domains.

for different ramp speeds towards the critical point. In addition, the influence of unstable modes after the crossing of the critical point on the emerging domain pattern was demonstrated.

7. Conclusion and Outlook

In this thesis we have experimentally studied the rich interplay of non-linear interactions and a linear coupling field in a two-component elongated Bose-Einstein condensate, which results in a miscible-immiscible phase transition. We have discussed the properties of the system far away from the transition point, which are dominated by interaction among the atoms in the limit of weak linear coupling. In the opposite limit of a strong coupling field the analog of optical dressed states has been realized in condensates using a non-adiabatic preparation scheme. We have examined the effective interactions between the dressed states by studying the long time dynamics of Rabi oscillations and found their miscibility to be opposite to that of atomic states.

The critical point of the phase transition occurs when the energy scales of the interactions and the linear coupling are equal. We have characterized the phase transition by examining the linear response of the spin correlations after a sudden quench to the proximity of the critical point. A power law divergence has been observed in the characteristic length scale on both sides of the phase transition. The extracted values for the critical exponent ν of 0.49 ± 0.07 and 0.51 ± 0.26 are in good agreement with the mean field prediction of $\nu = 1/2$. The relaxation time on the miscible side of the transition agrees with a prediction based on the energy gap in the excitation spectrum of the binary condensate. Furthermore, we have discussed a scheme for the measurement of dynamical scaling exponents in the context of the Kibble-Zurek mechanism and sketched its experimental feasibility. Indications for the transition from adiabatic to non-adiabatic behavior were observed.

The experimental system presented in this thesis offers a high level of control for the study of quantum phase transitions. As the control parameter is realized by the amplitude of a radio-frequency field, well defined sudden and finite-time quenches can be realized with sub-microsecond resolution. Further experiments can be made possible by the following improvements to the experimental implementation employed in this thesis.

The experimentally accessible time scale for the presented experiments was limited by increased atom loss due to the proximity to the Feshbach resonance. In addition, atom loss modifies relevant system parameters that depend on the atom density such as the critical coupling strength or the spin healing length. While the effect on the critical coupling strength could be compensated by adjusting the amplitude of the linear coupling field, unwanted imperfections remain. This problem can be circumvented by utilizing a different atomic species with naturally immiscible scattering parameters such that the use of a Feshbach resonance can be avoided. A further requirement for the employed states is a small differential sensitivity to external perturbations such as magnetic fields in order to ensure resonance of the linear coupling.

Another limitation of the current experimental setup is the finite longitudinal size of the atomic cloud and the resulting inhomogeneity. This leads to a spatial dependence of the critical coupling strength and restricts the analysis region to the central part of the atomic cloud, which can be treated as locally homogeneous. In addition our atomic cloud is not truly one-dimensional and the first few transverse excited states are populated. The role of transverse excitations in the condensates and their consequences for our observations require further investigation. True one-dimensional confinement has been realized both with atom chips [66, 15] and optical dipole potentials [121]. Such a geometry eliminates possible effects of transverse excitations and reduces effects of cloud inhomogeneities.

We have detected the atomic clouds by in-situ absorption imaging, which is a destructive process and provides only a snapshot of the spin dynamics in each single experimental realization. In many of the performed experiments the dynamics results from spontaneous symmetry breaking and is not shot-to-shot reproducible such that only realization-independent quantities such as average domain sizes could be analyzed. The evolution of a single experimental realization can be followed by employing non-destructive imaging techniques such as phase-contrast imaging [8, 122], which permits further insights on the growth of spin domains and their subsequent dynamics.

Ultracold atoms continue to offer great prospects for the study of quantum phase transitions. Novel schemes for the determination of dynamical scaling exponents have been proposed [94, 16] as alternatives to the classical Kibble-Zurek scenario involving quenches through the critical point. Very recent experiments have explored the dynamics following quenches in one [15] and two-component [60] elongated systems as well as one-dimensional lattices [123]. The divergence and scaling of fluctuations has been studied at a driven-dissipative Dicke phase transition [124] and universal spin dynamics was observed in two-dimensional Fermi gases [125]. This variety of experiments in the recent months provides only a first glimpse of the vast opportunities quantum gases have to offer in this field. Further experimental and theoretical insights about universality, phase transitions and quench dynamics near critical points will continue to push the frontiers of this exciting field of physics.

A. Summary of atomic and experimental parameters

A.1. Properties of ^{87}Rb

For an overview of the atomic properties of ^{87}Rb including optical, magnetic and electronic data we refer to [67]. The interaction and loss parameters that are relevant for our experiments employing states $|1\rangle = |F = 1, m_F = \pm 1\rangle$ and $|2\rangle = |F = 2, m_F = \pm 1\rangle$ are summarized below along with the corresponding references.

A.1.1. Scattering lengths

a_{11}	$100.40\,a_B$	[73, 77]
	$100.44\,a_B$	[78, 79]
a_{22}	$95.00\,a_B$	[77]
	$95.47\,a_B$	[78]
	$95.44(7)\,a_B$	[79]
a_{12}	$97.70\,a_B$	[126]
	$97.66\,a_B$	[77]
	$98.09\,a_B$	[78]
	$98.006(16)\,a_B$	[79]

For scattering properties within the $F = 1$ or $F = 2$ manifold, see [127].

A.1.2. Loss coefficients

For the loss coefficients we use the notation KN_{ijk}, where N denotes the number of particles involved in the inelastic collision process and $i, j, k \in \{1, 2\}$ are the states of the involved atoms.

$K1$	typically $0.05 \ldots 1\,/\mathrm{s}$	
$K2_{11}$	$0\,\mathrm{cm}^3/\mathrm{s}$	[77, 74]
	$< 1.6 \times 10^{-16}\,\mathrm{cm}^3/\mathrm{s}$	[128]
$K2_{22}$	$11.94(19) \times 10^{-14}\,\mathrm{cm}^3/\mathrm{s}$	[77]
	$10.4 \times 10^{-14}\,\mathrm{cm}^3/\mathrm{s}$	[74]
	$8.1(3) \times 10^{-14}\,\mathrm{cm}^3/\mathrm{s}$	[79]
$K2_{12}$	$7.80(19) \times 10^{-14}\,\mathrm{cm}^3/\mathrm{s}$	[77]
	$5 \times 10^{-14}\,\mathrm{cm}^3/\mathrm{s}$	[74]
	$1.51(18) \times 10^{-14}\,\mathrm{cm}^3/\mathrm{s}$	[79]
$K3_{111}$	$5.8(1.9) \times 10^{-30}\,\mathrm{cm}^6/\mathrm{s}$	[128]
$K3_{222}$	$18(5) \times 10^{-30}\,\mathrm{cm}^6/\mathrm{s}$	[129]

Also see [130] for a discussion of inelastic collisions in the $F = 2$ manifold.

A.1.3. Scattering lengths near the Feshbach resonance

B [G]	9.03	9.05	9.06	9.07	9.08	9.11	9.17
a_{12} $[a_B]$	100.3	102.6	105.6	112.9	120	84	94.0

Also see Figure 3.4 for a graphical summary.

A.2. Imaging

amplification	30.96
CCD pixel size	13 µm
pixel size in object space	420 nm
image width	512 px, 215 µm
image height	140 px, 59 µm

A.3. Optical dipole traps

A.3.1. Charger

For measurements near Feshbach resonance

transverse trap frequency $\omega_\perp$	$2\pi \times 460$ Hz
longitudinal trap frequency ω_x	$2\pi \times 22.0$ Hz

For measurements at the 'magic field' of 3.23 G

transverse trap frequency $\omega_\perp$	$2\pi \times 490$ Hz
longitudinal trap frequency ω_x	$2\pi \times 23.4$ Hz

A.3.2. Waveguide

transverse trap frequency $\omega_\perp$	$2\pi \times 128$ Hz
longitudinal trap frequency ω_x	$2\pi \times 1.9$ Hz

Parameters of the atomic cloud

typical linear atom density	230 atoms/µm
minimum spin healing length at 9.08 G	1.3 µm

B. Numerical methods for simulating Bose-Einstein condensates

This appendix summarizes the theoretical background for numerical simulations of one-dimensional trapped two-component Bose-Einstein condensates in the presence of a linear coupling between them. First, we will outline the underlying equation of motion, the Gross-Pitaevskii equation, and its variants for quasi one-dimensional geometries. The second part covers numerical methods for calculating the ground state, Bogoliubov excitations and time dynamics of Bose condensates.

For simplicity, all theoretical and numerical methods will be discussed in the context of a one-dimensional single species condensate. The generalization to higher dimensions with more components (possibly with a linear coupling between them) will be outlined only where qualitatively different problems arise.

B.1. Gross-Pitaevskii equation

In the mean field approximation, Bose-Einstein condensates at zero temperature, i.e. neglecting thermal excitations, can be described by the Gross-Pitaevskii equation (GPE) [29, 30]

$$i\hbar\frac{\partial\psi}{\partial t} = \left[-\frac{\hbar^2}{2m}\nabla^2 + V + g|\psi|^2\right]\psi \tag{B.1}$$

where $2\pi\hbar$ is Planck's constant, m the atomic mass and $V = V(x, y, z)$ the external trapping potential. $g = \frac{4\pi\hbar^2 a_s}{m}$ quantifies interatomic interactions, parametrized by the s-wave scattering length a_s.

This equation models the temporal and spatial dynamics of the three-dimensional wave function, $\psi = \psi(x, y, z, t)$, which is normalized to the number of atoms N in the condensate, $N = \int |\psi|^2 \mathrm{d}V$. For many trapping geometries, such as a spherical or cylindrical confinement, Equation B.1 can be reduced to lower dimensions in order to simplify analytic calculations and decrease computational complexity.

B.1.1. One-dimensional Gross-Pitaevskii equation

For cylindrical trapping geometries, where the transverse confinement is much stronger than the longitudinal one, the condensate can be described by a one-dimensional wave function. This is achieved by splitting the three-dimensional wave function into a longitudinal and a transversal part, $\psi = \psi_{1\mathrm{D}}(x, t) \cdot \psi_\perp(y, z)$. Assuming a transversal profile of Gaussian shape with width $\sigma = a_\perp$ and integrating out the transverse dimensions, one yields a one-dimensional Gross-Pitaevskii equation (1D GPE) with an effective interaction parameter $g' = g/(2\pi a_\perp^2)$ [131]

$$i\hbar\frac{\partial\psi_{1\mathrm{D}}}{\partial t} = \left[-\frac{\hbar^2}{2m}\frac{\partial^2}{\partial x^2} + V + g'|\psi_{1\mathrm{D}}|^2\right]\psi_{1\mathrm{D}} \tag{B.2}$$

Here, $a_\perp = \sqrt{\hbar/m\omega_\perp}$ denotes the transverse harmonic oscillator length and $\omega_\perp$ the corresponding trap frequency.

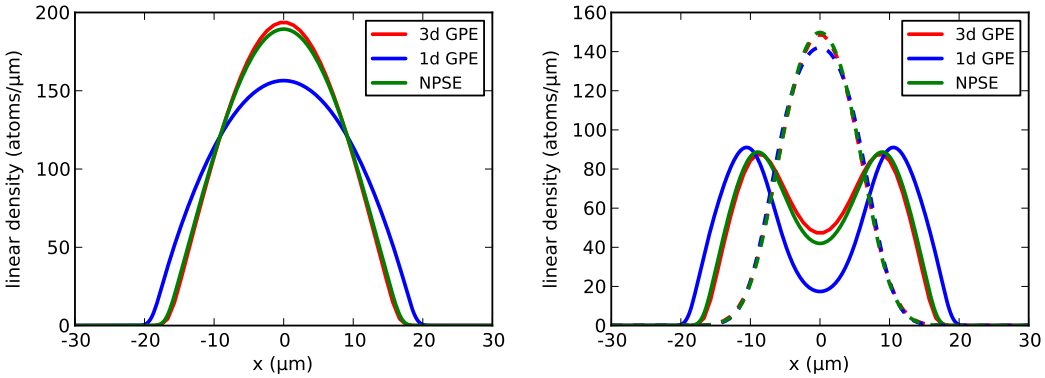

Figure B.1.: Comparison of different approximations to the full 3D Gross-Pitaevskii equation. The ground states of single (left) and two-component (right) condensates containing 4000 atoms in the charger are calculated using the 1D GPE (blue) and the NPSE (green). Comparison to the full three-dimensional solution (red) reveals, that the NPSE results agree well with the exact solution, while the 1D GPE deviates significantly.

The validity of this 1D approximation requires waveguides without longitudinal confinement or a large trapping aspect ratio $\frac{\omega_\perp}{\omega_x} \gg 1$. However, it also depends on the atom density, since the assumption of a transverse Gaussian profile, i.e. being in the transverse ground state, requires the chemical potential to be smaller than the transverse trapping frequency. The general condition for the validity of the 1D GPE is given by the dimensionality parameter [132]

$$\frac{N a_s a_\perp}{a_x^2} \ll 1$$

with the longitudinal harmonic oscillator length a_x. For our experiments performed in the charger ($N = 3000$, $a_s = 100\,a_{\mathrm{bohr}}$, $\omega_x = 23.4\,\mathrm{Hz}$, $\omega_\perp = 490\,\mathrm{Hz}$), this dimensionality parameter is 1.6 and for the measurements in the waveguide ($N = 50000$, $a_s = 100\,a_{\mathrm{bohr}}$, $\omega_x = 1.9\,\mathrm{Hz}$, $\omega_\perp = 128\,\mathrm{Hz}$) even 4.1. Thus, the one-dimensional Gross-Pitaevskii equation is not an adequate description of our system.

B.1.2. Nonpolynomial nonlinear Schrödinger equation

Our cigar-shaped Bose-Einstein condensate is better described by the nonpolynomial nonlinear Schrödinger Equation (NPSE), which assumes a Gaussian transverse profile as well, but allows its width to vary along the longitudinal trap axis, $\sigma = \sigma(x)$. Integration over the transverse coordinates yields [133]

$$i\hbar\frac{\partial\psi_{1\mathrm{D}}}{\partial t} = \left[-\frac{\hbar^2}{2m}\frac{\partial^2}{\partial x^2} + V + \frac{g|\psi_{1\mathrm{D}}|^2}{2\pi a_\perp^2}\frac{1}{\sigma^2/a_\perp^2} + \frac{\hbar\omega_\perp}{2}\left(\frac{1}{\sigma^2/a_\perp^2} + \sigma^2/a_\perp^2\right)\right]\psi_{1\mathrm{D}}$$

where $\sigma^2 = a_\perp^2\sqrt{1 + 2a_s|\psi_{1\mathrm{D}}|^2}$. The last term is not a constant offset term (which could be ignored), but has an implicit spatial dependence through σ.

Note that in the limit of weak interactions, $a_s|\psi_{1\mathrm{D}}|^2 \ll 1$, the NPSE reduces to the 1D GPE, $\sigma \approx a_\perp$. Our experimental parameters mentioned above yield $a_s|\psi_{1\mathrm{D}}|^2 \approx 0.8$. Thus the NPSE is a more appropriate description of our system as demonstrated in Figure B.1, which compares the

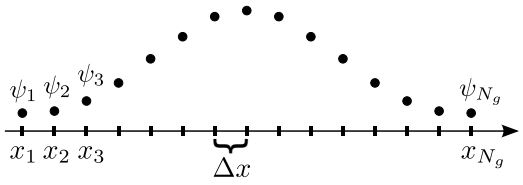

Figure B.2.: Schematic representation of the discretization of the wave function on a spatial grid. The continuous function is mapped onto a vector with N_g elements.

ground states of the condensate calculated by the 1D GPE, NPSE and the full 3D GPE.

The extension of the NPSE to binary condensates is non-trivial and we will not give the results here but refer to [134]. Note that for simulations of the time evolution including atom loss, the loss coefficients have to be modified in a similar manner as the interaction parameters when employing the NPSE instead of the 3D GPE.

B.2. Numerical methods

The Gross-Pitaevskii equation and its variants can be solved analytically only for a few special cases, e.g. in the limit of no interactions or in the limit of strong interactions (Thomas-Fermi regime). In general, solutions have to be found numerically. This section describes numerical methods for computing stationary states as well as Bogoliubov excitations and time dynamics of the Gross-Pitaevskii equation. It is based on personal communication with Panayotis Kevrekidis[1] during October 2010.

All numerical methods presented here require a discretization of continuous functions (e.g. the wave function or the potential) on a spatial grid as outlined in Figure B.2. For a spatial grid consisting of N_g grid points, the wave function ψ is represented by a vector of size N_g, whereas the Hamiltonian takes the form of an $N_g \times N_g$ matrix. The distance Δx between two grid points has to be smaller than the smallest features one expects to observe in the simulated wave function.

Similarly, the state of two components can be represented by a vector of size $2N_g$, where the first N_g elements correspond to the wave function of the first component and the other entries describe the second component.

B.2.1. Computing the ground state

The starting point of numerical simulations is calculating the ground state (or more generally, a stationary state) of the system, as this usually is the initial experimental state after Bose-Einstein condensation. Factoring out the time evolution in Equation B.1, $\psi(x,t) = e^{-i\mu t}\phi(x)$, one yields the equation modeling stationary states

$$\mu\phi = \left[-\frac{\hbar^2}{2m}\frac{\partial^2}{\partial x^2} + V + g|\phi|^2\right]\phi \tag{B.3}$$

with the chemical potential μ.

This section outlines two methods for computing the ground state of the system: Imaginary time propagation (ITP) and Newton's method for finding the roots of a function. While the former is restricted to finding the state of minimal energy, the latter method can converge to any stationary state.

[1]Homepage: `http://www.math.umass.edu/~kevrekid/`

Both methods are of iterative nature, i.e. they asymptotically approach the desired stationary state in discrete steps. This requires both a sensible initial guess of the wave function, for example a Thomas-Fermi or a Gaussian profile, and a break condition for terminating the iteration, such as a lower bound for the relative change of the wave function in one iteration step.

Imaginary time propagation

The time evolution of the wave function $\psi(x,t)$ under the Hamiltonian $\hat{H}$ is calculated using the propagator $e^{-i\hat{H}\Delta t/\hbar}$,

$$\psi(x,t+\Delta t) = e^{-i\hat{H}\Delta t/\hbar}\psi(x,t) \tag{B.4}$$

Any wave function can be expressed as a superposition of energy eigenstates ϕ_m with time-dependent amplitudes, $\psi(x,t) = \sum_m a_m(t)\phi_m(x)$. When rewriting Equation B.4 in this basis and replacing $\Delta t \to -i\Delta t$, the amplitudes of the basis states decay exponentially with a decay constant given by the corresponding energy eigenvalue,

$$\psi(x,t+i\Delta t) = \sum_m a_m(t)e^{-E_m\Delta t/\hbar}\phi_m(x)$$

Since the eigenstate with the lowest energy decays slowest, iteratively performing propagation steps in imaginary time yields the ground state of the system. Note that this operation is not unitary and thus requires renormalization of the wave function after each iteration step.

On a spatial grid, the determination of the propagator corresponds to the calculation of the matrix exponential $e^{-i\hat{H}\Delta t/\hbar} = e^{-i(\hat{H}_\mathrm{p}+\hat{H}_\mathrm{x})\Delta t/\hbar}$, where $\hat{H}_\mathrm{p}$ is the kinetic energy Hamiltonian. The potential and interaction term $\hat{H}_\mathrm{x}$ is diagonal and its matrix exponential can be easily computed.

The kinetic energy contribution is calculated more conveniently in momentum space, where $\hat{H}_\mathrm{p}$ is diagonal, but which requires a Fourier transformation of the wave function. Thus, one can split one propagation step into three successive steps in position and momentum space as proposed in [135],

$$\psi(x,t+\Delta t) = e^{-i(\hat{H}_\mathrm{p}+\hat{H}_\mathrm{x})\Delta t/\hbar}\psi(x,t) \approx e^{-i\hat{H}_\mathrm{p}\Delta t/2\hbar}e^{-i\hat{H}_\mathrm{x}\Delta t/\hbar}e^{-i\hat{H}_\mathrm{p}\Delta t/2\hbar}\psi(x,t)$$

This so-called 'split-step fast Fourier transform method' makes use of the Baker-Campbell-Hausdorff formula, which is only exact for commuting operators $\hat{H}_\mathrm{p}$ and $\hat{H}_\mathrm{x}$. However, the operators for kinetic and potential energy do not commute, which leads to an error $\mathcal{O}[(\Delta t)^3]$. Thus, this methods requires small steps in (imaginary) time in order to avoid the accumulation of numerical errors [135, 136].

In summary, the method of imaginary time propagation has the advantage of reliably converging towards the ground state without the requirement of a good initial guess of the ground state wave function. However, due to the diffusive nature of the equation, its convergence towards the steady state is slow and requires many iterations as shown in Figure B.3.

Newton's method

Newton's method is used to approximate the roots of a function $f(x)$. Given an initial guess x^0, it approaches a root, $\lim_{n\to\infty} f(x^n) = 0$, by the iteration $x^{k+1} = x_k - \frac{f(x^k)}{f'(x^k)}$, where f' denotes the derivative of f [137]. This method can be applied to the problem of finding the ground state of a Bose-Einstein condensate by defining

$$F(\phi) = \hat{H}\phi - \mu\phi = -\frac{\hbar^2}{2m}\frac{\partial^2\phi}{\partial x^2} + V\phi + g|\phi|^2\phi - \mu\phi$$

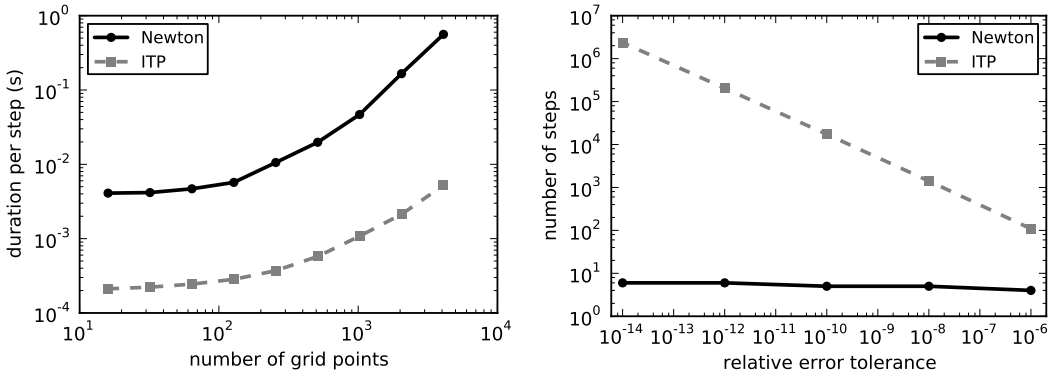

Figure B.3.: Comparison of the scaling characteristics of the Newton method and imaginary time propagation for computing a ground state. The left panel shows the scaling of the computational requirements when improving the number of grid points, i.e. the spatial resolution. The scaling for improved accuracy of the simulation is shown on the right. While single iteration steps take longer for Newton's method, a fewer iterations are required for high accuracy results.

in analogy to the stationary Gross Pitaevskii equation Equation B.3.

Each stationary state ϕ_0 is a root of this functional, $F(\phi_0) = 0$, and can be found by the iteration

$$\phi^{k+1} = \phi^k - J^{-1}(\phi^k) \cdot F(\phi^k)$$

with the Jacobian $J_{ij}(\phi^k) = \frac{\partial F_i}{\partial \phi_j^k}$. The computationally expensive part is the calculation of the inverse of the Jacobian.

When discretizing space on a grid, $F(\phi) = 0$ has to hold for each grid point, i.e. $F(\phi_n) = 0$ for each n. With a grid spacing of Δx, the second derivative can be approximated by a second difference as $\frac{d^2\phi}{dx^2} \approx \frac{\phi_{n+1}+\phi_{n-1}-2\phi_n}{\Delta x^2}$ resulting in a tri-diagonal Jacobian J. Thus, J can be handled as a sparse matrix in order to speed up the calculation of its inverse.

Since the chemical potential μ directly enters $F(\phi)$, knowledge about this parameters is required. The corresponding atom number N follows from the norm of the resulting stationary state. However, the atom number is easier to determine experimentally, such that it is favorable to provide the atom number instead of the chemical potential as an input parameter for the simulations. The additional constraint of a fixed atom number $N = \int |\phi|^2 \mathrm{d}V$ can be included via a Lagrangian multiplier κ resulting in an augmented $F'(\phi)$ having $N_g + 1$ dimensions instead of N_g,

$$F'(\phi) = \begin{pmatrix} F(\phi) + 2\kappa\Delta x\phi \\ \sum_n |\phi_n|^2 \Delta x - N \end{pmatrix} = 0$$

Newton's method has the advantage of quadratic convergence, i.e. fewer iteration steps are required to yield a stationary state with high accuracy as depicted in Figure B.3. Furthermore, this algorithm converges not only to the ground state, but also to any stationary state of the system. However, finding the desired solution requires a good initial guess of the wave function and thus knowledge about the sought-after state. The robustness of imaginary time propagation can be combined with the fast convergence of Newton's method by first iterating in imaginary time to obtain an estimate for the ground state, which can be used as a sensible starting point for Newton's method.

B.2.2. Bogoliubov - de Gennes stability analysis

This subsection summarizes the Bogoliubov - de Gennes analysis, a method for numerically computing the excitation spectrum and the corresponding spatial modes on top of a background state $\psi_0(x)$.

We assume $\psi_0(x)$ to be a known *stationary* solution of Equation B.1 with a time evolution of $\psi_0(x,t) = e^{-i\mu t}\psi_0(x,t=0)$ and $\delta\psi(x,t)$ to be a perturbation on top of $\psi_0(x)$

$$\psi(x,t) = e^{-i\mu t}(\psi_0(x) + \varepsilon\delta\psi(x,t))$$

with $\varepsilon \ll 1$.

Inserting this state in Equation B.1 and ignoring terms of second or higher order in ε, we obtain an equation of motion for the perturbation

$$i\hbar\frac{\partial\delta\psi}{\partial t} + \mu\delta\psi = -\frac{\hbar^2}{2m}\nabla^2\delta\psi + V\delta\psi + 2g|\psi_0|^2\delta\psi + g|\psi_0|^2\delta\psi^* \tag{B.5}$$

where $()^*$ denotes the complex conjugate.

We now assume the perturbation to be of the form

$$\delta\psi(x,t) = a(x)e^{i\omega t} + b^*(x)e^{-i\omega^* t}$$

with the complex amplitudes $a(x)$ and $b(x)$ and the energy $\hbar\omega$. We insert this ansatz into Equation B.5 and sort the equation by the linear independent terms $e^{-i\omega t}$ and $e^{i\omega t}$ resulting in two coupled equations for the excitation modes

$$\begin{aligned}
-\hbar\omega a &= -\frac{\hbar^2}{2m}\nabla^2 a + Va + 2g|\psi_0|^2 a + g|\psi_0|^2 b - \mu a \\
\hbar\omega b &= -\frac{\hbar^2}{2m}\nabla^2 b + Vb + 2g|\psi_0|^2 b + g|\psi_0|^2 a - \mu b
\end{aligned}$$

Thus, the excitation spectrum ω and the corresponding modes a and b are obtained as the eigenvalues and -vectors of the matrix equation

$$\hbar\omega\begin{pmatrix} a \\ b \end{pmatrix} = \begin{pmatrix} L_1 & L_2 \\ L_3 & L_4 \end{pmatrix}\begin{pmatrix} a \\ b \end{pmatrix} \tag{B.6}$$

with

$$\begin{aligned}
L_1 &= -\left(-\frac{\hbar^2}{2m}\nabla^2 + V + 2g|\psi_0|^2 - \mu\right) \\
L_2 &= -g|\psi_0|^2 \\
L_3 &= -L_2^* = g|\psi_0|^2 \\
L_4 &= -L_1^* = -\frac{\hbar^2}{2m}\nabla^2 + V + 2g|\psi_0|^2 - \mu
\end{aligned}$$

For the homogeneous system, $V(x) = 0$, $\mu = ng$, the famous Bogoliubov dispersion law [27] is recovered

$$\hbar\omega = \sqrt{L_1^2 - L_2^2} = \sqrt{\frac{\hbar^2 k^2}{2m}\left(\frac{\hbar^2 k^2}{2m} + 2ng\right)}$$

The generalization of Equation B.6 to the case of two linearly coupled interacting condensates can be calculated using the same method as above and we only give the resulting $4N_g \times 4N_g$ matrix:

$$\hbar\omega \begin{pmatrix} a_1 \\ b_1 \\ a_2 \\ b_2 \end{pmatrix} = \begin{pmatrix} L_{11} & L_{12} & L_{13} & L_{14} \\ L_{21} & L_{22} & L_{23} & L_{24} \\ L_{31} & L_{32} & L_{33} & L_{34} \\ L_{41} & L_{42} & L_{43} & L_{44} \end{pmatrix} \begin{pmatrix} a_1 \\ b_1 \\ a_2 \\ b_2 \end{pmatrix}$$

with

$$\begin{aligned}
L_{11} &= -\frac{\hbar^2}{2m}\nabla^2 + V + 2g_{11}|\psi_{1,0}|^2 + g_{12}|\psi_{2,0}|^2 - \mu_1 \\
L_{12} &= g_{11}|\psi_{1,0}|^2 \\
L_{13} &= g_{12}\psi_{1,0}^*\psi_{2,0} + \hbar\Omega/2 \\
L_{14} &= g_{12}\psi_{1,0}^*\psi_{2,0} \\
L_{21} &= -L_{12}^* \\
L_{22} &= -L_{11}^* \\
L_{23} &= -L_{14}^* \\
L_{24} &= -L_{13}^* \\
L_{31} &= g_{12}\psi_{1,0}^*\psi_{2,0} + \hbar\Omega/2 \\
L_{32} &= g_{12}\psi_{1,0}^*\psi_{2,0} \\
L_{33} &= -\frac{\hbar^2}{2m}\nabla^2 + V + 2g_{22}|\psi_{2,0}|^2 + g_{12}|\psi_{1,0}|^2 - \mu_2 \\
L_{34} &= g_{22}|\psi_{2,0}|^2 \\
L_{41} &= -L_{32}^* \\
L_{42} &= -L_{31}^* \\
L_{43} &= -L_{34}^* \\
L_{44} &= -L_{33}^*
\end{aligned}$$

Here, the strength of the linear coupling is parametrized by the Rabi frequency Ω and g_{ij} are the intra- and inter-species interaction parameters.

Practical tips

We conclude this section with a few tips regarding the numerical solution and the interpretation of the Bogoliubov - de Gennes equations.

- The Bogoliubov - de Gennes equations require knowledge of the chemical potential μ, which can be calculated numerically using the known background state ψ_0 and Equation B.3.
- The second derivative can be calculated on a grid using finite differences as mentioned in the discussion of Newton's method. This results in the matrices L_{ii} not being diagonal any more but also having entries in the first off-diagonals directly above and below the main diagonal.
- The numerically obtained excitation modes in general are not plane waves. Thus it is not straight-forward to assign a wave-vector k to each mode in order to obtain dispersion re-

lations as shown in subsection 2.4.4. We estimate k by the determining the position of the largest amplitude in the Fourier spectrum of the difference profile of the excitation modes of the two components. In addition, each excited mode has to be assigned to one of the two branches of the dispersion. As the gapped branch corresponds to out-of-phase modulation and the other branch to in-phase modulation of the two components, we assign modes whose maximum amplitude in the Fourier spectrum is larger than a threshold to the gapped branch. The threshold value is chosen such that each branch contains the same number of modes.

- The derivation of Equation B.6 required the background state $\psi_0(x,t)$ to be stationary, i.e. $\psi_0(x,t) = e^{-i\mu t}\psi_0(x,t=0)$. If this condition is not fulfilled the Bogoliubov - de Gennes analysis does not yield reliable results. This is the case for a superposition of two condensates in a trap, where the symmetry is broken by different intra-species scattering lengths $a_{11} \neq a_{22}$. Thus we have to assume $a_{11} = a_{22}$ when numerically calculating the excitation spectra for inhomogeneous atomic clouds. While this is not exactly fulfilled in ^{87}Rb it is a good approximation of the experimental system.

B.2.3. Time integration

In the previous sections we discussed algorithms to numerically compute stationary states of the GPE and their excitation spectra. Now, we will introduce two methods for calculating the time evolution of a wave function by integrating the Gross-Pitaevskii equation: real time propagation, which is straight forward to implement if imaginary time propagation is already available, and a Runge-Kutta method, which is a generic, and thus more flexible method for integrating differential equations.

The time dynamics of a state is computed in discrete time steps Δt. Similar to the conditions for the spatial grid, this temporal grid has to be chosen significantly smaller than the characteristic timescale of the dynamics. Additionally, small time steps are necessary to avoid the accumulation of numerical errors in each time step.

Real time propagation

As explained in the context of imaginary time propagation, the time evolution of a wave function is given by the propagator defined in Equation B.4. Thus, the same split-step fast Fourier transform algorithm as for imaginary time propagation can be applied to calculate the time dynamics of a condensate. The only change is that real time is used instead of imaginary time.

Again, this method works well if the real space part of the Hamiltonian $\hat{H}_x$ is diagonal, such that the matrix exponential can be computed efficiently. For two-component condensates with a linear coupling between the species, the matrix representation of the Hamiltonian is no longer diagonal, but includes two populated off-diagonals. In this special case, the Hamiltonian can be diagonalized analytically, but the extension to more complex scenarios is difficult.

Runge-Kutta method

A more universal approach to integrating differential equations is employing general explicit methods. As a simple example, we will briefly outline the Euler method: Given a differential equation $y'(t) = f(t, y(t))$ (in our case Equation B.1) with an initial value $y(t_0) = y_0$ (corresponding to the ground state), we can use a first order Taylor expansion to approximate $y(t_0 + \Delta t) \approx y(t_0) + \Delta t \cdot f(t_0, y_0)$. Iteratively repeating this procedure yields an approximate solution of the differential equation. Higher order terms can be included such that the error in each iteration is smaller

at the cost of higher computational complexity. A good compromise is a fourth-order Runge-Kutta method. A more detailed introduction to the numerical solution of differential equations can be found in [138].

The expansion of the one-dimensional example above to the N_g dimensional Gross-Pitaevskii equation on a grid is straight-forward. The only hitch is the kinetic energy term, which can be approximated using second order finite differences as explained in the context of Newton's method.

For simple scenarios in which the Hamiltonian can be easily diagonalized, this method is slower than real time propagation, but it can be easily generalized to more complex situations.

C. Calibration of in-situ imaging near the Feshbach resonance

For the detection of the atomic clouds we employ high-intensity absorption imaging [64]. A detailed description of our imaging setup and the atom number calibration was given in the context of spin squeezing measurements, where knowledge of the absolute atom number is critical [86, 32]. The limits or our imaging setup are discussed in [26].

The observable for the experiments on the miscible-immiscible phase transition discussed in this thesis is the difference of the density profiles of the atomic clouds. Knowledge of the absolute atom density is important as it enters the relevant parameter $n \cdot g_s$, where g_s is the interaction parameter and n the linear atom density (see subsection 2.3.1). The accuracy in this parameter is limited by shot-to-shot fluctuations in the atom density of about 10% and the systematic uncertainty of the inter-species scattering length a_{12} close to the Feshbach resonance. Thus, a calibration of the absolute atom number within these uncertainties is desired.

However, the experiments under discussion require *in-situ* detection of the spatial density distributions of the two components. An imaging pulse duration of 10 µs was chosen in order to minimize blurring due to defocussing and heating while keeping a good signal-to-noise ratio [26]. Ramping down the magnetic field from close to the Feshbach resonance at 9.09 G to fields below 0.5 G for detection takes about 300 ms, which is a lot longer than the time scale of spatial dynamics and atom loss in the condensates. Thus, we modify the imaging sequence to detect the atomic clouds directly at a magnetic field close to the Feshbach resonance where the experiments are performed. The necessary steps are described in this appendix.

C.1. Adjusting the imaging frequency for maximum detectivity

The linear Zeeman shift at magnetic fields close to the Feshbach resonance is about $6.3\,\mathrm{MHz}/(\Delta m_F)$, which is on the same order as the natural linewidth of the employed ^{87}Rb D2 line of 6.07 MHz [67]. Thus the frequency of the imaging laser beam has to be adjusted for a maximum atomic absorption. We experimentally determine the best frequency by using the zero-field calibration as a starting point and optimizing the signal to noise ratio, i.e. the deduced atom number as shown in Figure C.1.

The frequency of the imaging beam is optimized for resonance to the $(F = 2) \leftrightarrow (F' = 3)$ transition of the D2 line. The two atomic clouds are detected consecutively. Atoms in state $|2\rangle$ are imaged first and lost due to photon recoil in the absorption process. Afterwards atoms in state $|1\rangle$ are transferred to state $|2\rangle$ by a repumping laser and subsequently detected.

As shown in Figure C.1 the sensitivities for atoms in state $|1\rangle$ and $|2\rangle$ are both maximal at the same frequency, but their relative sensitivities are significantly different. This effect can be caused by an inefficient transfer of atoms from state $|1\rangle$ to $|2\rangle$ by the repumping laser, since its frequency is not adjusted for high field imaging. This leads to an underestimation of the atom number in the $F = 1$ manifold. In addition different magnetic sublevels m_F are populated when directly imaging atoms in state $|2\rangle$ compared to the situation after the atoms in state $|1\rangle$ have been repumped to the $F = 2$ manifold. Thus, different Clebsch-Gordan coefficients influence the relative detectivity of the two components as well.

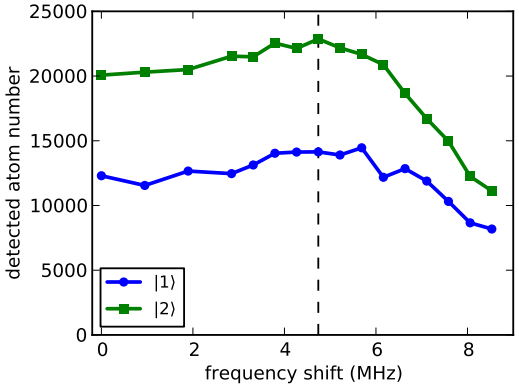

Figure C.1.: Detected number of atoms in the two hyperfine states after a $\pi/2$-pulse when varying the frequency of the imaging laser beam relative to the resonance at low magnetic field. The sensitivity is maximal at a shift of 4.7 MHz, but very different for the two species. The real number of atoms in the condensate is kept constant. The dashed line indicates the chosen working point.

C.2. Absolute atom number calibration

In order to estimate the detection error in the absolute atom number we compare the measurement at high magnetic field with the well characterized [26] imaging method at low field for different atom numbers (realized by variation of the final value of the evaporation ramp in the optical dipole traps). This comparison is only possible for a single species atomic cloud prepared in the F=1 hyperfine manifold, since neither spin-relaxation loss nor Feshbach loss reduce the atom number while ramping down the magnetic field. Atom loss due to heating or movement of the atomic cloud (e.g. caused by magnetic field gradients during the magnetic field ramp) are assumed to be small since neither the shape nor the position of the condensate changes during the ramp. The left panel of Figure C.2 summarizes these calibration measurements along with a linear fit that is used to correct for the detection error when imaging at high field. The number of atoms in the $F = 1$ manifold is underestimated by a factor 1.5.

The detection error for atoms in the $F = 2$ manifold is estimated by comparing the detected atom number with the corrected atom number in $F = 1$ after a $\pi/2$-pulse, which reliably creates an equal superposition of the two states.[1] The right panel of Figure C.2 shows the resulting imbalance versus total atom number. As the imbalance is close to zero the imaging calibration for the $F = 2$ atoms does not need further adjustment. The remaining drift of the imbalance originates from non-linearities in the calibration of the $F = 1$ atom number.

C.3. Imaging in the presence of a linear coupling field

In many experiments the amplitude of the linear coupling field is varied during the experimental cycle, for example when performing ramps or to compensate for atom loss. In this case the programming of the arbitrary waveform generator takes up to 20 s depending on the details of the sequence. In order to minimize variations in the duration of the experimental cycle the generator is programmed only once for a series of measurements where the time evolution of the atomic clouds

[1] Several oscillation cycles are evaluated for the measurement of the Rabi frequency. A sinusoidal fit to the oscillations provides a value for the Rabi frequency that is nearly independent of the details of the atom number calibration.

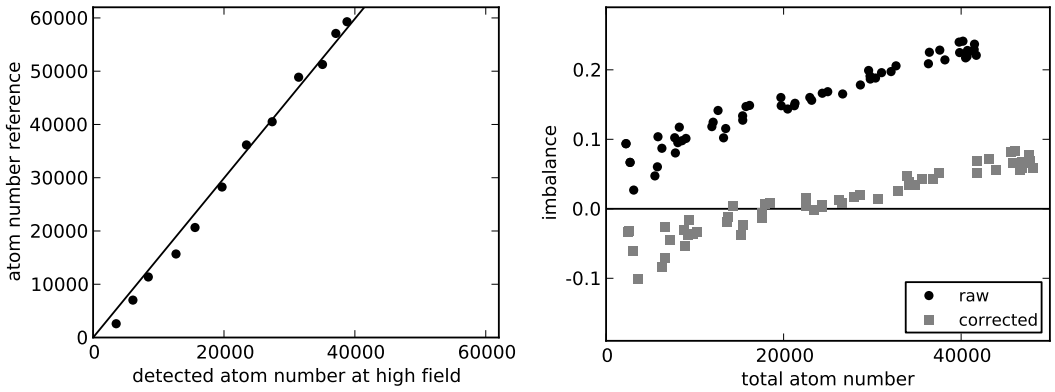

Figure C.2.: (left) Detected number of atoms in the F=1 manifold against the results of a reference measurement at low magnetic field. The detected atom number is underestimated by a factor 1.5. A linear fit (solid line) is used as a calibration curve for deducing the real atom number. (right) The imbalance after a $\pi/2$-pulse both for raw (black circles) and corrected (gray squares) $F = 1$ atom numbers is used to approximate errors in the detection of $F = 2$ atoms. After correction of the $F = 1$ atom numbers, the imbalance is close to zero meaning that the detection error on the F=2 atom number is small. The remaining drift of the imbalance with the total atom number is caused by a non-linearity in the atom number detection, i.e. a quadratic contribution which is not compensated when using the linear fit as a calibration.

is measured for a given sequence of the linear coupling. Thus, images at early evolution times (e.g. during the ramp) are taken in the presence of the coupling field. By comparing measurements with and without a linear coupling we found the detected number of atoms in the $F = 1$ ($F = 2$) manifold to change by a factor 1.02 ± 0.06 (1.04 ± 0.04) compatible with 1.

Bibliography

[1] S. Sachdev. *Quantum Phase Transitions*. Cambridge University Press, 2 edition, 2011.

[2] T Donner, S Ritter, T Bourdel, A Ottl, M Köhl, and T Esslinger. Critical behavior of a trapped interacting Bose gas. *Science*, 315(5818):1556–8, 2007.

[3] Zoran Hadzibabic, Peter Krüger, Marc Cheneau, Baptiste Battelier, and Jean Dalibard. Berezinskii–Kosterlitz–Thouless crossover in a trapped atomic gas. *Nature*, 441(7097):1118–1121, 2006.

[4] Markus Greiner, Olaf Mandel, Tilman Esslinger, Theodor W. Hansch, and Immanuel Bloch. Quantum phase transition from a superfluid to a Mott insulator in a gas of ultracold atoms. *Nature*, 415(6867):39–44, 2002.

[5] W. S. Bakr, A. Peng, M. E. Tai, R. Ma, J. Simon, J. I. Gillen, S. Fölling, L. Pollet, and M. Greiner. Probing the Superfluid-to-Mott Insulator Transition at the Single-Atom Level. *Science*, 329:547, 2010.

[6] K. Baumann, C. Guerlin, F. Brennecke, and T. Esslinger. Dicke quantum phase transition with a superfluid gas in an optical cavity. *Nature*, 464:1301–1306, 2010.

[7] C. N. Weiler, T. W. Neely, D. R. Scherer, A. S. Bradley, M. J. Davis, and B. P. Anderson. Spontaneous vortices in the formation of Bose-Einstein condensates. *Nature*, 455:948–951, 2008.

[8] L E Sadler, J M Higbie, S R Leslie, M Vengalattore, and D M Stamper-Kurn. Spontaneous symmetry breaking in a quenched ferromagnetic spinor Bose-Einstein condensate. *Nature*, 443(7109):312–5, 2006.

[9] Jochen Kronjäger, Christoph Becker, Parvis Soltan-Panahi, Kai Bongs, and Klaus Sengstock. Spontaneous Pattern Formation in an Antiferromagnetic Quantum Gas. *Phys. Rev. Lett.*, 105(9):090402, 2010.

[10] Manuel Endres, Takeshi Fukuhara, David Pekker, Marc Cheneau, Peter Schauβ, Christian Gross, Eugene Demler, Stefan Kuhr, and Immanuel Bloch. The/Higgs/'amplitude mode at the two-dimensional superfluid/Mott insulator transition. *Nature*, 487(7408):454–458, 2012.

[11] K. Baumann, R. Mottl, F. Brennecke, and T. Esslinger. Exploring Symmetry Breaking at the Dicke Quantum Phase Transition. *Phys. Rev. Lett.*, 107(14):140402, 2011.

[12] Chen-Lung Hung, Xibo Zhang, Nathan Gemelke, and Cheng Chin. Observation of scale invariance and universality in two-dimensional Bose gases. *Nature*, 470(7333):236–9, 2011.

[13] Xibo Zhang, Chen-Lung Hung, Shih-Kuang Tung, and Cheng Chin. Observation of quantum criticality with ultracold atoms in optical lattices. *Science*, 335(6072):1070–2, 2012.

[14] Marc Cheneau, Peter Barmettler, Dario Poletti, Manuel Endres, Peter Schauss, Takeshi Fukuhara, Christian Gross, Immanuel Bloch, Corinna Kollath, and Stefan Kuhr. Light-cone-like spreading of correlations in a quantum many-body system. *Nature*, 481(7382):484–7, 2012.

[15] M Gring, M Kuhnert, T Langen, T Kitagawa, B Rauer, M Schreitl, I Mazets, D Adu Smith, E Demler, and J Schmiedmayer. Relaxation and prethermalization in an isolated quantum system. *Science*, 337(6100):1318–22, 2012.

[16] Anatoli Polkovnikov, Krishnendu Sengupta, Alessandro Silva, and Mukund Vengalattore. Colloquium : Nonequilibrium dynamics of closed interacting quantum systems. *Rev. Mod. Phys.*, 83(3):863–883, 2011.

[17] Ilya M. Merhasin, Boris A. Malomed, and Rodislav Driben. Transition to miscibility in a binary Bose–Einstein condensate induced by linear coupling. *Journal of Physics B: Atomic, Molecular and Optical Physics*, 38(7):877, 2005.

[18] Jacopo Sabbatini, Wojciech H. Zurek, and Matthew J. Davis. Phase Separation and Pattern Formation in a Binary Bose-Einstein Condensate. *Phys. Rev. Lett.*, 107(23):230402, 2011.

[19] B. D. Esry and Chris H. Greene. Spontaneous spatial symmetry breaking in two-component Bose-Einstein condensates. *Phys. Rev. A*, 59(2):1457–1460, Feb 1999.

[20] Cheng Chin, Rudolf Grimm, Paul Julienne, and Eite Tiesinga. Feshbach resonances in ultracold gases. *Rev. Mod. Phys.*, 82(2):1225–1286, 2010.

[21] Claude Cohen-Tannoudji, Jacques Dupont-Roc, Gilbert Grynberg, and Pierre Meystre. *Atom-Photon Interactions: Basic Processes and Applications*. New York: Wiley, 1992.

[22] E. Nicklas, H. Strobel, T. Zibold, C. Gross, B. A. Malomed, P. G. Kevrekidis, and M. K. Oberthaler. Rabi Flopping Induces Spatial Demixing Dynamics. *Phys. Rev. Lett.*, 107(19):193001, 2011.

[23] C. Gross, T. Zibold, E. Nicklas, J. Estève, and M. K. Oberthaler. Nonlinear atom interferometer surpasses classical precision limit. *Nature*, 464(7292):1165–1169, 2010.

[24] Tilman Zibold, Eike Nicklas, Christian Gross, and Markus K. Oberthaler. Classical Bifurcation at the Transition from Rabi to Josephson Dynamics. *Phys. Rev. Lett.*, 105(20):204101, 2010.

[25] C Gross, H Strobel, E Nicklas, T Zibold, N Bar-Gill, G Kurizki, and M K Oberthaler. Atomic homodyne detection of continuous-variable entangled twin-atom states. *Nature*, 480(7376):219–23, 2011.

[26] W. Muessel, H. Strobel, M. Joos, E. Nicklas, I. Stroescu, J. Tomkovic, D. Hume, and M. Oberthaler. Optimized absorption imaging of mesoscopic atomic clouds. *to be published*.

[27] Lev Pitaevskii and Sandro Stringari. *Bose-Einstein Condensation*. Oxford University Press, New York, 2003.

[28] Chaohong Lee. Universality and Anomalous Mean-Field Breakdown of Symmetry-Breaking Transitions in a Coupled Two-Component Bose-Einstein Condensate. *Phys. Rev. Lett.*, 102(7):070401, 2009.

[29] E. Gross. Structure of a quantized vortex in boson systems. *Il Nuovo Cimento (1955-1965)*, 20(3):454–477, 1961.

[30] L. P. Pitaevskii. Vortex Lines in an imperfect Bose Gas. *Soviet Physics JETP-USSR*, 13(2), 1961.

[31] Harold J. Metcalf and Peter Van der Straten. *Laser cooling and trapping*. Springer Verlag, 1999.

[32] Christian Gross. *Spin squeezing and non-linear atom interferometry with Bose-Einstein condensates.* PhD thesis, University of Heidelberg, 2010.

[33] C. P. Search and P. R. Berman. Manipulating the speed of sound in a two-component Bose-Einstein condensate. *Phys. Rev. A*, 63(4):043612, 2001.

[34] M. J. Steel and M. J. Collett. Quantum state of two trapped Bose-Einstein condensates with a Josephson coupling. *Phys. Rev. A*, 57(4):2920–2930, 1998.

[35] Masahiro Kitagawa and Masahito Ueda. Squeezed spin states. *Phys. Rev. A*, 47(6):5138–5143, 1993.

[36] M. F. Riedel, P. Böhi, Y. Li, T. W. Hänsch, A. Sinatra, and P. Treutlein. Atom-chip-based generation of entanglement for quantum metrology. *Nature*, 464(7292):1170–1173, 2010.

[37] B. D. Josephson. Possible new effects in superconductive tunnelling. *Physics Letters*, 1(7):251–253, 1962.

[38] Anthony J. Leggett. Bose-Einstein condensation in the alkali gases: Some fundamental concepts. *Rev. Mod. Phys.*, 73(2):307–356, 2001.

[39] Tilman Zibold. *Classical Bifurcation and Entanglement Generation in an Internal Bosonic Josephson Junction.* PhD thesis, University of Heidelberg, 2012.

[40] R. Gati and M. K. Oberthaler. A bosonic Josephson junction. *Journal of Physics B: Atomic, Molecular and Optical Physics*, 40(10):–61, 2007.

[41] Paolo Tommasini, E. J. V. de Passos, A. F. R. de Toledo Piza, M. S. Hussein, and E. Timmermans. Bogoliubov theory for mutually coherent condensates. *Phys. Rev. A*, 67(2):023606, 2003.

[42] P. Ao and S. T. Chui. Binary Bose-Einstein condensate mixtures in weakly and strongly segregated phases. *Phys. Rev. A*, 58(6):4836–4840, 1998.

[43] E. Timmermans. Phase Separation of Bose-Einstein Condensates. *Phys. Rev. Lett.*, 81(26):5718–5721, 1998.

[44] P. B. Blakie, R. J. Ballagh, and C. W. Gardiner. Dressed states of a two component Bose-Einstein condensate. *Journal of Optics B: Quantum and Semiclassical Optics*, 1(4):378, 1999.

[45] C. P. Search, A. G. Rojo, and P. R. Berman. Ground state and quasiparticle spectrum of a two-component Bose-Einstein condensate. *Phys. Rev. A*, 64(1):013615, 2001.

[46] M. Abad and A. Recati. A study of coherently coupled two-component Bose-Einstein Condensates. *ArXiv e-prints*, 2013.

[47] Tin-Lun Ho and V. B. Shenoy. Binary Mixtures of Bose Condensates of Alkali Atoms. *Phys. Rev. Lett.*, 77(16):3276–3279, 1996.

[48] H. Pu and N. P. Bigelow. Properties of Two-Species Bose Condensates. *Phys. Rev. Lett.*, 80(6):1130–1133, 1998.

[49] Marek Trippenbach, Krzysztof Góral, Kazimierz Rzazewski, Boris Malomed, and Y. B. Band. Structure of binary Bose-Einstein condensates. *Journal of Physics B: Atomic, Molecular and Optical Physics*, 33(19):4017, 2000.

[50] Kevin E Strecker, Guthrie B Partridge, Andrew G Truscott, and Randall G Hulet. Formation and propagation of matter-wave soliton trains. *Nature*, 417(6885):150–3, 2002.

[51] Elena V. Goldstein and Pierre Meystre. Quasiparticle instabilities in multicomponent atomic condensates . *Phys. Rev. A*, 55(4):2935–2940, 1997.

[52] C. K. Law, H. Pu, N. P. Bigelow, and J. H. Eberly. "Stability Signature" in Two-Species Dilute Bose-Einstein Condensates. *Phys. Rev. Lett.*, 79(17):3105–3108, 1997.

[53] V. P. Mineev. Theory of Solution of two almost perfect Bose Gases. *Sov. Phys. JETP*, 40:132, 1974.

[54] W. B. Colson and Alexander L. Fetter. Mixtures of Bose liquids at finite temperature. *Journal of Low Temperature Physics*, 33(3):231–242, 1978.

[55] Bogdan Damski and Wojciech H. Zurek. Quantum phase transition in space in a ferromagnetic spin-1 Bose–Einstein condensate. *New Journal of Physics*, 11(6):063014, 2009.

[56] Jacopo Sabbatini, Wojciech H. Zurek, and Matthew J. Davis. Causality and defect formation in the dynamics of an engineered quantum phase transition in a coupled binary Bose–Einstein condensate. *New Journal of Physics*, 14(9):095030, 2012.

[57] P. Ao and S. T. Chui. Two stages in the evolution of binary alkali Bose-Einstein condensate mixtures towards phase segregation. *Journal of Physics B: Atomic, Molecular and Optical Physics*, 33(3):535, 2000.

[58] Kenichi Kasamatsu and Makoto Tsubota. Multiple Domain Formation Induced by Modulation Instability in Two-Component Bose-Einstein Condensates. *Phys. Rev. Lett.*, 93(10):100402, 2004.

[59] H. Pu and N. P. Bigelow. Collective Excitations, Metastability, and Nonlinear Response of a Trapped Two-Species Bose-Einstein Condensate. *Phys. Rev. Lett.*, 80(6):1134–1137, 1998.

[60] S. De, D. L. Campbell, R. M. Price, A. Putra, B. M. Anderson, and I. B. Spielman. Quenched binary Bose-Einstein condensates: spin domain formation and coarsening. *arXiv preprint 1205.1888*, 2013.

[61] Bernd Eiermann. *Kohärente nichtlineare Materiewellendynamik - Helle atomare Solitonen -*. PhD thesis, University of Heidelberg, 2004.

[62] Michael Albiez. *Observation of nonlinear tunneling of a Bose-Einstein condensate in a single Josephson junction*. PhD thesis, University of Heidelberg, 2005.

[63] Andreas Weller. *Dynamics and Interaction of Dark Solitons in Bose-Einstein Condensates*. PhD thesis, University of Heidelberg, 2009.

[64] G. Reinaudi, T. Lahaye, Z. Wang, and D. Guéry-Odelin. Strong saturation absorption imaging of dense clouds of ultracold atoms. *Opt. Lett.*, 32(21):3143–3145, 2007.

[65] Jens Appmeier. Bose-Einstein condensates in a double well potential: A route to quantum interferometry. Master's thesis, University of Heidelberg, 2007.

[66] Thibaut Jacqmin, Julien Armijo, Tarik Berrada, Karen V. Kheruntsyan, and Isabelle Bouchoule. Sub-Poissonian Fluctuations in a 1D Bose Gas: From the Quantum Quasicondensate to the Strongly Interacting Regime. *Phys. Rev. Lett.*, 106(23):230405, Jun 2011.

[67] D. A. Steck. Rubidium 87 D Line Data, 2010.

[68] Helmut Strobel. Quantum Spin Dynamics in Mesoscopic Bose-Einstein Condensates. Master's thesis, University of Heidelberg, 2011.

[69] D. M. Harber, H. J. Lewandowski, J. M. McGuirk, and E. A. Cornell. Effect of cold collisions on spin coherence and resonance shifts in a magnetically trapped ultracold gas. *Phys. Rev. A*, 66(5):053616, 2002.

[70] C. Deutsch, F. Ramirez-Martinez, C. Lacroûte, F. Reinhard, T. Schneider, J. N. Fuchs, F. Piéchon, F. Laloë, J. Reichel, and P. Rosenbusch. Spin Self-Rephasing and Very Long Coherence Times in a Trapped Atomic Ensemble. *Phys. Rev. Lett.*, 105(2):020401, 2010.

[71] M. Egorov, R. P. Anderson, V. Ivannikov, B. Opanchuk, P. Drummond, B. V. Hall, and A. I. Sidorov. Long-lived periodic revivals of coherence in an interacting Bose-Einstein condensate. *Phys. Rev. A*, 84(2):021605, 2011.

[72] M. Erhard, H. Schmaljohann, J. Kronjäger, K. Bongs, and K. Sengstock. Measurement of a mixed-spin-channel Feshbach resonance in ^{87}Rb . *Phys. Rev. A*, 69(3):032705, 2004.

[73] Artur Widera, Olaf Mandel, Markus Greiner, Susanne Kreim, Theodor W. Hänsch, and Immanuel Bloch. Entanglement Interferometry for Precision Measurement of Atomic Scattering Properties. *Phys. Rev. Lett.*, 92(16):160406, 2004.

[74] Satoshi Tojo, Yoshihisa Taguchi, Yuta Masuyama, Taro Hayashi, Hiroki Saito, and Takuya Hirano. Controlling phase separation of binary Bose-Einstein condensates via mixed-spin-channel Feshbach resonance. *Phys. Rev. A*, 82(3):033609, 2010.

[75] Timo Ottenstein. A New Objective for High Resolution Imaging of Bose-Einstein Condensates. Master's thesis, University of Heidelberg, 2006.

[76] D. S. Hall, M. R. Matthews, J. R. Ensher, C. E. Wieman, and E. A. Cornell. Dynamics of Component Separation in a Binary Mixture of Bose-Einstein Condensates. *Phys. Rev. Lett.*, 81(8):1539–1542, 1998.

[77] K. M. Mertes, J. W. Merrill, R. Carretero-González, D. J. Frantzeskakis, P. G. Kevrekidis, and D. S. Hall. Nonequilibrium Dynamics and Superfluid Ring Excitations in Binary Bose-Einstein Condensates. *Phys. Rev. Lett.*, 99(19):190402, 2007.

[78] Yun Li, P. Treutlein, J. Reichel, and A. Sinatra. Spin squeezing in a bimodal condensate: spatial dynamics and particle losses. *Eur. Phys. J. B*, 68(3):365–381, 2009.

[79] M. Egorov, B. Opanchuk, P. Drummond, B. V. Hall, P. Hannaford, and A. I. Sidorov. Precision measurements of s-wave scattering lengths in a two-component Bose-Einstein condensate. *ArXiv e-prints*, 2012.

[80] M. R. Andrews, D. M. Kurn, H. J. Miesner, D. S. Durfee, C. G. Townsend, S. Inouye, and W. Ketterle. Propagation of Sound in a Bose-Einstein Condensate. *Phys. Rev. Lett.*, 79(4):553–556, Jul 1997.

[81] M. R. Andrews, D. M. Stamper-Kurn, H. J. Miesner, D. S. Durfee, C. G. Townsend, S. Inouye, and W. Ketterle. Erratum: Propagation of Sound in a Bose-Einstein Condensate [Phys. Rev. Lett. 79, 553 (1997)]. *Phys. Rev. Lett.*, 80(13):2967–2967, Mar 1998.

[82] J. Dziarmaga. Dynamics of a quantum phase transition and relaxation to a steady state. *Advances in Physics*, 59:1063–1189, 2010.

[83] Jürgen Berges, Sebastian Scheffler, and Dénes Sexty. Bottom-up isotropization in classical-statistical lattice gauge theory. *Phys. Rev. D*, 77(3):034504, 2008.

[84] MR Matthews, DS Hall, DS Jin, JR Ensher, CE Wieman, EA Cornell, F Dalfovo, C Minniti, and S Stringari. Dynamical response of a Bose-Einstein condensate to a discontinuous change in internal state. *Physical Review Letters*, 81(2):243–247, 1998.

[85] E. A. Cornell, D. S. Hall, M. R. Matthews, and C. E. Wieman. Having it both ways: Distinguishable yet phase-coherent mixtures of Bose-Einstein condensates. *J. Low Temp. Phys.*, 113, 1998. JILA Pub. 6133.

[86] J. Esteve, C. Gross, A. Weller, S. Giovanazzi, and M. K. Oberthaler. Squeezing and entanglement in a Bose–Einstein condensate. *Nature*, 455(7217):1216, 2008.

[87] M. R. Matthews, B. P. Anderson, P. C. Haljan, D. S. Hall, M. J. Holland, J. E. Williams, C. E. Wieman, and E. A. Cornell. Watching a Superfluid Untwist Itself: Recurrence of Rabi Oscillations in a Bose-Einstein Condensate. *Phys. Rev. Lett.*, 83(17):3358–3361, 1999.

[88] J. Williams, R. Walser, J. Cooper, E. A. Cornell, and M. Holland. Excitation of a dipole topological state in a strongly coupled two-component Bose-Einstein condensate. *Phys. Rev. A*, 61(3):033612, 2000.

[89] Stewart D. Jenkins and T. A. Brian Kennedy. Spin squeezing in a driven Bose-Einstein condensate. *Phys. Rev. A*, 66(4):043621, 2002.

[90] Stewart D. Jenkins and T. A. B. Kennedy. Dynamic stability of dressed condensate mixtures. *Phys. Rev. A*, 68(5):053607, 2003.

[91] Y-J Lin, K Jiménez-García, and I B Spielman. Spin-orbit-coupled Bose-Einstein condensates. *Nature*, 471(7336):83–6, 2011.

[92] N Timoney, I Baumgart, M Johanning, A F Varón, M B Plenio, A Retzker, and Ch Wunderlich. Quantum gates and memory using microwave-dressed states. *Nature*, 476(7359):185–8, 2011.

[93] Norman F. Ramsey. A Molecular Beam Resonance Method with Separated Oscillating Fields. *Phys. Rev.*, 78(6):695–699, 1950.

[94] A. Chandran, A. Erez, S. S. Gubser, and S. L. Sondhi. Kibble-Zurek problem: Universality and the scaling limit. *Physical Review B*, 86(6):064304, 2012.

[95] C. De Grandi, V. Gritsev, and A. Polkovnikov. Quench dynamics near a quantum critical point. *Phys. Rev. B*, 81(1):012303, 2010.

[96] T. W. B. Kibble. Some implications of a cosmological phase transition. *Physics Reports*, 67(1):183–199, 1980.

[97] W. H. Zurek. Cosmological experiments in superfluid helium? *Nature*, 317:505–508, 1985.

[98] T. W. B. Kibble. Topology of cosmic domains and strings. *Journal of Physics A: Mathematical and General*, 9(8):1387, 1976.

[99] T.W.B. Kibble. Phase-Transition Dynamics in the Lab and the Universe. *Physics Today*, 60:47, 2007.

[100] W. H. Zurek. Cosmological experiments in condensed matter systems. *Physics Reports*, 276:177–221, 1996.

[101] I. Chuang, B. Yurke, R. Durrer, and N. Turok. Cosmology in the laboratory - Defect dynamics in liquid crystals. *Science*, 251:1336–1342, 1991.

[102] M. J. Bowick, L. Chandar, E. A. Schiff, and A. M. Srivastava. The Cosmological Kibble Mechanism in the Laboratory: String Formation in Liquid Crystals. *Science*, 263:943–945, 1994.

[103] R. Monaco, J. Mygind, and R. J. Rivers. Zurek-Kibble Domain Structures: The Dynamics of Spontaneous Vortex Formation in Annular Josephson Tunnel Junctions. *Phys. Rev. Lett.*, 89(8):080603, Aug 2002.

[104] R. Monaco, J. Mygind, and R. J. Rivers. Spontaneous fluxon formation in annular Josephson tunnel junctions. *Phys. Rev. B*, 67(10):104506, Mar 2003.

[105] S. Ducci, P. L. Ramazza, W. González-Viñas, and F. T. Arecchi. Order Parameter Fragmentation after a Symmetry-Breaking Transition. *Phys. Rev. Lett.*, 83(25):5210–5213, Dec 1999.

[106] P. C. Hendry, N. S. Lawson, R. A. M. Lee, P. V. E. McClintock, and C. D. H. Williams. Generation of defects in superfluid ^{4}He as an analogue of the formation of cosmic strings. *Nature*, 368:315–317, 1994.

[107] M. E. Dodd, P. C. Hendry, N. S. Lawson, P. V. E. McClintock, and C. D. H. Williams. Nonappearance of Vortices in Fast Mechanical Expansions of Liquid ^{4}He through the Lambda Transition. *Physical Review Letters*, 81:3703–3706, 1998.

[108] V. M. H. Ruutu, V. B. Eltsov, A. J. Gill, T. W. B. Kibble, M. Krusius, Y. G. Makhlin, B. Plaçais, G. E. Volovik, and W. Xu. Vortex formation in neutron-irradiated superfluid ^{3}He as an analogue of cosmological defect formation. *Nature*, 382:334–336, 1996.

[109] C. Bäuerle, Y. M. Bunkov, S. N. Fisher, H. Godfrin, and G. R. Pickett. Laboratory simulation of cosmic string formation in the early Universe using superfluid ^{3}He. *Nature*, 382:332–334, jul 1996.

[110] D V Freilich, D M Bianchi, A M Kaufman, T K Langin, and D S Hall. Real-time dynamics of single vortex lines and vortex dipoles in a Bose-Einstein condensate. *Science*, 329(5996):1182–5, 2010.

[111] Wojciech H. Zurek. Causality in Condensates: Gray Solitons as Relics of BEC Formation. *Phys. Rev. Lett.*, 102(10):105702, 2009.

[112] E. Witkowska, P. Deuar, M. Gajda, and K. Rzążewski. Solitons as the Early Stage of Quasicondensate Formation during Evaporative Cooling. *Physical Review Letters*, 106(13):135301, apr 2011.

[113] Bogdan Damski. The Simplest Quantum Model Supporting the Kibble-Zurek Mechanism of Topological Defect Production: Landau-Zener Transitions from a New Perspective. *Phys. Rev. Lett.*, 95(3):035701, 2005.

[114] Wojciech H. Zurek, Uwe Dorner, and Peter Zoller. Dynamics of a Quantum Phase Transition. *Phys. Rev. Lett.*, 95(10):105701, 2005.

[115] Jacek Dziarmaga. Dynamics of a Quantum Phase Transition: Exact Solution of the Quantum Ising Model. *Phys. Rev. Lett.*, 95(24):245701, 2005.

[116] David Chen, Matthew White, Cecilia Borries, and Brian DeMarco. Quantum Quench of an Atomic Mott Insulator. *Phys. Rev. Lett.*, 106(23):235304, 2011.

[117] M. Mielenz, J. Brox, S. Kahra, G. Leschhorn, M. Albert, T. Schaetz, H. Landa, and B. Reznik. Trapping of Topological-Structural Defects in Coulomb Crystals. *Physical Review Letters*, 110(13):133004, 2013.

[118] S. Ulm, J. Roßnagel, G. Jacob, C. Degünther, S. T. Dawkins, U. G. Poschinger, R. Nigmatullin, A. Retzker, M. B. Plenio, F. Schmidt-Kaler, and K. Singer. Observation of the Kibble-Zurek scaling law for defect formation in ion crystals. *ArXiv e-prints*, 2013.

[119] Moritz Höfer. Observation of Pattern Formation in a Quenched Binary Bose-Einstein Condensate. Master's thesis, University of Konstanz, 2012.

[120] Nuno D. Antunes, Pedro Gandra, and Ray J. Rivers. Is domain formation decided before or after the transition? *Phys. Rev. D*, 73(12):125003, 2006.

[121] Toshiya Kinoshita, Trevor Wenger, and David S Weiss. Observation of a one-dimensional Tonks-Girardeau gas. *Science*, 305(5687):1125–1128, 2004.

[122] Maxime Joos. Phase contrast imaging of mesoscopic Bose-Einstein condensates. Master's thesis, University of Heidelberg, 2013.

[123] Florian Meinert, Manfred J. Mark, Emil Kirilov, Katharina Lauber, Philipp Weinmann, Andrew J. Daley, and Hanns-Christoph Nägerl. Many-body quantum quench in an atomic one-dimensional Ising chain. *arXiv preprint 1304.2628*, 2013.

[124] Ferdinand Brennecke, Rafael Mottl, Kristian Baumann, Renate Landig, Tobias Donner, and Tilman Esslinger. Real-time observation of fluctuations at the driven-dissipative Dicke phase transition. *arXiv preprint 1304.4939*, 2013.

[125] Marco Koschorreck, Daniel Pertot, Enrico Vogt, and Michael Köhl. Universal spin dynamics in two-dimensional Fermi gases. *arXiv preprint 1304.4980*, 2013.

[126] A. M. Kaufman, R. P. Anderson, Thomas M. Hanna, E. Tiesinga, P. S. Julienne, and D. S. Hall. Radio-frequency dressing of multiple Feshbach resonances. *Phys. Rev. A*, 80(5):050701, 2009.

[127] Artur Widera, Fabrice Gerbier, Simon Fölling, Tatjana Gericke, Olaf Mandel, and Immanuel Bloch. Precision measurement of spin-dependent interaction strengths for spin-1 and spin-2 87 Rb atoms. *New Journal of Physics*, 8(8):152, 2006.

[128] E. A. Burt, R. W. Ghrist, C. J. Myatt, M. J. Holland, E. A. Cornell, and C. E. Wieman. Coherence, Correlations, and Collisions: What One Learns about Bose-Einstein Condensates from Their Decay. *Phys. Rev. Lett.*, 79(3):337–340, 1997.

[129] J. Söding, D. Guéry-Odelin, P. Desbiolles, F. Chevy, H. Inamori, and J. Dalibard. Three-body decay of a rubidium Bose–Einstein condensate. *Applied Physics B: Lasers and Optics*, 69(4):257–261, 1999.

[130] Satoshi Tojo, Taro Hayashi, Tatsuyoshi Tanabe, Takuya Hirano, Yuki Kawaguchi, Hiroki Saito, and Masahito Ueda. Spin-dependent inelastic collisions in spin-2 Bose-Einstein condensates. *Phys. Rev. A*, 80(4):042704, 2009.

[131] M. Olshanii. Atomic Scattering in the Presence of an External Confinement and a Gas of Impenetrable Bosons. *Phys. Rev. Lett.*, 81(5):938–941, 1998.

[132] Chiara Menotti and Sandro Stringari. Collective oscillations of a one-dimensional trapped Bose-Einstein gas. *Phys. Rev. A*, 66(4):043610, 2002.

[133] L. Salasnich, A. Parola, and L. Reatto. Effective wave equations for the dynamics of cigar-shaped and disk-shaped Bose condensates. *Phys. Rev. A*, 65(4):043614, 2002.

[134] Luca Salasnich and Boris A. Malomed. Vector solitons in nearly one-dimensional Bose-Einstein condensates. *Phys. Rev. A*, 74(5):053610, 2006.

[135] M. D. Feit, J. A. Fleck Jr., and A. Steiger. Solution of the Schrödinger equation by a spectral method. *Journal of Computational Physics*, 47(3):412–433, 1982.

[136] Juha Javanainen and Janne Ruostekoski. Symbolic calculation in development of algorithms: split-step methods for the Gross–Pitaevskii equation. *Journal of Physics A: Mathematical and General*, 39(12):–179, 2006.

[137] Rolf Rannacher. Einführung in die Numerische Mathematik, 2006. Vorlesungsscriptum.

[138] Rolf Rannacher. Numerische Mathematik 1, 2009. Vorlesungsscriptum.

Danksagung / Acknowledgments

- Zu allererst möchte ich mich bei Markus Oberthaler dafür bedanken, dass er mir die Möglichkeit gegeben hat in seiner Gruppe zu arbeiten. Mit seiner unermüdlichen Begeisterung, der offenen Art und dem fairen Umgang sorgt er für eine phantastische Atmosphäre in der Gruppe. Vielen Dank für das Vertrauen, die Unterstützung, die erhellenden Diskussionen, die vielen Fragen und noch wesentlich mehr Antworten.

- Bedanken möchte ich mich auch bei Thomas Gasenzer für die Bereitschaft meine Arbeit zu begutachten. Die Diskussionen der letzten Jahre haben mir dabei geholfen viele Aspekte unserer Experimente aus anderen Blickwinkeln zu betrachten.

- Panayotis Kevrekidis taught me almost everything I know about numerical methods for the simulation of Bose-Einstein condenstates. Thanks a lot for the patient and thorough explanations, the enlightening discussions and the great hospitality in Amherst.

- A big thank you goes to Matthew Davis and Jacopo Sabbatini, who introduced me to the many fascinating aspects of the Kibble-Zurek mechanism and clarified many of my questions in long discussions by email, on the phone or in person.

- Isabelle Bouchoule has contributed fundamental ideas and calculations to the understanding of the experiments in the final stages of this work. Thank you for the support.

- Ein sehr großer Dank gilt Moritz Höfer der mit mir zusammen viele der vorgestellten Messungen durchführt hat. Danke für die vielen unterhaltsamen und produktiven Tage und Abende im Labor und den unermüdlichen Einsatz bei der Arbeit, aber auch auf dem Rad oder in den Bergen.

- Die Unterstützung von Aisling Johnson war großartig. Vielen Dank für die Erklärungen, das gemeinsame Grübeln und die vielen guten Kommentare und Vorschläge beim Lesen dieser Arbeit.

- Wolfgang Müssel und Helmut Strobel danke ich für die unglaubliche Unterstützung in jeglicher Hinsicht: Für die richtigen Fragen, die klare Sicht auf die Physik, die gründlichen Gedanken und die vielen Stunden in denen ihr diese Arbeit Korrektur gelesen habt.

- Bei Tilman Zibold bedanke ich mich für die vielen gemeinsamen und immer unterhaltsamen Stunden und die immerwährende Diskussionsbereitschaft.

- Christian Gross danke ich für das Einführen in das Experiment, die vielen Erklärungen, die tolle Zusammenarbeit, die vielen Stunden im Labor und die Bloch Kugel.

- Ich möchte mich bei Jirka Tomkovic für die schöne gemeinsame Zeit in Büro und Labor bedanken, für die selbstlose Hilfsbereitschaft und die vielen interessanten Diskussionen.

- Bei Ion Streoscu und Daniel Linnemann bedanke ich mich für die vielen guten Vorschläge und aufmunternden Worte beim Schreiben dieser Arbeit und die gute Zusammenarbeit.

- I would like to thank David Hume for many helpful discussions and the great collaboration.
- Ich hatte das große Glück mit den besten Kollegen zusammenarbeiten zu dürfen, die man sich nur vorstellen kann, dem BEC Team: Jerome, Stefano, Andreas, Jens-Philipp, Naida, Elisabeth, Simon, Jonas, Philipp, Maxime, Mike, ...
- Ebenso tragen alle anderen Matterwavers zur phantastischen Stimmung und Solidarität in der Gruppe bei. Ob beim Diskutieren über Physik, beim Mittagessen, bei Kaffee oder Bier, im Schnee, auf Bergen oder im Keller. Ich hatte immer einen riesigen Spaß mit euch Nalis, Attas und Aegislern!
- Unseren team assistants Dagmar und Christiane gebührt ein großer Dank für die unkomplizierte Hilfe bei der Bewältigung der großen und kleinen bürokratischen Hürden.
- Der Verwaltung des KIP möchte ich danken, dass eben diese Hürden auf Minimalhöhe gestutzt wurden.
- Der mechanischen Werkstatt gilt mein Dank für die präzise Erstellung wesentlicher Komponenten unseres experimentellen Aufbaus.
- Für ihre Geduld und ihr Verständnis möchte ich all denjenigen Freunden danken, mit denen ich in den letzten Monaten viel zu wenig Zeit verbracht habe.
- Ich danke meinen Eltern für die permanente Unterstützung in allen Fragen des Lebens, das Verständnis, die Freude, die langen Spaziergänge und den immer guten Rat.
- Meiner Frau Konstanze danke ich, dass sie immer für mich da ist, mir die Augen öffnet, mit mir lacht, mich versteht, mich mitnimmt und zurückholt. Hannes danke ich für die immer gute Laune, das Lächeln, das Grinsen, das Krächzen, das Lachen und das Schmunzeln. Ebenso gilt mein Dank Emma für das Klopfen, das nasse Gesicht und den warmen Rücken.